POLITECNICO DI TORINO

I Facoltà di Ingegneria

Corso di Laurea Magistrale in Ingegneria Civile

Tesi di Laurea Magistrale

Dam-break wave propagation on a rough surface: Experimental and numerical study

Relatori:
Prof. Davide Poggi
Prof. Gabriel George Katul
Correlatore:
Ing. Silvia Cordero

Candidato:
Mattia Melis

Settembre 2018

“Alla mia famiglia”

Abstract

The effect of hydraulic resistance on the downstream evolution of the water surface profile h in a sloping channel covered by a uniform dense rod canopy following the instantaneous collapse of a dam was examined using flume experiments. Near the head of the advancing wave front, where h meets the rods, the conventional picture of a turbulent boundary layer was contrasted to a distributed drag-force representation. The details of the boundary layer around the rod and any interferences between rods was lumped into a drag coefficient C_d. The study demonstrated the following: In the absence of a canopy, the Ritter solution agreed well with the measurements. When the canopy was represented by an equivalent wall friction as common when employing Manning's formula with constant roughness, it was possible to match the measured wave front speed but not the precise shape of the water surface profile. However, upon adopting a distributed drag force with a constant C_d, the agreement between measured and modeled h was quite satisfactory at all positions and times. The measurements and model calculations suggested that the shape of h near the wave front was quasi-linear with longitudinal distance for a constant C_d. The computed constant C_d($\approx$0.4) was surprisingly much smaller than the C_d($\approx$1) reported in uniform flow experiments with staggered cylinders for the same element Reynolds number. This finding suggested that drag reduction mechanisms associated with unsteadiness, non-uniformity, transient waves, and other flow disturbances were more likely to play a role when compared to conventional sheltering effects.

Abbreviations

SVE: Saint-Venant Equations
LES: Large Eddie Simulations
DNS: Direct Numerical Simulations
EGL: Energy Grade Line

Contents

List of Figures V

List of Tables IX

1 Introduction 1

2 Literature Review 3
2.1 Flow over a smooth concrete channel . . . 3
2.1.1 Experiments . . . 3
2.1.2 Analytical Studies . . . 4
2.2 Flow over a rod dense canopy . . . 7
2.2.1 Experiments . . . 7
2.2.2 Analytical Studies . . . 16

3 Theory 21
3.1 The Frictionless Case and Choice of Normalizing Variables . . . 22
3.2 Canopy Drag and Friction Slope . . . 23
3.2.1 The Isolated Cylinder Case . . . 24
3.2.2 The Array of Cylinder Case . . . 24
3.2.3 The Staggered Canopy Case . . . 24
3.2.4 Blockage and Sheltering Effects on C_d . . . 25
3.3 Wall friction versus distributed drag force: The advancing front region . . . 26

4 Experiments 29
4.1 Flood wave channel . . . 29
4.2 Water Level Measuring Equipment . . . 33
4.3 Run tests . . . 34
4.4 Movies analysis . . . 35
4.5 Camera Calibration . . . 37
4.6 Data Processing . . . 41

5 Numerical Solution of the SVE 49
5.1 Boundary Conditions . . . 49

6 Results 55
6.1 Data summary and comparison with the Ritter Solution . . . 55
6.2 Determination of C_d and n . . . 57
6.3 Comparison between SVE and measurements . . . 59

7 Discussion 73
7.1 Misalignment between the total velocity vector and the cylinder axis 73
7.2 Waviness 74
7.3 Froude Number effects 76
7.4 Separation 79

8 Conclusions 81

A MATLAB Codes 83
A.1 Script to detect the water surface profile 83
A.2 Script to switch from Pixel Coordinates to Metric Coordinates 86
A.3 Script to assemble the water surface profiles 87
A.4 Script to eliminate the outliers 89
A.5 Script to interpolate and average the water level surface profiles 92
A.6 Script to solve the SVE numerically 96
A.7 Script to represent the measured profile and the profile obtained by solving the SVE numerically 103

List of Figures

2.1 *A comparison between measured normalized water surface h_n (red circles) and modeled h_n (black line) using the Ritter Solution for $S_o = 0$ against normalized velocity u_n for all 4 configurations (and $x > 0, t > 0$). Panels from left to right indicate increasing $H_o = 0.15, 0.20, 0.25, 0.30m$. The horizontal dashed line in all panels indicates the water level beneath which it is impossible to detect the surface.* 4

2.2 *Dam Break Wave in a dry horizontal channel.* 6

2.3 *Dimensionless water profile. Comparison between Chanson (2009), Whitham (1955), Dressler (1952) and experimental data (Schoklitsch 1917).* 6

2.4 *Plan and lateral view of the channel flow facility.* 7

2.5 *Drag Coefficient versus the cylinder Reynold's number.* 8

2.6 *Summary of studying about the Drag Coefficient. (N), (F) and (L) indicate Numerical, Field and Laboratory Results. (N/A) indicate information Not Available.* 9

2.7 *Plan view of the Rods Canopy for $\phi = 0.27$.* 10

2.8 *The Coefficients estimated with a linear regression for Tanino and Nepf study compared with Petryk and Koch results.* 10

2.9 *C_d represented in function of ϕ and Re_p.* 11

2.10 *Experimental Setup.* 13

2.11 *Parameters of the Experimental Runs.* 13

2.12 *Comparison between measured and predicted normalized water level. Dots indicate measured values from the experiments, the green lines represents the water level calculated using Cd_{iso}, the red lines are predictions made using Cd_{array} and the black lines represent the new Drag Coefficient proposed Cd_{new}.* 14

2.13 *Drag Coefficients comparison.* 15

2.14 *Variation of the Drag Coefficient C_d with the cylinder Reynold's number for an isolated cylinder. Comparison between the experimental data and the formula proposed by Cheng and labeled as $Equation1$ in the figure.* 16

2.15 *Summary of previously collected experimental data.* 17

2.16 *Variation of Drag Coefficient C_{da} with Reynold's number R_a.* 17

2.17 *Cylinders arrangement.* 18

2.18 *LES and model configuration.* 19

2.19 *Representation of the bulk velocity U_b, constricted velocity U_c and pore velocity U_p. Reference velocity used in the study and correspondent Reynold's Numbers and Drag Coefficients.* 19

2.20 *Drag Coefficients representation in function of the pore velocity U_p and the constricted velocity U_c.* 20

3.1 *A comparison between C_d as a function of $Re_d = UD/\nu$ for an isolated cylinder (i.e. equation 3.16), an array (i.e. equation 3.19) of cylinders [18] with $\phi_v = 0.03$ (the experiment here), and staggered (i.e. equation 3.21) cylinders [24] with $\lambda = (1/2)\sqrt{3}\phi_v$. At $Re_d = 0.7 \times 10^4$, the array and staggered C_d models suggest a switch from 'blockage' to 'sheltering' with increasing Re_d. Also, for $Re_d > \times 10^5$, the C_d models become weakly dependent on Re_d.* 25

4.1 *Overview and later view of the experimental setup showing the channel, the cameras, the dam and the dyed water behind the dam, and a sample image used to determine the water surface profile at one instant in time shortly after the dam break.* 30
4.2 *Detailed later view of the experimental setup, sample image of the rods canopy from above and image the setup ready for a run test.* 31
4.3 *Frontal, rear and lateral vision of the cofferdam.* 32
4.4 *Sony Handycam HDR-XR500.* 33
4.5 *Cameras Setup.* 33
4.6 *Laser functioning.* 34
4.7 *Sample image used to determine the water surface profile for $H_o = 0.3m$, $So = 2\%$, $t = 0.5s$.* 36
4.8 *Sample image used to determine the water surface profile for $H_o = 0.3m$, $So = 2\%$, $t = 1s$.* 36
4.9 *Sample image used to determine the water surface profile for $H_o = 0.3m$, $So = 2\%$, $t = 1.5s$.* 36
4.10 *Image of the checkerboard pattern fixed to one of the three glasses of the channel.* 38
4.11 *Automathic detection of the checkerboard points.* 38
4.12 *Mean Reprojection Error per Image.* 39
4.13 *Extrinsics Parameters Visualization.* 39
4.14 *Presentation of the reprojecting precision.* 41
4.15 *Water surface profile for $S_o = 1\%$, $H_o = 0.20m$, $t = 3.24s$ recorded by Camera 1.* 42
4.16 *Water surface profile for $S_o = 1\%$, $H_o = 0.20m$, $t = 3.24s$ recorded by Camera 2.* 42
4.17 *Water surface profile for $S_o = 1\%$, $H_o = 0.20m$, $t = 3.24s$ recorded by Camera 3.* 43
4.18 *Assembled water surface profile for $S_o = 1\%$, $H_o = 0.20m$, $t = 3.24s$ with the presence of several outliers. The horizontal dashed line indicates the water level above which the water level profile $h(x,t)$ can not be detected.* 44
4.19 *Assembled water surface profile for $S_o = 1\%$, $H_o = 0.20m$, $t = 3.24s$ with the presence of several outliers and interpolating polynomial function.The horizontal dashed line indicates the water level above which the water level profile $h(x,t)$ can not be detected.* 45
4.20 *Assembled water surface profile for $S_o = 1\%$, $H_o = 0.20m$, $t = 3.24s$ once all the outliers are removed.The horizontal dashed line indicates the water level above which the water level profile $h(x,t)$ can not be detected.* 45
4.21 *Representation of the water surface profile, derived from the superimposition of ten run tests, for $S_o = 0\%$, $H_o = 0.15m$, at for different times (t=0.5s, t=1.8s, t=3.1s and t=4.3s).* 46
4.22 *Representation of the water surface profile, derived from the superimposition of ten run tests, for $S_o = 0\%$, $H_o = 0.20m$, at for different times (t=0.5s, t=1.8s, t=3.1s and t=4.3s).* 47

4.23 Representation of the water surface profile, derived from the superimposition of ten run tests, for $S_o = 0\%$, $H_o = 0.25m$, at for different times (t=0.5s, t=1.8s, t=3.1s and t=4.3s). 47
4.24 Representation of the water surface profile, derived from the superimposition of ten run tests, for $S_o = 0\%$, $H_o = 0.30m$, at for different times (t=0.5s, t=1.8s, t=3.1s and t=4.3s). 48

5.1 Evolution of $h(0,t)$ for a 1% slope, $0.25m$ run test. 50
5.2 Inflow hydrograph obtained by differenciating the volumes in time for the first 2 seconds, when the frontwave is visible, and with Ritter's formula for the remaining time. 51
5.3 Logarithmic representation of the measured water level in time, the linear part suggests a power low of h in the recession part. 52
5.4 Inflow hydrograph obtained by differenciating the volumes first, with Ritter's formula when the frontwave is no more recorded by the cameras and with a power low with negative exponent for the remaining time. 53

6.1 A comparison between measured normalized water surface $h_n = h/H_o$ (red circles) and modeled h_n (black line) using the Ritter Solution for $S_o = 0$ against normalized velocity $u_n = (x/t)/\sqrt{gH_o}$ for all 16 configurations (and $x > 0, t > 0$). Panels from left to right indicate increasing S_o = 0,1,2,3% (horizontal arrow) whereas panels from top to bottom indicate increasing $H_o = 0.15, 0.20, 0.25, 0.30$m (vertical arrow).The horizontal dashed line in all panels indicates the water level beneath which it is impossible to detect the surface. . . 56
6.2 A comparison between measured water surface h and modeled h using a constant $n = 0.05$. Using the linear portion of the $h(x,t)$, a near constant $C_d = 0.4$ was determined and used throughout. The horizontal dashed line in all panels indicates the water level beneath which it is impossible to detect the surface. . . 58
6.3 A comparison between measured and modeled $h(x,t)$ for $S_o = 0\%$ and $H_o = 0.15m$. The first panel in the first row from the left represents the measured $h(x,t)$, the second is modeled $h(x,t)$ with $n =$ 0,05. In the second row from the left is shown the modeled $h(x,t)$ with $C_{d,s}$ and modeled $h(x,t)$ with $C_d = 0.4$. 60
6.4 A comparison between measured and modeled $h(x,t)$ for $S_o = 0\%$ and $H_o = 0.15m$. $h(x,t)$ measured is represented with the three $h(x,t)$ modeled ($C_{d,s}$, $C_d = 0.4$ and $n = 0.05$) for three significant times ($t = 0.5s$, $t = 1.5s$ and $t = 2.5s$). The three time instants are shown in figure 6.3 as a horizontal dashed red line. 61
6.5 A comparison between measured and modeled $h(x,t)$ for $S_o = 1\%$ and $H_o = 0.20m$. The first panel in the first row from the left represents the measured $h(x,t)$, the second is modeled $h(x,t)$ with $n =$ 0,05. In the second row from the left is shown the modeled $h(x,t)$ with $C_{d,s}$ and modeled $h(x,t)$ with $C_d = 0.4$. 62
6.6 A comparison between measured and modeled $h(x,t)$ for $S_o = 1\%$ and $H_o = 0.20m$. $h(x,t)$ measured is represented with the three $h(x,t)$ modeled ($C_{d,s}$, $C_d = 0.4$ and $n = 0.05$) for three significant times ($t = 0.5s$, $t = 1.5s$ and $t = 2.5s$). The three time instants are shown in figure 6.9 as a horizontal dashed red line. 63

6.7 A comparison between measured and modeled $h(x,t)$ for $S_o = 2\%$ and $H_o = 0.25m$. The first panel in the first row from the left represents the measured $h(x,t)$, the second is modeled $h(x,t)$ with $n = 0{,}05$. In the second row from the left is shown the modeled $h(x,t)$ with $C_{d,s}$ and modeled $h(x,t)$ with $C_d = 0.4$. 64
6.8 A comparison between measured and modeled $h(x,t)$ for $S_o = 2\%$ and $H_o = 0.25m$. $h(x,t)$ measured is represented with the three $h(x,t)$ modeled ($C_{d,s}$, $C_d = 0.4$ and $n = 0.05$) for three significant times ($t = 0.5s$, $t = 1.5s$ and $t = 2.5s$). The three time instants are shown in figure 6.7 as a horizontal dashed red line. 65
6.9 A comparison between measured and modeled $h(x,t)$ for $S_o = 3\%$ and $H_o = 0.30m$. The first panel in the first row from the left represents the measured $h(x,t)$, the second is modeled $h(x,t)$ with $n = 0{,}05$. In the second row from the left is shown the modeled $h(x,t)$ with $C_{d,s}$ and modeled $h(x,t)$ with $C_d = 0.4$. 66
6.10 A comparison between measured and modeled $h(x,t)$ for $S_o = 3\%$ and $H_o = 0.30m$. $h(x,t)$ measured is represented with the three $h(x,t)$ modeled ($C_{d,s}$, $C_d = 0.4$ and $n = 0.05$) for three significant times ($t = 0.5s$, $t = 1.5s$ and $t = 2.5s$). The three time instants are shown in figure 6.9 as a horizontal dashed red line. 67
6.11 A comparison between measured and modeled $h(x,t)$ using a Manning's formula with constant $n = 0.05$ for all (x,t) and all 16 runs. The colormap signifies density of points. The one-to-one line is also shown. 68
6.12 A comparison between measured and modeled $h(x,t)$ using the staggered $C_{d,s}$ formulation for all (x,t) and all 16 runs. The colormap signifies density of points. The one-to-one line is also shown. 69
6.13 A comparison between measured and modeled $h(x,t)$ using a constant $C_d = 0.4$ for all (x,t) and all 16 runs. The colormap signifies density of points. The one-to-one line is also shown. 70

7.1 Calibrated values of the Drag Coefficient C_d as function of Reynolds number. . 74
7.2 A comparison between measured and modeled $h(x,t)$ using a Etminan's formula with reduced asymptotic limit for all (x,t) and all 16 runs. The colormap signifies density of points. The one-to-one line is also shown. 75
7.3 Calibrated values of the Drag Coefficient C_d as function of Froude number. . . 77
7.4 A comparison between measured and modeled $h(x,t)$ using C_d as a function of Fr all (x,t) and all 16 runs. The colormap signifies density of points. The one-to-one line is also shown. 78

List of Tables

4.1 *Points of the checkerboard in metric coordinates known as "World Points".* . . 40
4.2 *Reprojected points of the checkerboard in metric coordinates known as "New World Points"* 40

6.1 *Characteristics of the linear regression for* $C_{d,s}$, $C_d = 0.4$ *and* $n = 0.05$. 71

7.1 Characteristics of the linear regression for $C_{d,s}$, $C_d = 0.4$, $n = 0.05$, $C_{d,s} modified$ and $C_d Froude$ 80

1. Introduction

Over the centuries agriculture has been one of the most important form of sustenance for all the populations across the entire world. The first pioneers soon realized that the systematic request of water from the plants could not be supplied by the random nature of the rains. In order to have water supplies all year, independently that it was a rainy period or not, the first artificial reservois were built. Historically, the first certified dam was built around the 4000 B.C. in Egypt. It was followed by more dams built by the Babylonians. These dams, constructed with compacted soil, had the main purpose of storing water to power the irrigation systems.
Nowadays there are hundreds of thousands dams all over the world and, to the initial goal of storing water, it's been added up the purpose of generate electricity with the birth of the so called "*Hydroelectric*". The dams are also the main supplier of water for domestic as well as industrial use.
The dams, which are barriers built across the rivers, have different sizes. The smallest ones, known as *"small dams"* count less than 15 meters of height or a million cube meters of water stored. All the others are labeled as *"big dams"*. For example one of the most famous dams in Africa is the *Aswan Dam*, built across the Nile River. It is 3,830 m long, 980 m wide at the base, 40 m wide at the crest and 111 m tall. It holds 169 millions cubic meters of water and has an installed power of 2100 MW. Another historically remarkable dam is the *"Hoover Dam"*, with its 19 turbines and an installed capacity of 2080 MW provides power in Arizona, California and Nevada. The reservoir has a capacity of 35.2 millions cubic meters of water.
Although the good sides, the building of a dam comes with dangerous consequences too. In fact, the collapse or even a partial break of the dam would generate the spillage of a great amount of water with devastating consequences for the downstream localities. The collapse of the dam, hereafter referred to as dam-break, even if it is not a common event has attached great importance because it results in life losses as well as environmental and urban damages. Despite the fact that the "*big dams*" have larger amounts of water, the failure of *"small dams"* is way more recurrent resulting in more human losses and higher costs for renovations. In particular the collapse of the *"small dams"* is even more frequent for the privately-owned dams [60]. According to a study conducted in China in 2009 in the last two centuries more than 900 hundreds dams collapsed. About the 66% of the 593 cases collected are represented by earth dams [79]. It is shown that the *"small dams"* appear to have a higher probability to collapse, in fact the 50% of the failures concern the dams with an height less than 15m. Moreover the 47% of failures is about the first 20 years after the construction. For example the "*Coedty dam*" in the United Kingdom with a 0.32 millions cube meters reservoir failed on 1925 causing the death of 16 people [55]. The Kelly Barnes, with his 11.6m height, failed on 1977 causing the death of 39 people [9], [60].
Moreover, interest in the dam-break problem in hydrology and hydraulics have exponentially proliferated given their similarities to surging or flash/outburst floods in streams [64], glacial lake bursts [13], tsunami run up on coastal plains [14], intense rainfall induced overland flow over vegetated surfaces in dryland ecosystems [41, 71, 6, 59], peatlands [28] and tropical regions [1], inflow into weltands and marshes [38, 51], among others. More broadly, the shallow

water equations describing water flow after dam-break encompass diverse phenomenon such as thin-film flows, gravity currents, and the non-linear Fokker-Planck equation widely used in engineering, physics, chemistry, and biology [20].
In order to reduce the risk linked to the dam-break is crucial to comprehend the features of the flow outcoming from the dam. The dam-break problem is associated to a sudden release of water behind a vertical wall [76]. The salient features of such shallow flows are unsteadiness and inertia being balanced by hydrostatic pressure gradients and resistive forces.
Hence, the work here has the main goal to add to the experimental literature benchmark flume experiments where the static water level behind the dam as well as bed slope are varied for a channel uniformly covered by a dense rod canopy. It is envisaged that these experiments can be used in testing future simulations (LES or DNS) as well as theories and models aimed at describing dam-break wave propagation in situations where the resistance to the flow is not originating from side or bed friction. The majority of applications listed in the introduction fall in this aforementioned category.

2. Literature Review

For many years the dam-break problem has been a central theme in hydrology and hydraulics research. This interest led to the accomplishment of a great number of run tests and analytical studies useful to describe the behavior of the wave following the sudden release of water behind the dam. In this section will be reported the main results achieved for horizontal prismatic channels as well as sloping. Furthermore will be examined all the prior literature comprehending both the cases where the bed-ground is smooth as well as highly vegetated.

2.1 Flow over a smooth concrete channel

2.1.1 Experiments

The huge loss of human lives and money due to the dams collapsing over the last century has resulted in many experimental studies of the dam-break problem.
Most of the experiments were reviewed by Lindsey Ann LaRoque [49]. The experiments above mentioned were conducted between 1960 and 2014 and involved smooth concrete sloping channels. The characteristics of the flow were captured by measuring the free water level profile as well as the velocity of the flow by image analysis techniques. On the other hand it is difficult to find direct measurement of the flow velocity. Among them, for example, Stansbly in 1998 [68] exclusively focused on the initial stages of the instantaneous dam-break over smooth surfaces and Janosi in 2004 [36] studied the frictional reductions via additions of polymers.
At last is worth mentioning the experimental studies conducted by Schoklitsch in 1917 [66] which will be compared with the analytical solutions proposed in the next section.

Fasanella (2017)

In 2017 Giovanni Fasanella analyzed all the major experimental literature [25], with particular attention to non-prismatic and not straight channels, they will not be repeated here.
In his work he conducted experiments on dam-break over a smooth concrete bed-ground channel using the same facility which will be used in this thesis proving the validity of the Ritter Solution.
The test runs were performed using a flat channel and involved four differing water levels behind the dam ($H_o = 0.15$m, 0.20m, 0.25m, 0.30m) resulting in a total of 4 configurations. The displaying of the adimensional results demonstrates the collapsing of the data on the Ritter Solution as shown in figure 2.1.

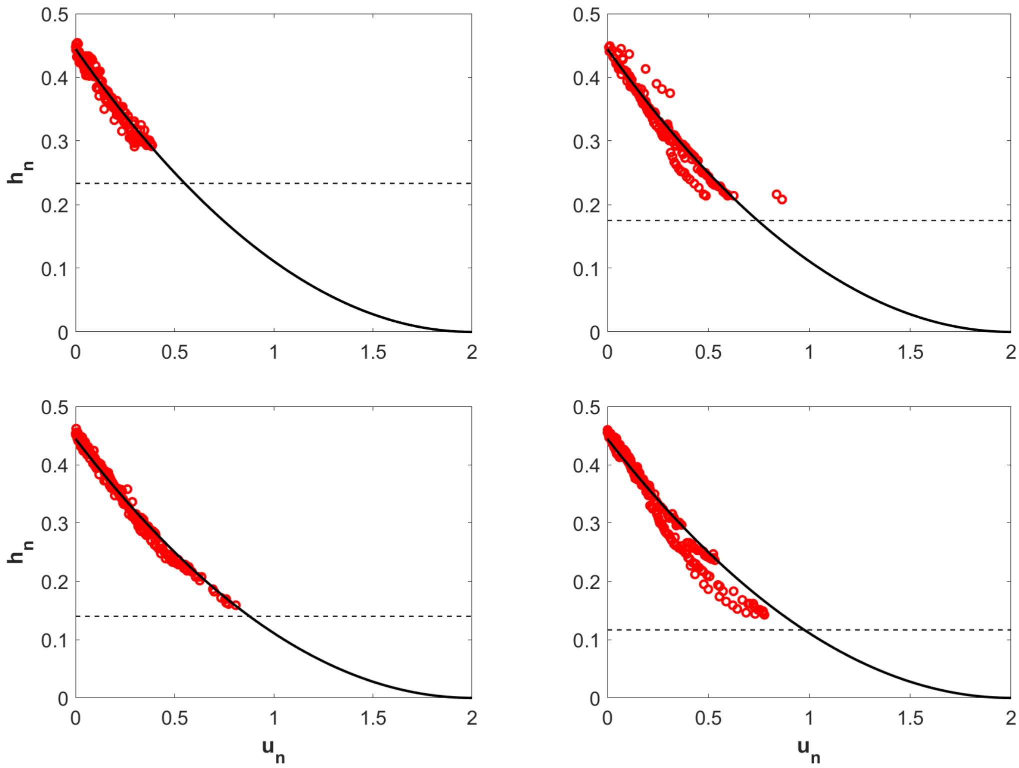

Figure 2.1. *A comparison between measured normalized water surface h_n (red circles) and modeled h_n (black line) using the Ritter Solution for $S_o = 0$ against normalized velocity u_n for all 4 configurations (and $x > 0, t > 0$). Panels from left to right indicate increasing $H_o = 0.15, 0.20, 0.25, 0.30m$. The horizontal dashed line in all panels indicates the water level beneath which it is impossible to detect the surface.*

2.1.2 Analytical Studies

Well known analytical studies of the dam-break problem include frictionless flows over a flat rigid surface [65] and simplified frictional corrections to such flows [23, 76, 30, 32, 31] discussed elsewhere [27]. Moreover, extensions to steep slopes [5] as well as gradual dam breaching [52, 11, 72, 14, 73] instead of instantaneous dam breaks have also been proposed.
In 2009 Chanson [14] developed an analytical solution for the dam-break wave using the method of characteristics. The results obtained by Chanson, for horizontal and sloping channels, are compared with the most important previous studies by Ritter [65], Dressler [23] ,Whitham [76] and Hunt [30, 32, 31].
For the 1D Dam-Break problem the wave produced by the instantaneous collapse of the dam is represented by the SVE:

$$\frac{\partial d}{\partial t} + d\frac{\partial V}{\partial x} + V\frac{\partial d}{\partial x} = 0, \tag{2.1}$$

$$\frac{\partial V}{\partial t} + V\frac{\partial V}{\partial x} + \frac{\partial d}{\partial x} + S_f - S_o = 0, \tag{2.2}$$

where d is the dimensionless water level, V is the dimensionless velocity, S_f is the Friction Slope, S_o is the channel slope, t is the dimensionless time and x is the dimensionless distance from the dam. The Friction Slope S_f is represented in function of the Darcy-Weisbach factor f:

$$S_f = \frac{f}{2V'^2 g D'_H}, \tag{2.3}$$

where D'_H is the dimensional hydraulic radius and V' is the dimensional velocity. Chanson proposed to solve the SVE with the method of characteristic which set the following system of equations:

$$\frac{\partial}{\partial t}(V + 2C) = S_o - S_f, \tag{2.4}$$

$$\frac{\partial}{\partial t}(V - 2C) = S_o - S_f, \tag{2.5}$$

where the celerity C is equal to 1.
If a frictionless case is considered, $S_f = 0$, for a horizontal channel equations 2.4 and 2.5 give Ritter's solution ($C = 1$):

$$\frac{x}{t} = 2 - 3\sqrt{d}, \tag{2.6}$$

$$V = \frac{2}{3}(1 + \frac{x}{t}), \tag{2.7}$$

In 1995 Whitham introduced the concept that, in case of Dam-Break, the fluid can still be considered as ideal ($S_f = 0$) except for the wave-tip zone dominated by resistance. Experiments by Dressler [23] showed that in the wave-tip zone the velocity could approximately be considered constant. Follows that equation 2.2 yields to:

$$\frac{\partial d}{\partial t} + \frac{f}{8}\frac{U^2}{2d} = 0, \tag{2.8}$$

The integration of the previous equation gives the shape of the wave-tip:

$$d = \sqrt{\frac{f}{4}U^2(x_s - x)}, \tag{2.9}$$

For turbulent motion the flow resistance f can be approximated with Altsul formula:

$$f = 0.1(1.46\frac{k'_s}{D'_H} + \frac{100}{Re})^{1/4}, \tag{2.10}$$

where k'_s is the equivalent sand roughness height. Therefore the equation describing the free water surface was presented by Chanson as follows:

$$d = \frac{1}{9}(2 - \frac{x}{t})^2 \quad -t \leq x \leq (\frac{3}{2}U - 1)t \tag{2.11}$$

and

$$d = (\frac{9}{32}(3.65x10^{-5}k_s + \frac{2.5x10^{-3}}{Re_d U})^{1/4}U^2(x_s - x))^{4/9} \quad (\frac{3}{2}U - 1)t \leq x \leq x_s. \tag{2.12}$$

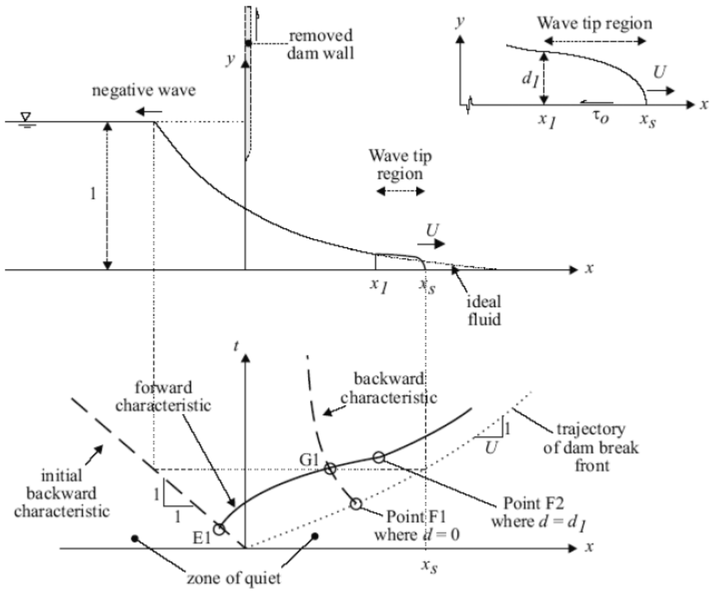

Figure 2.2. *Dam Break Wave in a dry horizontal channel.*

The analytical solutions (Ritter, Whithman, Dressler) as well as experimental data obtained in large facilities by Schocklitsch are compared in figure 2.3 with the equation proposed by Chanson.

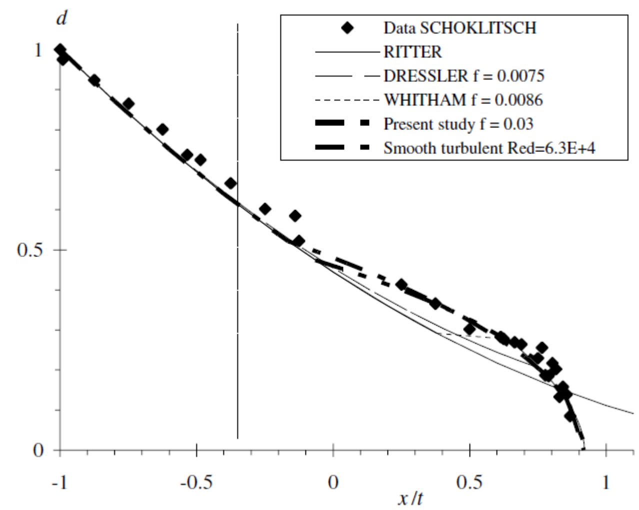

Figure 2.3. *Dimensionless water profile. Comparison between Chanson (2009), Whitham (1955), Dressler (1952) and experimental data (Schoklitsch 1917).*

The main result achieved by Chanson (see figure 2.3) was to obtain a formula able to reproduce the features of the 1D dam-break problem. It was further demonstrated the validity of the Ritter solution with the exception of the shape of the wave-front tip. Furthermore Chanson extended the Ritter Solution in the case of a dam-break for a frictionless sloping channel.

2.2 Flow over a rod dense canopy

2.2.1 Experiments

Despite vast life and economic losses commonly associated with dam-breaks, controlled laboratory experiments on this topic remain surprisingly limited with the exception of the cases where a vegetation pattern is not considered [49]. All the experiments found in literature focused on non-uniform flow over vegetion such as Kobayashi in 1993 [44], Poggi in 2004 [61], Tanino and Nepf in 2008 [70] and Wang in 2015 [74]. These experiments, described afterwards, were performed by setting a steady-state condition for the flow, hence without taking into account the main features of the dam-break such as unsteadiness and inertia.
Some laboratory studies are now considering single isolated obstacles [67] as may be encountered in an urban environment at high Froude numbers but not an array of obstacles.
Hence, the work here has the main goal to fill the knowledge gap by adding to the experimental literature benchmark flume experiments where the static water level behind the dam as well as bed slope are varied for a channel uniformly covered by a dense rod canopy.

Poggi et al. (2004)

In 2004 Poggi [61] conducted flume experiments to seek a phenomenological theory able to describe the key flow statistics in terms of canopy density.
The experiments were carried out at the Hydraulics Laboratory, sited in Politecnico di Torino. The re-circulating prismatic channel was 18 m long, 0.90 m wide and 1 m deep. The walls were made of glass in order to permit the passage of the laser Doppler Anemometer (LDA) light. The facility is shown in figure 2.4.

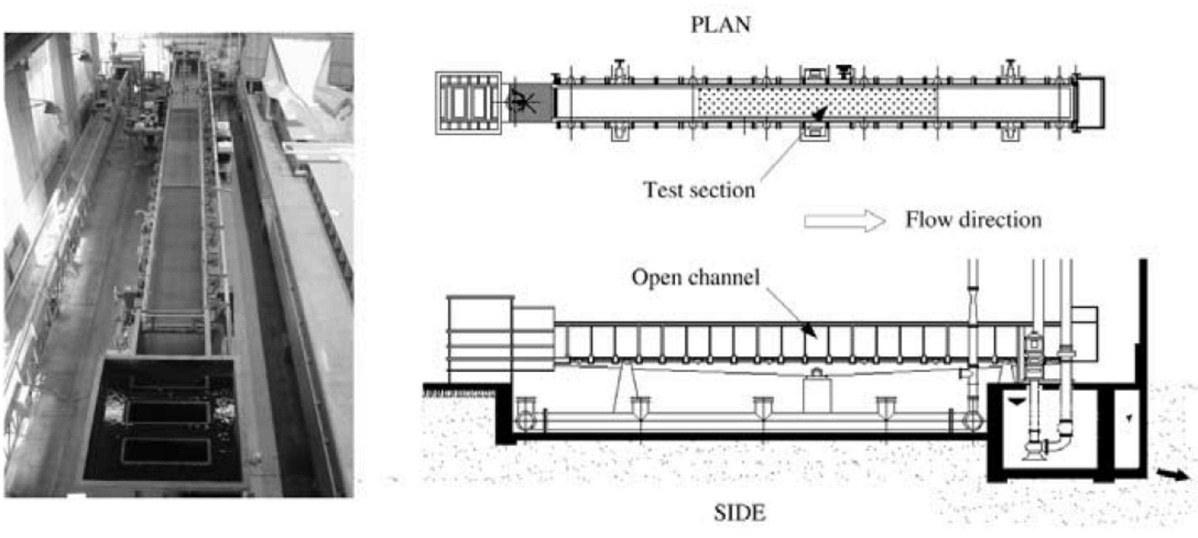

Figure 2.4. *Plan and lateral view of the channel flow facility.*

The vegetation was represented by an array of vertical stainless steel cylinders, 0.12m high and with a diameter of 0.004m. Five canopy roughness densities were analyzed: 67, 134, 268, 536, and 1072 rods per square meter. The velocity was measured by using two-component laser Doppler Anemometry (LDA). The experiments were conducted in a steady-state condition, in fact the flow Reynold's number was preserved by mainteining a constant water level equal to 0.6m. Moreover a fluorescent dye solution (Red Rhodamine) was mixed to the water. The Rhodamine is a red dye that becomes metallic green when excited by the laser. A cylindrical

lens allowed to split the laser beam into a thin sheet and provided a planar illumination at the section considered.
The Drag Coefficient, function of the Reynold's number and influenced by the Sheltering Effect was calculated by the following formula:

$$C_d(z, R_e, a) = -2(\frac{\partial(\overline{u'w'})}{\partial z} + \frac{\partial \overline{p}}{\partial x})(a\overline{u}^2)^{-1}. \tag{2.13}$$

The $\overline{u'w'}$ profiles were measured as well as $\overline{u}$.
In figure 2.5 are plotted with a dashed line the C_d expected for a single cylinder ($C_d = Re^{0.5}$, Bachelor 1954) and the C_d obtained with equation 2.13.

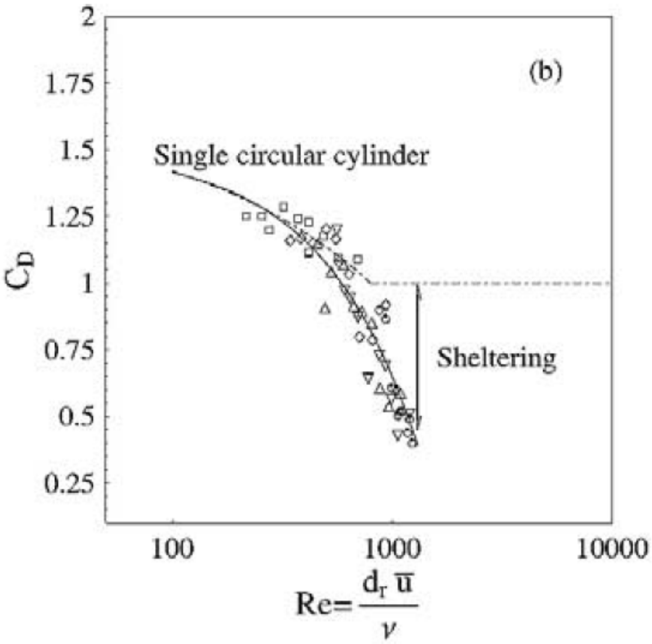

Figure 2.5. *Drag Coefficient versus the cylinder Reynold's number.*

The tendency showed was a decreasing of C_d with the Reynold's number in contrast with a constant value (for lower Reynold's numbers) showed by the isolated case cylinder. This decrease was attributed to the sheltering effect which employed a Reynold's number dependency even for $Re > 1000$. Hence it was proposed a new formulation for C_d:

$$C_d(R_{ed}) = 1.5 - 8.5R_{ed}10^{-4} \tag{2.14}$$

Tanino and Nepf (2008)

In 2008 Tanino and Nepf investigated the drag generated by a random dense and rigid canopy represented by rods, when crossed by a flow in a steady-state condition. The main goal was to study the relation between the Drag Coefficient C_d and the cylinder Reynold's number $Re_p = Ud/\nu$ when several canopy densities ϕ were considered.
Starting from the numerical and experimental studies already produced in literature (see figure 2.6) were investigated the cases yet unexplored, for a two dimensional array of cylinders, where $\phi > 0.05$ for $Re_p > 100$ and $\phi < 0.05$ for $Re_p < 1000$.

Source	Array	Configuration	ϕ	Reynolds number
Ayaz and Pedley 1999	Rigid cylinders (N)	Square	0.13	$\leqslant 40.00/(1-\phi)$
			0.35	
			0.50	
			0.59	
Koch and Ladd 1997	Rigid cylinders (N)	Random	0.05	$\leqslant 37$
			0.10	$\leqslant 33$
			0.20	$\leqslant 100$
			0.40	$\leqslant 67$
		Square, staggered	0.2	57–210
			0.4	82–320
Lee et al. 2004	Sawgrass (L; F)	N/A	N/A	0–200 (L)
				$70-10^4$ based on depth (F)
Mazda et al. 1997	Two tidal mangrove swamps (F)	N/A	0.05–0.45 (depth dependent)	N/A
Nepf 1999	Rigid cylinders (L)	Random	0.006	4,000–10,000
			0.02	
			0.06	
Petryk 1969	Rigid cylinders (L)	Random	0.015	$(0.6-5)\times 10^4$
			0.027	$(3-9)\times 10^4$
Stone and Shen 2002	Rigid cylinders (L)	Staggered	0.0055	$O(250-8{,}000)$ assuming $\nu=0.009$ cm^2/s
			0.0220	
			0.0610	
Wu et al. 1999	Flexible horsehair mattress (L)	N/A	N/A	20–3,000 based on depth and $U_p(1-\phi)$

Figure 2.6. *Summary of studying about the Drag Coefficient. (N), (F) and (L) indicate Numerical, Field and Laboratory Results. (N/A) indicate information Not Available.*

The Drag Coefficient C_d was calculated operating in steady-state conditions by modelling the coefficients α_0 and α_1:

$$C_d = 2(\frac{\alpha_0}{Re_p} + \alpha_1). \tag{2.15}$$

The Results were compared to the empirical expression proposed by White (1991) [48]:

$$C_d \approx 1 + 10Re_p^{-2/3}. \tag{2.16}$$

The Experiments were performed in two Plexiglass recirculating flumes. The flow rate Q was measured with an in-line flow meter. The run test were executed taking into account several vegetation densities such as $\phi = 0.091$, $\phi = 0.1$, $\phi = 0.20$, $\phi = 0.27$, and $\phi = 0.35$ and Re_p from 25 to 685.

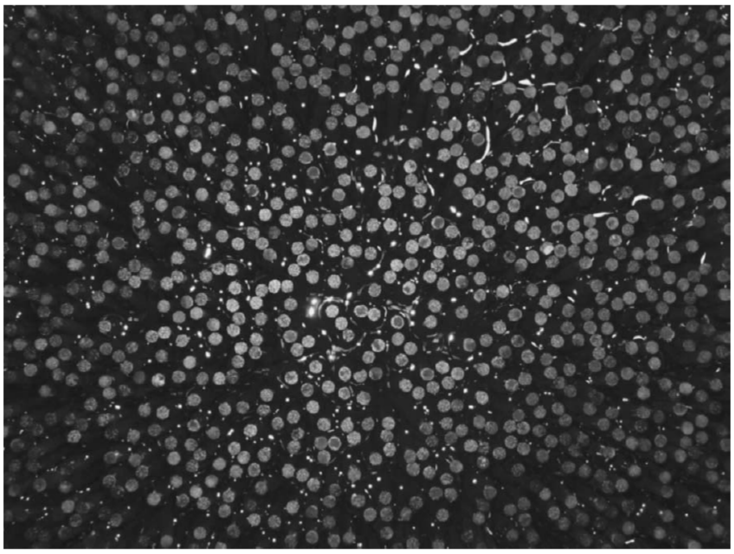

Figure 2.7. *Plan view of the Rods Canopy for $\phi = 0.27$.*

The Drag Coefficient estimated parameters α_0 ans α_1 are shown in figure 2.8 as well as the correlation coefficient r and the number of data points included in the regression n.

Source	ϕ	α_0	α_1	r	n	Re_p range
Petryk 1969	0.015	$(3.0\pm1.2)\times10^3$	0.49 ± 0.04	0.975	10	$(0.6-5)\times10^4$
	0.027	$(3.2\pm2.4)\times10^3$	0.66 ± 0.04	0.993	5	$(3-9)\times10^4$
Present study	0.091	25 ± 12	0.74 ± 0.03	0.985	18	148–685
	0.15	84 ± 14	1.12 ± 0.06	0.969	26	87–396
	0.20	85 ± 5	1.15 ± 0.02	0.996	37	29–482
	0.27	82 ± 2	1.58 ± 0.01	0.999	20	25–294
	0.35	84 ± 6	1.72 ± 0.03	0.997	19	40–305
Koch and Ladd 1997	0.05	11	0.97			5–37
	0.1	17	1.0			6–33
	0.2	40	1.2			6–100
	0.4	167	2.6			8–67

Figure 2.8. *The Coefficients estimated with a linear regression for Tanino and Nepf study compared with Petryk and Koch results.*

The most important result achieved in this paper is shown in in figure 2.9. C_d decreases as Re_p increases for all ϕ investigated. The data also demonstrate that drag exerted by an array of cylinders is bigger than an isolated cylinder.

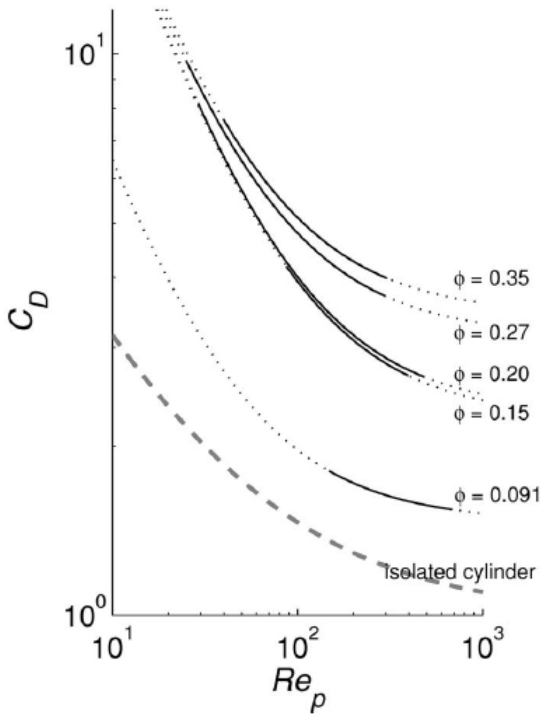

Figure 2.9. *C_d represented in function of ϕ and Re_p.*

Wang et al. (2015)

Wang in 2015 studied the flow redistribution on flat ground from crusted bare soil to vegetated patches following intense rainfall events. In order to mimic this phenomenon several flume experiments were carried out using plastic rods to represent the vegetation. The measured $H(x)$ obtained by image processing were used for testing different models to represent the roughness. If a rectangular channel with a constant width B, water depth H(x), cross-sectional area A(x) is considered, the flow $Q(x)$ among the rod canopy can be described using the SVE obtained rearranging the friction slope definition:

$$S_f = -\frac{\partial E}{\partial x} = -\frac{\partial}{\partial x}(z_g + \frac{P}{\gamma} + \alpha\frac{U^2}{2g}), \tag{2.17}$$

$$U\frac{\partial U}{\partial x} + g\frac{\partial H}{\partial x} - g(S_o - S_f) = 0. \tag{2.18}$$

The momentum equation, associated to the continuity equation, provides the relation between U and $H(x)$, unknowns of the problem. In order to know the characteristics of the flow (U and $H(x)$) a closure is required for S_f. Wang, starting from the past literature, used several closing in order to reproduce the experimental water depth. For S_f, according to the past literature, were proposed two closures:

$$S_f = \left(\frac{2gn^2}{R_h^{4/3}}\right)\frac{U^2}{2g}, \tag{2.19}$$

and

$$S_f = \left(\frac{C_d m D \alpha_s}{1 - \alpha_s \phi_v}\right)\frac{U^2}{2g}. \tag{2.20}$$

The first one is carried out by considering a local uniform flow, starting from Manning's formula. The second one is obtained by considering a force balance between the flow driving mechanism and resistance along the stream direction. In the second case the Friction Slope S_f is a function of the Drag Coefficient C_d. An expression for $C_{d,iso}$ describing the data for isolated cylinders for $Re_d < 10^5$ was given by Cheng in 2012 [16]

$$C_{d,iso} = 11(Re_d)^{-0.75} + 0.9\Gamma_1(Re_d) + 1.2\Gamma_2(Re_d), \tag{2.21}$$

where

$$\Gamma_1(Re_d) = 1 - \exp\left(-\frac{1000}{Re_d}\right), \tag{2.22}$$

and

$$\Gamma_2(Re_d) = 1 - \exp\left[-\left(\frac{Re_d}{4500}\right)^{0.7}\right]. \tag{2.23}$$

In the case of an array of cylinders a formulation for $C_{d,a}$ derived from a large synthesis of experiments on emergent vegetation and was given by Cheng in 2010 [18]:

$$C_{d,a} = \frac{50}{Re_v} + 0.7\left[1 - \exp\left(-\frac{Re_v}{15000}\right)\right]. \tag{2.24}$$

The linkage between the vegetation-array and a stem related Reynolds number is

$$Re_v = \frac{\pi(1-\phi_v)}{4\phi_v} Re_d. \tag{2.25}$$

Moreover a new $C_{d,new}$ was inferred with the flume data:

$$C_{d,new} = \frac{2g(1-\phi_{veg})}{mD}(P^* - A^*) \tag{2.26}$$

where P* and A* are respectively the pressure and the advection component.
The experiments were conducted in China using a flume 15m long and 0.3m wide. The channel sides were made of glass to permit optical access in order to image the water surface. The vegetation was represented by an array of plastic cylinders, the diameter was $D = 0.008m$ and the height $h = 0.25m$. The cylinders were accommodated on a plastic board with uniformly spaced holes which permitted to change the position hence the density of the vegetation as shown in the next figure.

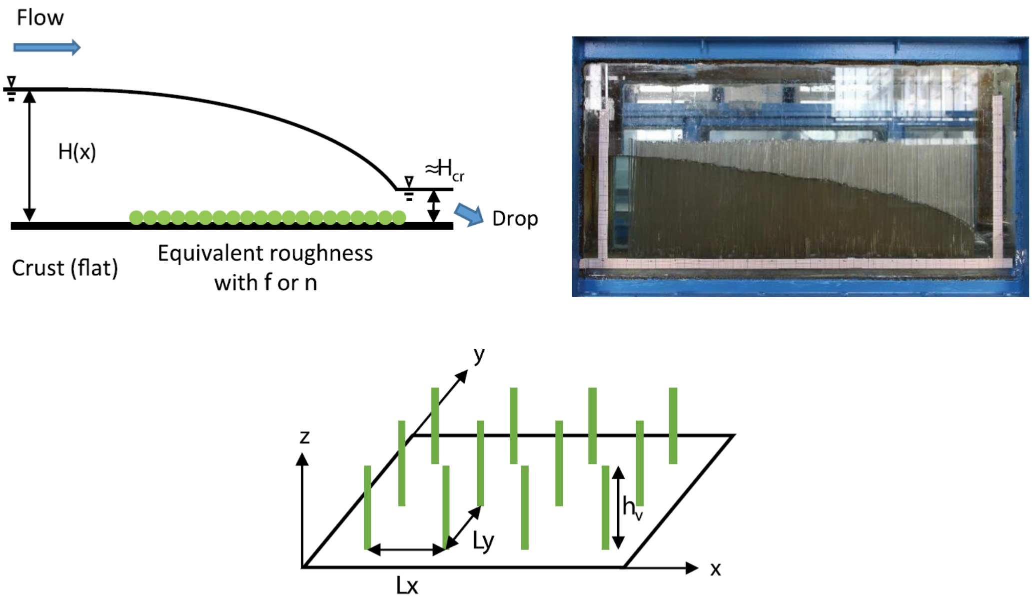

Figure 2.10. *Experimental Setup.*

Eight vegetation densities were investigated, labeled Runs A to H throughout and summarized in the next table. The most important characteristic of this experiments is that a steady flow was set $Q = 0.003m^3/s$.

Run	ϕ_{veg}	ϕ_{board}	ϕ_{hole}	L (m)	H_0 (m)
A	0.419	0.419	0	0.7125	0.2145
B	0.291	0.291	0	0.6353	0.1379
C	0.206	0.206	0	0.6482	0.1107
D	0.163	0.163	0	0.6581	0.0984
E	0.073	0.291	0.218	0.6162	0.0715
F	0.041	0.163	0.122	0.6560	0.0628
G	0.018	0.291	0.273	0.5251	0.0536
H	0.010	0.163	0.153	0.5275	0.0466

Figure 2.11. *Parameters of the Experimental Runs.*

In figure 2.12 is shown the experimental water profile and the profile provided by SVE Equations associated to the S_f closures mentioned before. This comparison demonstrated that the use of SVE with Cd_{iso} overestimated the water level while the use of Cd_{array} underestimated it.

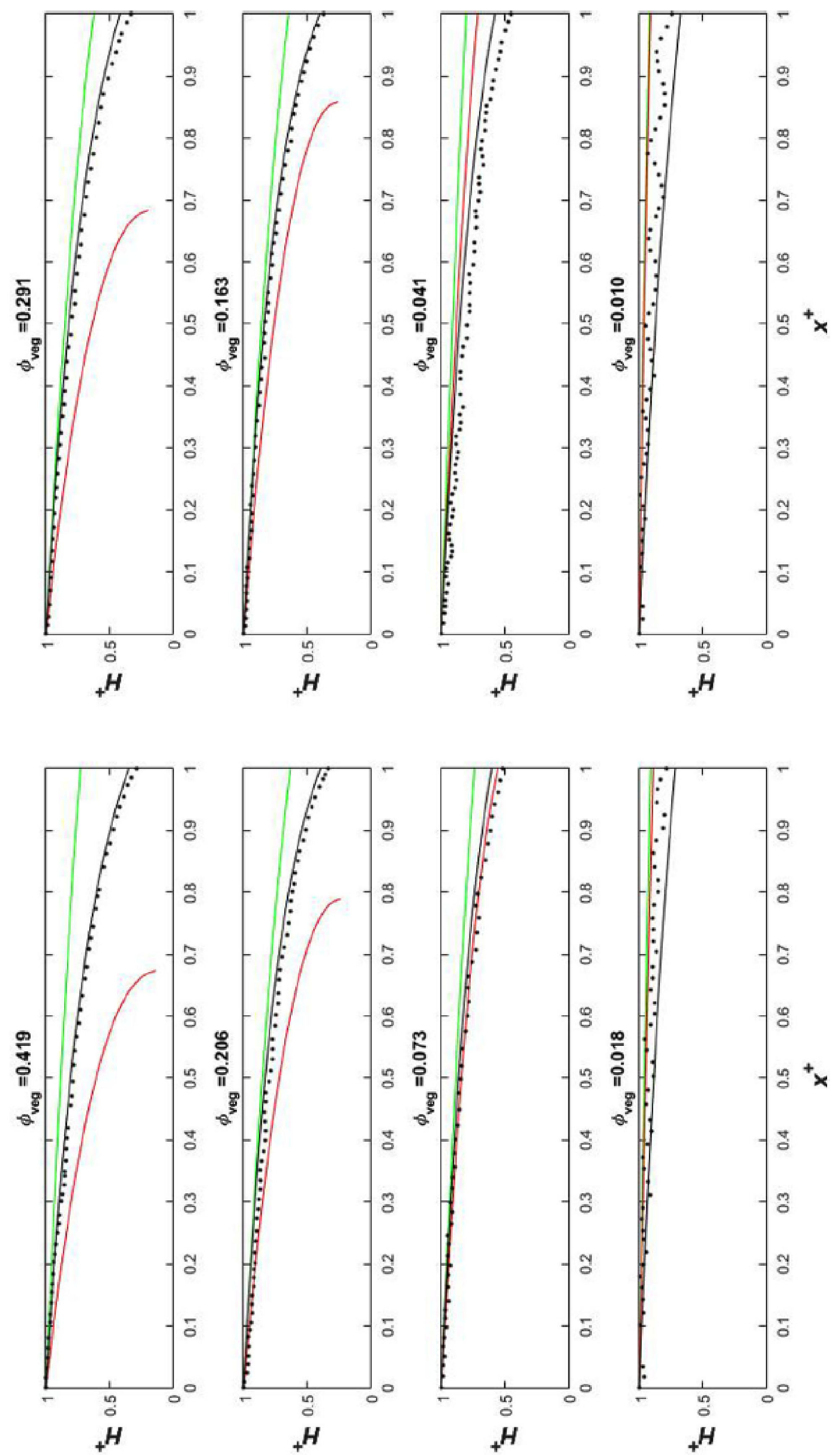

Figure 2.12. *Comparison between measured and predicted normalized water level. Dots indicate measured values from the experiments, the green lines represents the water level calculated using Cd_{iso}, the red lines are predictions made using Cd_{array} and the black lines represent the new Drag Coefficient proposed Cd_{new}.*

In figure 2.13 is shown the comparison between the Drag Coefficients formulations.

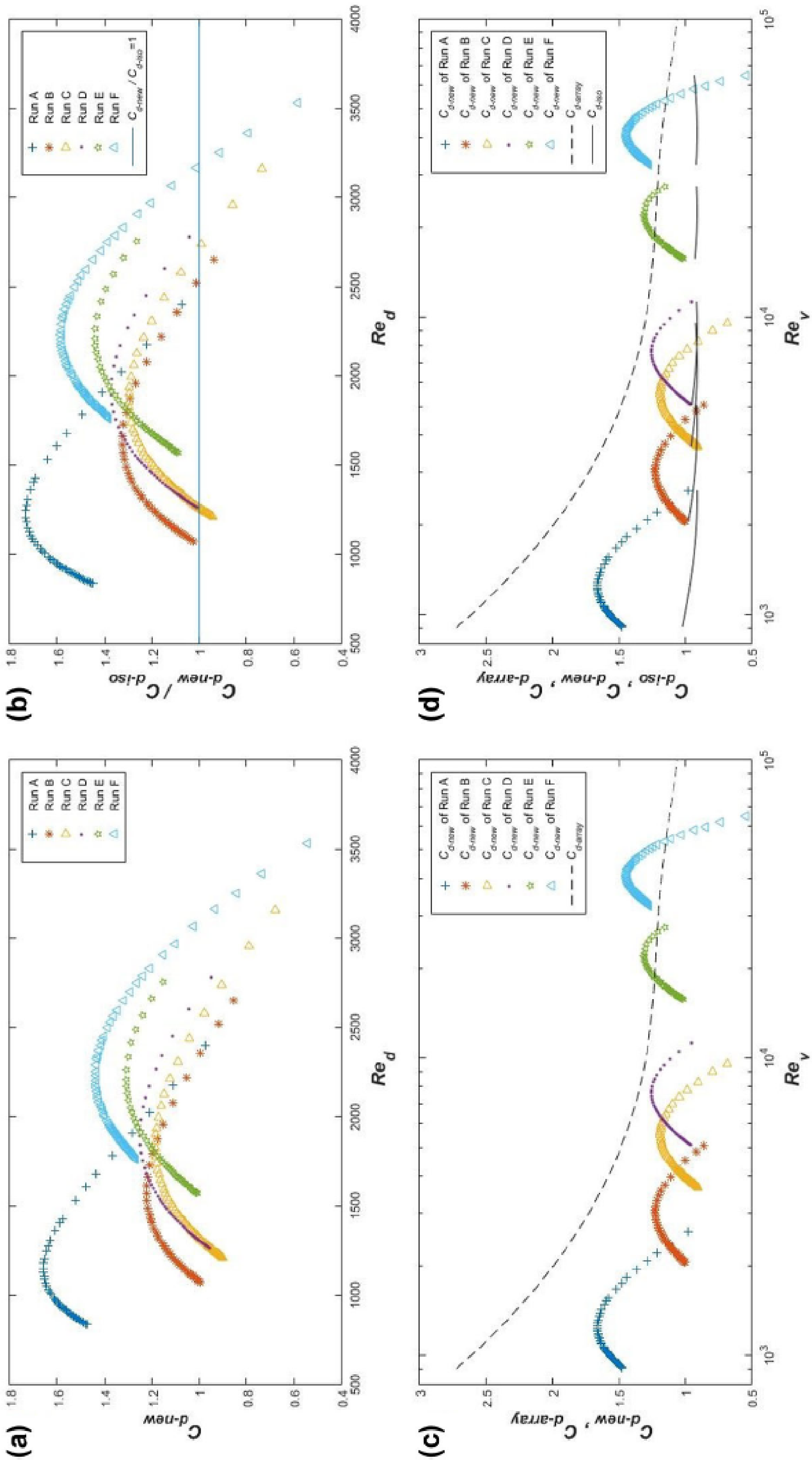

Figure 2.13. *Drag Coefficients comparison.*

2.2.2 Analytical Studies

Nian-Sheng and Cheng (2012)

In 2012 Nian-Sheng and Cheng proposed new formulations to parametrize the Drag Coefficient C_d for flows through an isolated cylinder and arrays of emergent cylinders.
In this work were considered only rigid circular stems as vegetation model. Many previous experimental studies were taken into account such as Cheng and Nguyen in 2011 [19], Tanino and Nepf in 2008 [70], James et al. in 2004 [35] as well as analitycal studies.
The objective was to investigate the flow dynamics such as flow separation and vortex shedding when an array of cilynders was considered. In particular the main challenge was to understand how the single-cylinder drag coefficient could be modified by the presence of a dense rod canopy. In order to represent the Drag Coefficient C_d for a wide range of Reynold's number and fit the experimental data an empirical formula for $C_{d,iso}$ was proposed (see equation 2.21). Figure 2.14 shows the perfect fitting of equation 2.21 with the experimental data.

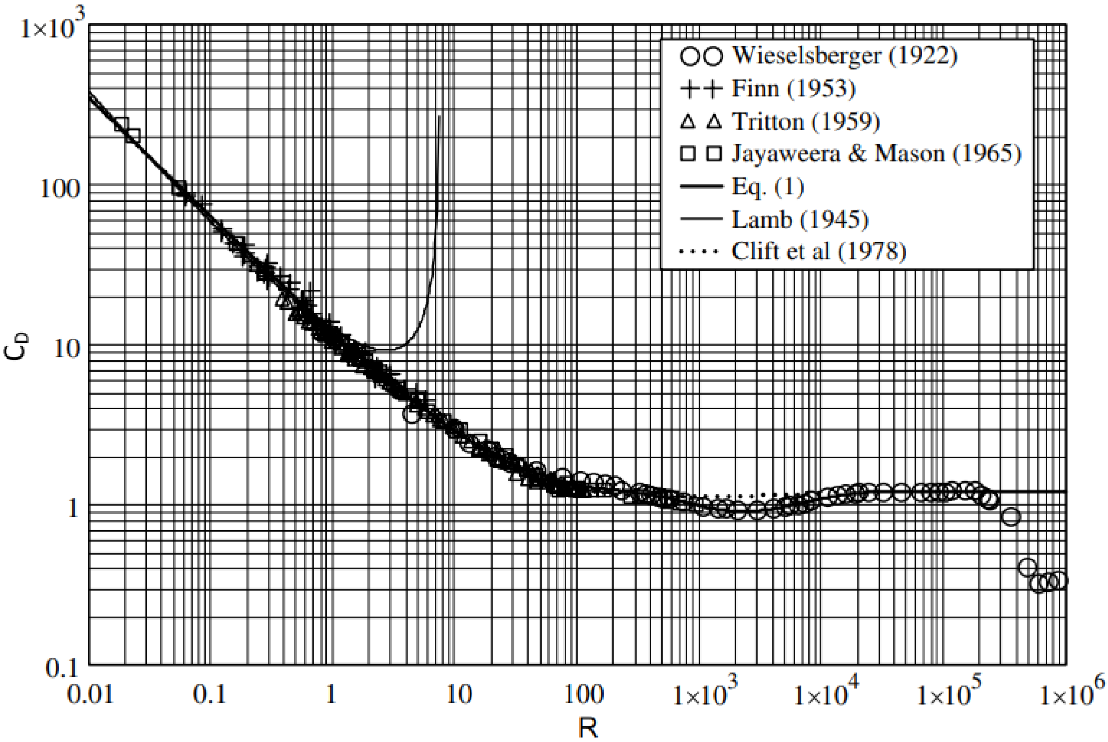

Figure 2.14. *Variation of the Drag Coefficient C_d with the cylinder Reynold's number for an isolated cylinder. Comparison between the experimental data and the formula proposed by Cheng and labeled as $Equation1$ in the figure.*

When an array of cylinders was considered (see figure 2.15) a new empirical formula for the Drag Coefficient was derived.

$$C_{da} = \frac{\pi}{2}\frac{1}{\lambda}\frac{gDS}{V_v^2}, \tag{2.27}$$

where g il the gravitational acceleration, S is the average energy slope of the flow, V_v is the velocity through the emergent vegetation and λ is the average solid fraction occupied by the stems. For a rare vegetation equation 2.27 yields to equation 2.21. The wide database used to evaluate equation 2.27 is summarized in figure 2.15.

Investigator	Number of datasets	Vegetation fraction, λ	Stem arrangement	Stem diameter, d (mm)	$R_a(V_v d/\nu)$
Ishikawa et al. (2000)	30	0.00314–0.0126	Staggered	4; 6.4	910–4,570
James et al. (2004)	23	0.0035–0.0314	Staggered	5	240–870
Liu et al. (2008)	9	0.0031–0.0160	Staggered; in-line	6.35	1,280–2,200
Tanino and Nepf (2008)	116	0.090–0.35	Random	6.4	25–690
Ferreira et al. (2009)	2	0.022–0.038	Random	11	1,190–1,450
Tanino and Nepf (personal communication, 2010)	73	0.031–0.056	Staggered	6.4	110–830
Cheng and Nguyen (2011)	143	0.0043–0.119	Staggered	3.2; 6.6; 8.3	200–1,540

Figure 2.15. *Summary of previously collected experimental data.*

The next figure shows the variation of C_{da} with the cylinder Reynold's number R_a. When the average solid fraction occupied by the stems λ is small, C_{da} and R_a merge to $C_{d,iso}$ and R_e as expected. The curves plotted were calculated by using equation 2.27 for $\lambda = 0.03$, $\lambda = 0.1$, $\lambda = 0.2$, $\lambda = 0.3$ and $\lambda = 0.4$. The diameter considered for the rods was $D = 0.006m$. Also represented in figure 2.16 are the experimental data showed in figure 2.15.

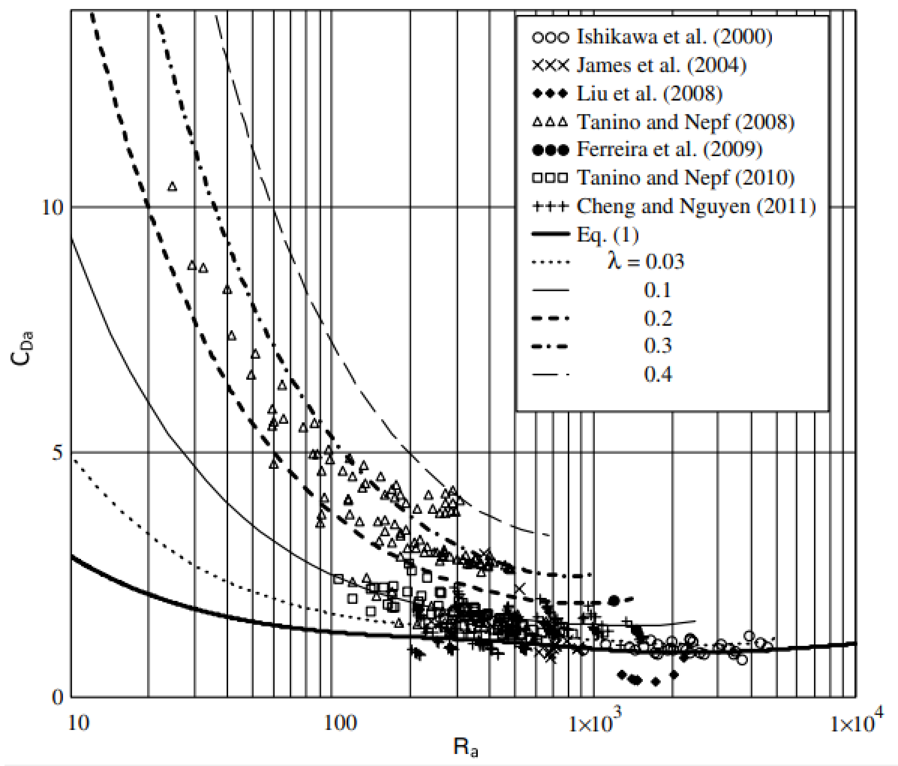

Figure 2.16. *Variation of Drag Coefficient C_{da} with Reynold's number R_a.*

It is shown that the formula proposed by Cheng well fits the experimental data. Moreover it confirmed that the Drag Coefficient increases with increasing rods density.

Etminan (2017)

One of the most relevant study about the influence of vegetation canopies on rivers, streams and floodplains was carried out by Etminan in 2017.
As demonstrated by previous publications, the flow structure is influenced by the drag forces exerted by the vegetation. LES were performed in order to study the role played by the three mechanisms able to modify the drag, such as blockage, sheltering and early separation. In the

LES the spatially-filtered, three-dimensional Navier-Stokes Equations are solved numerically. The equations in tensor notation are:

$$\frac{\partial \overline{u}_i}{\partial x_i} = 0, \tag{2.28}$$

$$\frac{\partial \overline{u}_i}{\partial t} + \frac{\partial}{\partial x_j}(\overline{u}_j \overline{u}_i) = -\frac{1}{\rho}\frac{\partial \overline{p}}{\partial x_i} + 2\nu \frac{\partial^2 \overline{S}_{ij}}{\partial x_i \partial x_j} - \frac{\partial \tau_{ij}}{\partial x_j}, \tag{2.29}$$

where i and j are set from 1 to 3. The velocities u_1 and u_2 are in the streamwise direction, ν is the kinematic viscosity and p is the pressure. S_{ij} has the following form:

$$\overline{S}_{ij} = (\frac{\partial \overline{u}_i}{\partial x_j} + \frac{\partial \overline{u}_j}{\partial x_i}). \tag{2.30}$$

The turbulence was modeled with a standard Smagorinsky closure:

$$\overline{\tau}_{ij} = -2\nu_t \overline{S}_{ij} + \frac{2}{3}k\delta_{ij}. \tag{2.31}$$

The simulations were conducted in OpenFOAM version 2.3.0 and the incompressible solver pimpleFoam was used. The model vegetation chose was a staggered array of cylinders with a spacing S (see figure 2.17).

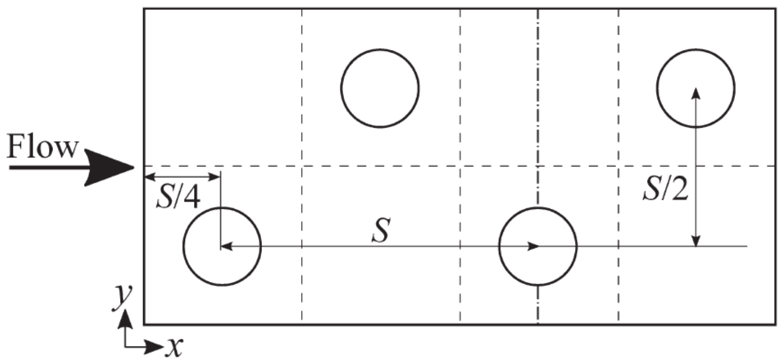

Figure 2.17. *Cylinders arrangement.*

In this study six array densities were explored ($\lambda = 0.016$, $\lambda = 0.04$, $\lambda = 0.08$, $\lambda = 0.012$, $\lambda = 0.020$ and $\lambda = 0.25$). The grid chose for the simulation consisted in four sets of cells. Each set was represented by an O-grid block around the cylinder and an H-grid block in the far field. The simulations were performed for four Reynold's numbers $R_{ep} = U_p d/\nu$ as shown in figure 2.18.

Table 1. The Model Canopies and Grid Configurations Employed

Density, λ	Spacing, S/d	Grid Points in H-Grid, $m_x \times m_y \times m_z \times m_{set}$	Grid Points in O-Grid, $m_\theta \times m_r \times m_z \times m_{set}$	Total Number of Grid Points	$Re_p = U_p d/\nu$
0.016	10	$82 \times 82 \times 148 \times 4$	$(82 \times 4) \times 70 \times 148 \times 4$	17,572,928	500, 1,340
0.04	6.3	$80 \times 80 \times 140 \times 4$	$(80 \times 4) \times 70 \times 140 \times 4$	16,128,000	200, 500, 1,000, 1,340
0.08	4.4	$70 \times 70 \times 140 \times 4$	$(70 \times 4) \times 55 \times 140 \times 4$	11,368,000	200, 500, 1,000, 1,340
0.12	3.6	$62 \times 62 \times 140 \times 4$	$(62 \times 4) \times 45 \times 140 \times 4$	8,402,240	200, 500, 1,000, 1,340
0.20	2.8	$50 \times 50 \times 140 \times 4$	$(50 \times 4) \times 25 \times 140 \times 4$	4,200,000	200, 500, 1,000, 1,340
0.25	2.5	$42 \times 42 \times 140 \times 4$	$(42 \times 4) \times 20 \times 140 \times 4$	2,869,440	500, 1,340

Figure 2.18. *LES and model configuration.*

The simulation were carried out by considering four velocities to which corresponded for Reynold's number and Drag Coefficient (see figure 2.19). U_b is the bulk velocity, U_p is the pore velocity, they are related by $U_p = U_b/(1-\lambda)$. U_s is the velocity at the boundary of the wake region and U_c is the constricted cross-section velocity. U_b, U_s and U_c relation is expressed by the following formula:

$$U_c = \frac{1-\lambda}{1-\sqrt{\frac{2\lambda}{\pi}}} U_p \equiv \frac{1}{1-\sqrt{\frac{2\lambda}{\pi}}} U_b. \tag{2.32}$$

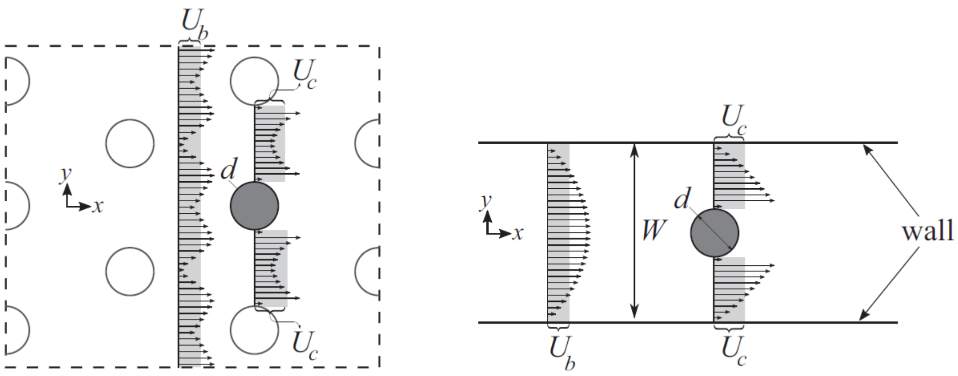

Reference Velocity	Symbol	Reynolds Number	Drag Coefficient
Pore velocity	U_p	Re_p	$C_{d,p}$
Bulk velocity	U_b	Re_b	$C_{d,b}$
Separation velocity	U_s	Re_s	$C_{d,s}$
Constricted cross-section velocity	U_c	Re_c	$C_{d,c}$

Figure 2.19. *Representation of the bulk velocity U_b, constricted velocity U_c and pore velocity U_p. Reference velocity used in the study and correspondent Reynold's Numbers and Drag Coefficients.*

The next figure shows the Drag Coefficients Cd_c and Cd_p calculated by taking into account the constricted velocity U_c and the pore velocity U_p.

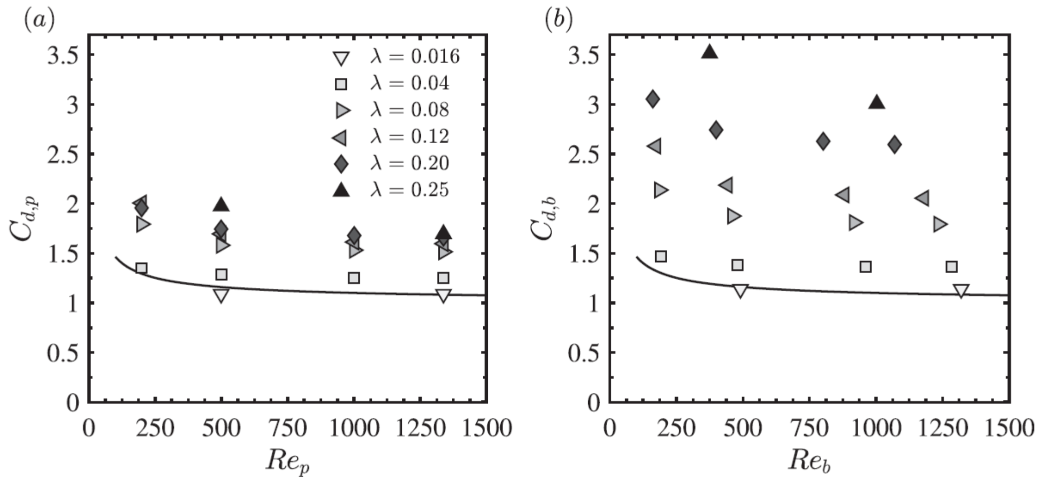

Figure 2.20. *Drag Coefficients representation in function of the pore velocity U_p and the constricted velocity U_c.*

The $C_{d,c}$ values collapse onto the same curve while the $C_{d,p}$ values seem to be more spread around a single curve. This pointed out that the constricted velocity U_c was the one able to explain better the drag exerted by a rod canopy in the range of Reynold's number considered. Hence Etminan proposed a Drag Coefficient $C_{d,c}$ formulation as follow:

$$C_{d,c} = 1 + 10Re_c^{-2/3}. \tag{2.33}$$

3. Theory

The problem treated in this thesis is the instantaneous collapse of a dam in a long sloping prismatic channel covered by a dense rod canopy chosen as a model vegetation. The goal is to describe the water level $h(x,t)$ downstream from the dam for various S_o and initial water level H_o behind the dam.
The outflow subsequent the collapse of the Dam is a '*non-uniform flow*' and, in fact, can be represented through the SVE which are derived from the Navier-Stokes Equations assuming (i) constant water density, (ii) the water depth h is small compared with other length scales such as the wave length of the water surface or the channel width, and (iii) the pressure distribution is hydrostatic so that vertical acceleration can be ignored, and (iv) the bed-slope is not too steep [21]. With these conditions the SVE can be written as follows:

$$\frac{\partial A}{\partial t} + \frac{\partial Q}{\partial x} = 0, \tag{3.1}$$

$$\frac{\partial Q}{\partial t} + \frac{\partial}{\partial x}\frac{Q^2}{A} + gA\left(\frac{\partial h}{\partial x} - S_o\right) + gAS_f = 0. \tag{3.2}$$

Where A is the cross-section area, Q is the discharge flow, x is the spatial coordinate, t is the temporal coordinate, g is the gravitational acceleration, h is the water level, S_f is the Friction Slope and S_o is the Bed Slope. These equations describe the temporal and spatial change of the physical quantities representing the unsteady flow. The first equation is known as Continuity Equation, it represents the '*Law of Conservation of Mass*', which means that the inflow, outflow and the variation of mass in a control volume are balanced. The second equation is the Momentum Equation, it is an extension of Newton's second law applied to fluid dynamics. Due to the fact that the width of the facility is constant, the cross-section area can be expressed by the following formula:

$$A = bh. \tag{3.3}$$

The SVE can be rearranged as follows:

$$\frac{\partial h}{\partial t} + h\frac{\partial v}{\partial x} + v\frac{\partial h}{\partial x} = 0, \tag{3.4}$$

$$\frac{1}{g}\frac{\partial v}{\partial t} + \frac{v}{g}\frac{\partial v}{\partial x} + \frac{\partial h}{\partial x} = S_o - S_f. \tag{3.5}$$

Where h is the water level, x is the spatial coordinate, t is the temporal coordinate, S_f is the Friction Slope, S_o is the Bed Slope, v is the mean velocity and g is the gravitational acceleration. The second formula takes the form of the Dynamic Wave Equation.
In order to describe the water level $h(x,t)$ downstream from the dam play an important role the choice of how the Friction Slope S_f is modeled. In almost all applications, the resistance law used to describe S_f is based on a locally steady and uniform flow [8, 49]. Unsurprisingly, Manning's formula [53] with a constant roughness coefficient n remains popular given the

voluminous literature on n and its connection to the so-called Strickler scaling [10] or momentum roughness height [40]. The flow velocity in an open channel can be described by Chezy's formula:

$$U = \frac{AR_h^{1/6}}{n}\sqrt{R_h S_o}, \tag{3.6}$$

where S_o is the bottom slope.
In a steady and uniform flow the EGL slope coincides with the bottom slope resulting in $S_o = S_f$. Such approximation yields an S_f given by

$$S_f = \left(\frac{2gn^2}{R_h^{4/3}}\right)\frac{U^2}{2g}, \tag{3.7}$$

where R_h is the hydraulic radius.
When the channel cover is densely vegetated, there is consensus that such a closure may be too simple even for steady-uniform flow thereby necessitating further inquiry into the explicit inclusion of a distributed drag force by vegetation elements at high Reynolds numbers [57, 77, 50, 26, 33, 62, 29, 46, 56, 24]. Equation 3.7 assumes that frictional losses occur through bed and side stresses (i.e. R_h) rather than a distributed drag force that can be emergent or entirely submerged [62, 39, 56, 54]. The work here explores experimentally and numerically the effects of canopy drag on S_f for unsteady inertial flow over a rigid dense cylindrical vegetation covering a large flume base where the slope S_o is also varied. A number of formulations that have been proposed to link S_f to the vegetation drag coefficient C_d are also evaluated. These formulations have been shown to partly capture blockage, sheltering, angle of separation, among others [47, 37, 12, 35, 7, 70, 22, 18, 43, 45, 80, 17, 15, 74, 75, 24].
Hence the theory section will be organized as follows: the case where $S_f = 0$ is first reviewed as this case sets the choice of the normalizing variables for the data analysis and model runs. Next, various formulations linking S_f to the drag by a rod canopy are provided. This representation for the drag force is then contrasted to a Manning type formulation to highlight plausible effects on the shape of $h(x,t)$ in the advancing wave front region.

3.1 The Frictionless Case and Choice of Normalizing Variables

Since the work here considers the effects of vegetation on S_f, it is instructive to establish a reference solution for an ideal flow whereby $S_f \approx 0$. Although this ideal case implies no energy losses along the channel, it allowed the foundation of the Ritter Solution [65] which represents a milestone of the dam-break scenario. Ritter, assuming a horizontal channel and a initially dry ground ahead of the dam, proposed the following solution to equations 3.1 and 3.2

$$U(x,t) = \frac{2}{3}\left(\frac{x}{t} + \sqrt{H_o g}\right), \tag{3.8}$$

and

$$h(x,t) = \frac{1}{9g}\left(2\sqrt{H_o g} - \frac{x}{t}\right)^2, \tag{3.9}$$

where H_o is the water level at rest just behind the dam.
Equations 3.8 and 3.9 can also be expressed in dimensionless form as

$$h_n = \frac{1}{9}\left(2 - u_n\right)^2, \tag{3.10}$$

where $h_n = h/H_o$ is the dimensionless water depth, $u_n = (x/t)(H_o g)^{-1/2}$ is the dimensionless wave speed, $t_n = t(H_o/g)^{-1/2}$ is dimensionless time, and $x_n = x/H_o$ is dimensionless

longitudinal position downstream from the dam.
This fundamental relation shows that in the case of a frictionless channel the dimensionless water level h_n and the dimensionless wave speed u_n are linked by a parabolic relation. This means that for a fixed h_n corresponds a unique u_n. Ritter's solution to equations 3.1 and 3.2 was extended to the case of a sloping channel [14, 49] and can be expressed as follows

$$U(x,t) = \frac{2}{3}\left(\frac{x}{t} + \sqrt{H_o g} + S_o g t\right), \tag{3.11}$$

and

$$h(x,t) = \frac{1}{9g}\left(2\sqrt{H_o g} - \frac{x}{t} + \frac{1}{2}S_o g t\right)^2, \tag{3.12}$$

where H_o is the water level at rest just behind the dam and the initial conditions is a dry stream bed.

3.2 Canopy Drag and Friction Slope

To arrive at an expression resembling equation 3.7 to be used in the SVE, a locally steady-uniform flow within or above the dense canopy is considered. With this assumption a local balance between the flow driving forces and the drag forces is required:

$$\rho g S_f V_w = C_d A_v \rho \frac{U^2}{2g} + B dx\,(1-\phi_v)\,\tau_{ground} + 2H dx \tau_{wall} g, \tag{3.13}$$

where τ_{ground} is the ground friction per unit area, τ_{wall} is the side friction, B is the width of the channel and dx is the infinitesimal length of channel where the initial conditions are respected. The ground and side friction contribution to the total stress are ignored relative to the distributed drag force acting on the flow by the canopy elements [74]. Equation 3.13 yields to:

$$\rho g S_f V_w = C_d A_v \rho \frac{U^2}{2g}, \tag{3.14}$$

where ρ is the density of water, V_w is the volume of water, A_v is the frontal area of the vegetation contained in V_w and C_d is the drag coefficient. It is convenient to examine the force balance per unit ground area so that $V_w = h(1-\alpha_s\phi_v)$ and $A_v = mDh\alpha_s$, where ϕ_v is the solid volume fraction per ground area determined by $\phi_v = m\pi D^2/4$, m is the rod density determined from the number of rods per unit ground area, and α_s depends on whether the vegetation is emergent ($h/h_c > 1$) or submerged (i.e. $h/h_c < 1$). For an emergent canopy , $\alpha_s = 1$ whereas for a submerged canopy, $\alpha_s = h_c/h$ and varies with h. The S_f can now be directly determined from equation 3.14 as

$$S_f = \left(\frac{C_d m D \alpha_s}{1-\alpha_s\phi_v}\right)\frac{U^2}{2g}. \tag{3.15}$$

In virtually, for all studies dealing with shallow flow within vegetation, C_d is assumed to vary with a Reynolds number $Re = VL/\nu$, where V and L are characteristic velocity and length scales respectively, and ν is the kinematic viscosity of water. In terms of possible choices for L, the rod diameter or spacing, and the hydraulic radius (or water level) have been proposed. Likewise, in terms of possible choices for V, bulk velocity, pore-scale velocity or a variant on it such as the constricted velocity, and separation velocity are commonly employed. Models for C_d that vary V instead of L are now reviewed.

3.2.1 The Isolated Cylinder Case

For an isolated cylinder, the local $C_{d,iso}$ can be determined from the bulk velocity and rod diameter by forming an element Reynolds number $Re_d = UD/\nu$. In this case the variation of drag is related to the flow separation that occurs when the water hits the rods. An expression for $C_{d,iso}$ that describes data for isolated cylinders for $Re_d < 10^5$ is given by [16, 74]

$$C_{d,iso} = 11(Re_d)^{-0.75} + 0.9\Gamma_1 (Re_d) + 1.2\Gamma_2 (Re_d), \tag{3.16}$$

where

$$\Gamma_1 (Re_d) = 1 - \exp\left(-\frac{1000}{Re_d}\right), \tag{3.17}$$

and

$$\Gamma_2 (Re_d) = 1 - \exp\left[-\left(\frac{Re_d}{4500}\right)^{0.7}\right]. \tag{3.18}$$

This expression assumes that the drag from each cylinder operates in isolation assuming the same U acts upon all cylinders which means no shelter or blockage.

3.2.2 The Array of Cylinder Case

Several studies found that C_d in a vegetated array (hereafter referred to as $C_{d,a}$) differs from $C_{d,iso}$ and these variations depend on the Reynolds number and ϕ_v. At a given Re_d, increasing vegetation density (or ϕ_v) appears to initially increase C_d [70, 69] and then to decrease it [57, 51] for emergent canopies [24]. Such adjustment was partly accommodated by an empirical formulation for $C_{d,a}$ derived from a large synthesis of experiments on emergent vegetation and is given as [18]

$$C_{d,a} = \frac{50}{Re_v} + 0.7\left[1 - \exp\left(-\frac{Re_v}{15000}\right)\right]. \tag{3.19}$$

The linkage between the vegetation-array and a stem related Reynolds number is

$$Re_v = \frac{\pi(1-\phi_v)}{4\phi_v} Re_d. \tag{3.20}$$

Once again, this linkage allows for direct comparisons between $C_{d,iso}$ and $C_{d,a}$ for a set ϕ_v.

3.2.3 The Staggered Canopy Case

For a staggered cylindrical canopy, [24] compared C_d for various Reynolds numbers definitions by using differing characteristic velocity scales but maintaining $L = D$. The aforementioned work showed that typical C_d formulation for a single cylinder case can still be employed when using a constriction velocity U_c as the reference V to form $Re_s = U_c D/\nu$. Their resulting expression, applicable for $Re_s < 6000$, can be summarized as

$$C_{d,s} = 1 + 10 Re_s^{-2/3}, \tag{3.21}$$

where $Re_s = U_c D/\nu$, and U_c, the constriction velocity imposed by the vegetation, is related to U through the conservation of mass using

$$U_c = \frac{1}{1 - \sqrt{\frac{2\lambda}{\pi}}} U, \tag{3.22}$$

where $\lambda = (\pi D^2/4)/(0.5 S_s^2)$ is the volume fraction for a staggered cylindrical array, and S_s is the rod spacing along the flow. For uniformly spaced vegetation, $\phi_v = \lambda$ but for a staggered array, the two quantities differ because the lateral spacing of rods differ from the longitudinal spacing. Using the staggered configuration in [24], $\lambda = (1/2)\sqrt{3}\phi_v$. Equation 3.22 suggests that $Re_s = (1 - \sqrt{2\lambda/\pi})^{-1} Re_d$ given that both utilize $L = D$ in their definition of Re. In the limit of large $Re_s (> 5000)$, $C_{d,s} \to 1$ and may be treated as a constant independent of Re.

3.2.4 Blockage and Sheltering Effects on C_d

Because $C_{d,iso}$ ignores sheltering and blockage, it is convenient to compare the aforementioned equations for C_d (isolated, array and staggered) to assess the Re_d range where sheltering ($C_d < C_{d,iso}$) and blockage ($C_d > C_{d,iso}$) are anticipated to dominate. Sheltering indicates that some vegetation elements are located in the wake region of the upstream elements [63], resulting in a lower velocity than their upstream counterparts and generate a lower drag compared with the isolated cylinder case. Delayed separation can be explained by the enhancement of the mean separation angle that is larger than that for the isolated cylinder, resulting in a decreasing drag coefficient compared with the isolated cylinder [24]. Both sheltering and delayed separation reduce C_d when compared to the isolated cylinder case. Blockage effects, which lead to local increases in C_d, are explained by two main factors [24]: (i) the velocity between cylinders is enhanced by the presence of vegetation; and (ii) wake pressure increases drag [78].

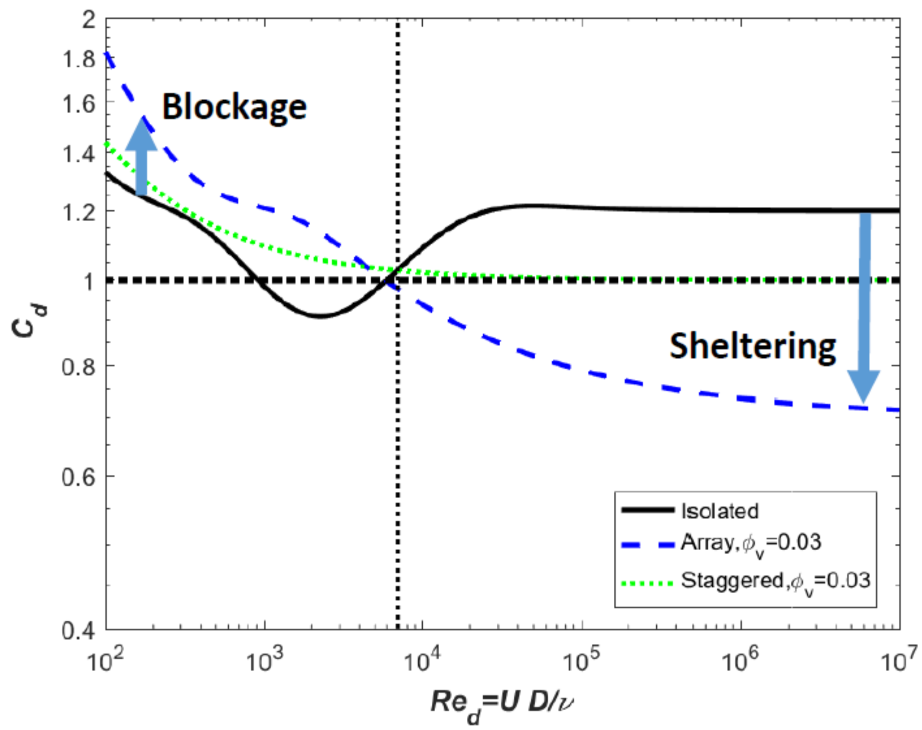

Figure 3.1. *A comparison between C_d as a function of $Re_d = UD/\nu$ for an isolated cylinder (i.e. equation 3.16), an array (i.e. equation 3.19) of cylinders [18] with $\phi_v = 0.03$ (the experiment here), and staggered (i.e. equation 3.21) cylinders [24] with $\lambda = (1/2)\sqrt{3}\phi_v$. At $Re_d = 0.7 \times 10^4$, the array and staggered C_d models suggest a switch from 'blockage' to 'sheltering' with increasing Re_d. Also, for $Re_d > \times 10^5$, the C_d models become weakly dependent on Re_d.*

The expressions for $C_{d,a}$ and $C_{d,s}$ are compared to $C_{d,iso}$ in Figure 3.1 for $\phi_v = 0.03$ corresponding to the flume experiments to be discussed. This comparison is enabled by the fact that Re_v and Re_s have been related to Re_d once ϕ_v or λ are specified for a given rod density (m or S_s). Roughly, when $Re_d > 0.7 \times 10^4$, $C_{d,a}$ and $C_{d,s}$ are reduced when compared to $C_{d,iso}$

suggesting that sheltering dominates. Conversely, when $100 < Re_d < 0.5 \times 10^4$, both $C_{d,a}$ and $C_{d,s}$ exceed $C_{d,iso}$ suggesting that blockage dominates. All three formulations agree that for large Re_d (i.e. $Re_d > \times 10^5$), C_d becomes weakly dependent on Re_d or almost entirely independent of Re_d altogether. The operational Re_d for the flume experiments exceed 0.5×10^4 in the vicinity of the advancing wave front.

3.3 Wall friction versus distributed drag force: The advancing front region

The water level shape of an advancing wavefront for a vegetated canopy is now contrasted to conventional Manning (or wall friction) representation of S_f using a simplified SVE. The SVE simplifications to be employed here are common to all analytical approaches describing the advancing wavefront. What is different here is the link between S_f and $(U^2)/(2g)$. Within the wavefront region, the front speed is assumed to be roughly constant so that $\partial U/\partial t$ and $\partial U/\partial x$ are small relative to the remaining terms in the SVE [14]. Also, the simplest case of a flat channel ($S_o = 0$) is considered for analytical foresight only. For these simplifications, the SVE reduces to its steady-non inertial (diffusive wave) version given by

$$g\left(\frac{\partial h}{\partial x} + S_f\right) = 0, \tag{3.23}$$

and the continuity equation simplifies to

$$\frac{\partial h}{\partial t} + U\frac{\partial h}{\partial x} = 0. \tag{3.24}$$

At very high Re_d to be expected following a dam-break, C_d is likely to be dominated by sheltering and becomes weakly dependent on Re_d as shown in Figure 4.10. Hence, to a leading order in equation 3.15, C_d may be treated as a constant with a numerical value that is smaller than $C_{d,iso}$ at high Re_d. Hence, the reduced SVE yields

$$U = \sqrt{-\frac{2g(1-\phi_v)}{C_d m D}\frac{\partial h}{\partial x}}, \tag{3.25}$$

which upon insertion into the reduced continuity equation (i.e. equation 3.24) and solving the corresponding partial differential equation for h yields

$$h(x,t) = C_1 + C_2 t - \left[C_2\sqrt{\frac{C_d m D}{2g(1-\phi_v)}}\right]^{2/3} x. \tag{3.26}$$

The C_1 and C_2 are integration constants to be determined from initial and boundary conditions or other constraints such as conservation of water mass or asymptotic matching to a solution near the dam location. Hence, the precise value of C_1 and C_2 vary with the specifics of the dam-channel setup. Hovewever, main finding here that for a constant C_d, $h(x,t)$ is linear in x with a slope that depends on the $(C_d m D)/(1-\phi_v)$ in the wave-front region is independent of C_1 and C_2. If the same analysis is repeated with equation 3.7 and a constant n instead of a constant C_d, the resulting U is given by

$$U = \sqrt{\frac{h^{4/3}}{n^2}\frac{\partial h}{\partial x}}, \tag{3.27}$$

(i.e. non-linear in h unless $\partial h/\partial x$ scales with $h^{-4/3}$ to ensure constant U) and the general solution of the reduced continuity equation (i.e. equation 3.24) is now given by

$$h(x,t) = \left[\frac{7}{3}\frac{(t + A_1 x + A_2)}{A_1^3} n^2\right]^{3/7} . \tag{3.28}$$

Again, A_1 and A_2 are integration constants to be determined similar to C_1 and C_2. Upon inspecting the two general solutions in equations 3.28 and 3.26, differences between constant n and constant C_d (expected to prevail at high Re_d) become evident. For a constant C_d, h scales linearly with x whereas h scales as a power-law with a sub-unity exponent (i.e. $x^{3/7}$) for the constant n near the advancing wavefront. Numerical solution to the full SVE confirm these differences and are to be discussed in comparison with experiments proposed here.

4. Experiments

4.1 Flood wave channel

The experiments were conducted using a flood wave channel situated at the Giorgio Bidone hydraulics Laboratory in Politecnico di Torino, Italy. The 11.6m long prismatic channel has a rectangular cross-section that is 0.5m (=B) wide and sides that are 0.6m in height. The smooth concrete channel bottom is elevated 1.27m from the ground floor. The channel sides are made of glass to permit optical access. The glass sides are enforced using a steel structure. A mechanical wheel allows the channel to rotate around a pin that can be switched so as to vary S_o from 0% to 3%. The channel is filled directly with water from below by a pipe and the outflow from the channel discharges into a tank after passing over a rectangular weir. The vegetation immediately ahead of the dam is composed of an array of a polymeric resin cylinders. The cylinders are fixed on six plastic boards 15cm wide and 1.75m long. In order to fill all the cross-section, the boards are positioned side-by-side three at a times for a total length of 3.5m. The panels are attached to the channel bottom using silicon. This attachment allowed the rods not to move during the runs. The cylinders comprising the rod canopy are rigid with uniform diameter D=0.006m and height h_c=0.10m. The rods are arranged in a staggered configuration with a spacing of 0.035m transversely and longitudinally, while the distance to the diagonal is 0.0175m. This arrangement resulted in a density $m = 1206$ rods m^{-2}.
A wooden cofferdam with an instantaneous opening is used to represent the dam-break scenario. The wood is waterproofed as this treatment allows the wood not to deteriorate during the lengthy experimental duration. The cofferdam is fixed on an aluminum double T-support and is free to move upward and downward through a vertical railing structure sustained by the steel body of the facility. A Pneumatic cylinder is fixed on top of the vertical structure and powered by a compressor located on the floor. The compressor directs an 11bar pressure to the pneumatic cylinder forcing a disc to move upward quickly. The disc is connected to the piston rod, which in turn is fixed to the framework of the cofferdam. This system uplifts the cofferdam at a speed of 0.86 m s^{-1} thereby mimicking the instantaneous release of water into the flume following dam break.

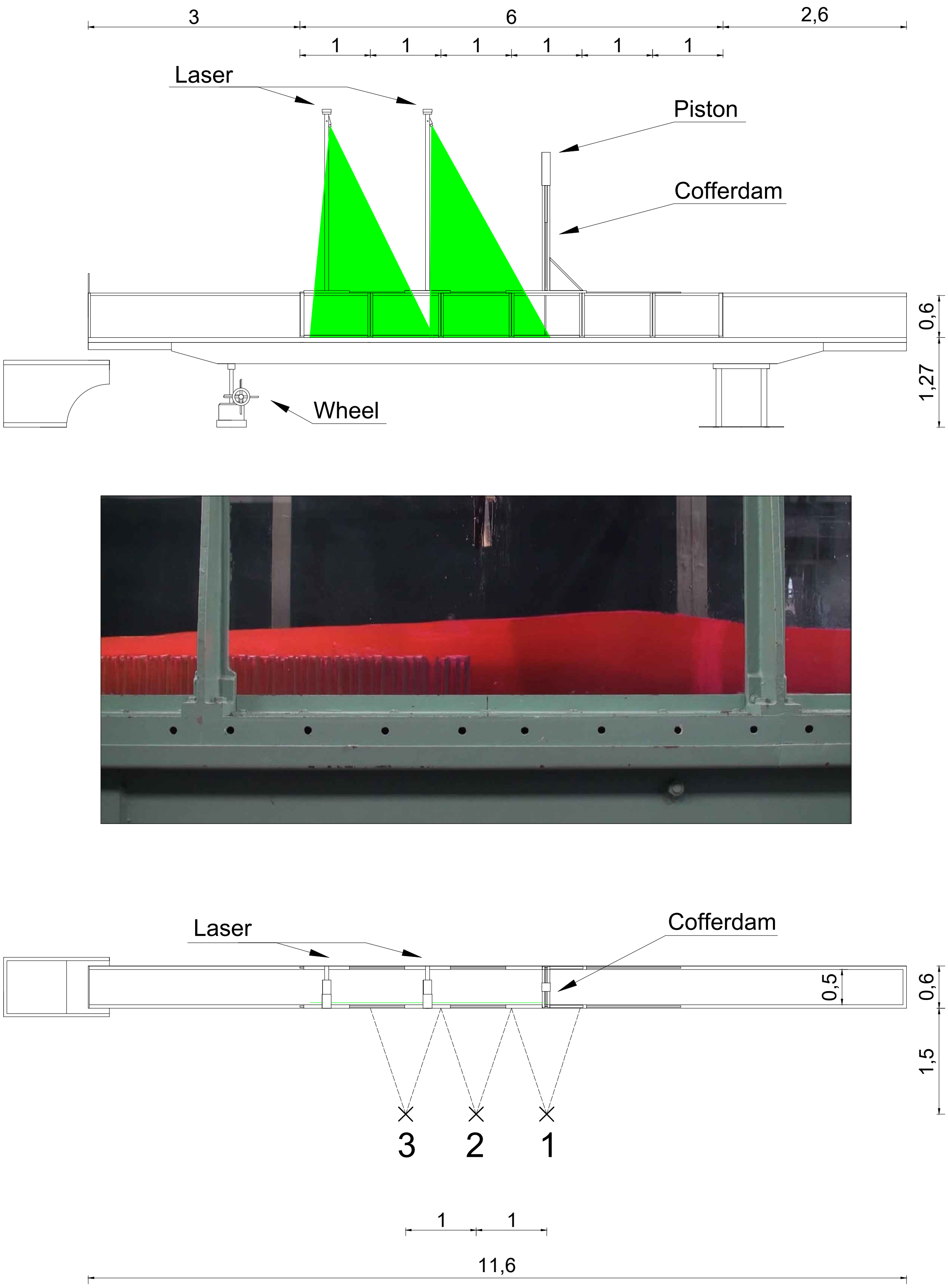

Figure 4.1. *Overview and later view of the experimental setup showing the channel, the cameras, the dam and the dyed water behind the dam, and a sample image used to determine the water surface profile at one instant in time shortly after the dam break.*

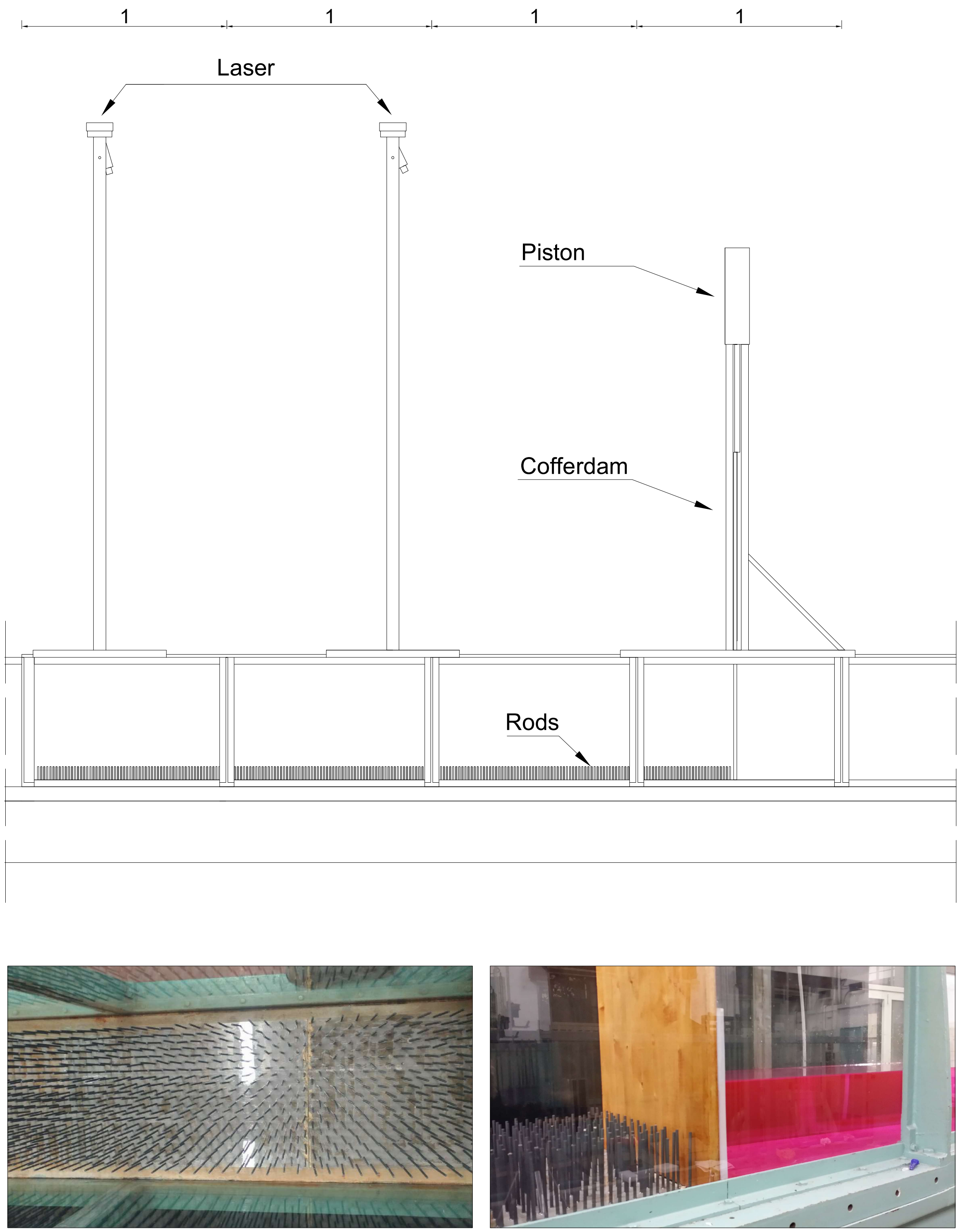

Figure 4.2. *Detailed later view of the experimental setup, sample image of the rods canopy from above and image the setup ready for a run test.*

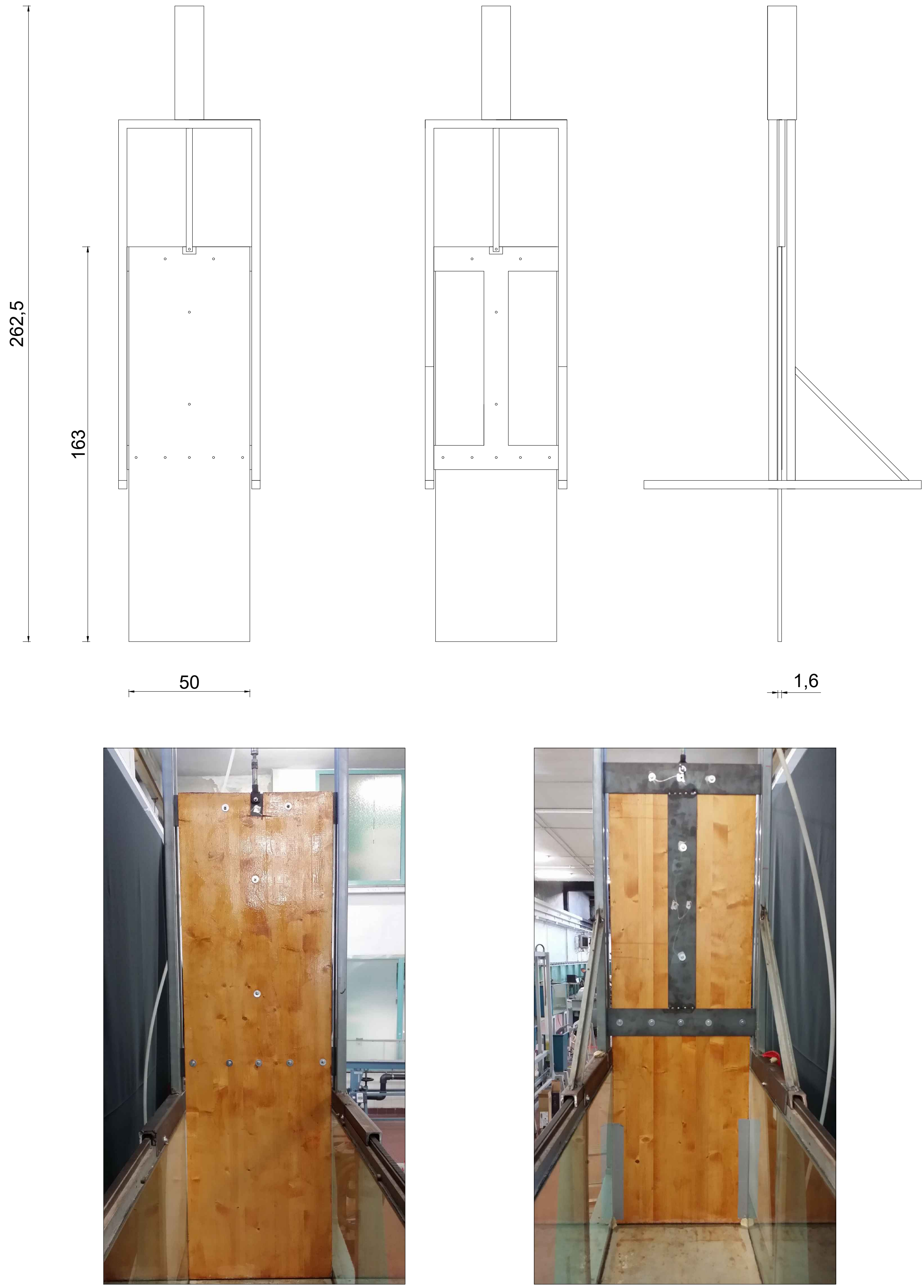

Figure 4.3. *Frontal, rear and lateral vision of the cofferdam.*

4.2 Water Level Measuring Equipment

The main variables measured here are water level $h(x,t)$ variations along the channel at regular temporal intervals. In order to get the water heights without influencing the flow three Sony Handycam HDR-XR500 were used. Each camera is equipped with a 3-3/16" widescreen touchpanel LCD, a Sony's premium G Lens and a remote control to start all the cameras concurrently. This model is able to record high-definition AVCHD video and store it in a 120GB hard disk. The resolution used in the experiment is the best available that is 1920x1080, which at the same time allows to get 29,97 frames per second.
The cameras are fixed on a horizontal bar at a distance of 1m from each other. They are aligned with the bottom of the channel when the slope is 0%. The distance between the cameras and the glasses is 1.5m, which grant the camera to record a movie of the full glass in front of it. It follows that the three cameras consent to cover a length of 3m starting from 0.5m upstream of the dam as it is shown in figure 4.5.

Figure 4.4. *Sony Handycam HDR-XR500.*

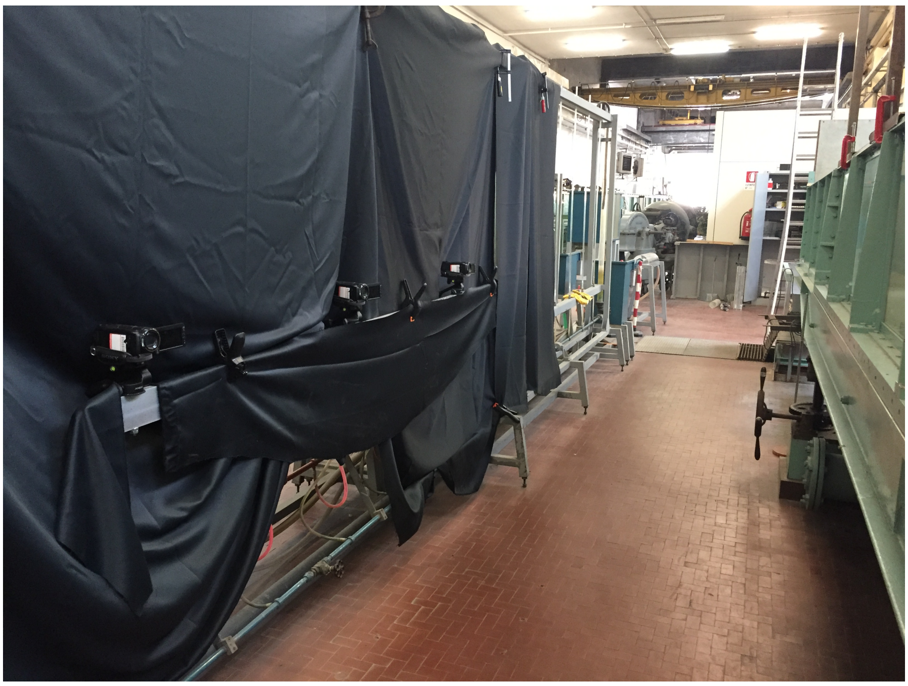

Figure 4.5. *Cameras Setup.*

To avoid any kind of reflection coming from the windows of the laboratory, two black cloths have been placed behind the cameras and behind the flood wave channel. As stated above, the motivation of using cameras to get movies of the flow is to determine the water profile without flow interferences. Since water is transparent, it is difficult to automate the detection of the water surface profile from images without additional markers. That's why the water was mixed with Rhodamine. Rhodamine is a dye which becomes fluorescent and emits red light when being excited with light at a different wavelength, in particular by green light. The green light is emitted by two laser generators, with 200 mW power, fixed over the channel on two supports welded to the metallic frame of the facility. Each laser emits a narrow beam of green light which crosses a glass cylinder with a diameter of 3mm. When the light crosses the cylinder is refracted and generates a plane of light perpendicular to the bottom of the channel and with the same direction of the flow. During each experiment in fact the water is red colored and the laser generate a plane of light that gives to a longitudinal section of the water an orange color as shown in figure 4.6. The addition of such a dye enhances the imaging and automated detection of the water surface.

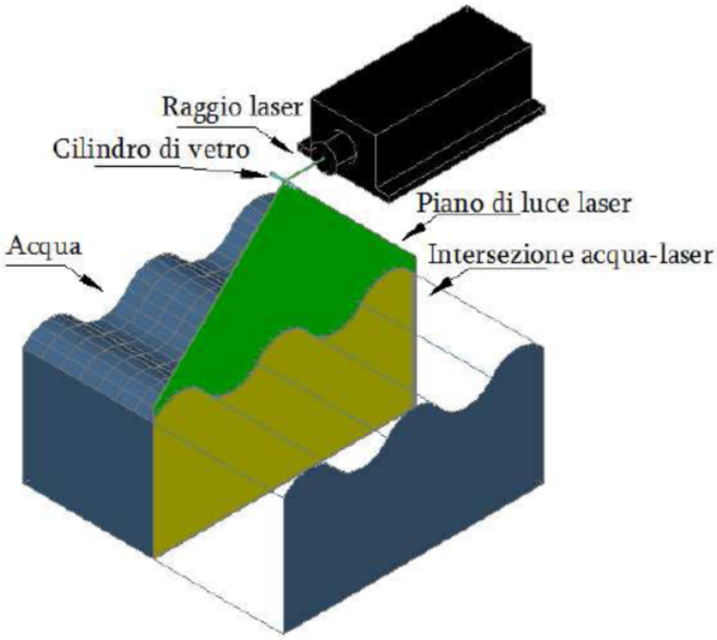

Figure 4.6. *Laser functioning.*

4.3 Run tests

The test runs were performed using four differing water levels behind the dam ($H_o = 0.15$m, 0.20m, 0.25m, 0.30m) and four differing bed slopes ($S_o = 0\%$, 1%, 2%, 3%) resulting in a total of 16 configurations. The experiment regarding the 0% slope were completed ten times for each water level allowing to obtain statistically robust data or rather not affected by outliers. The outcome of the analysis showed a low standard deviation between the different water profiles. This led to the decision to perform only 5 experiments per water level for the remaining slopes to a total of other sixty trials.

The trials were completed following a rigorous procedure according to a robust precision needed for the case in question. At first the gate is closed so that a reservoir is set up behind the dam. The reservoir is filled from below until the desired water level is reached. The water levels is measured by a hydrometer fixed on a glass panel of the facility. The water is then mixed with a precise amount of Rhodamine calculated in relation of the volume stored behind the dam. The goal is to reach a color that has same shade of red for each experiment. Once the wave channel is set the next step is to prepare the measuring equipment. The two lasers are started up by turning their activation key. The compressor, connected to the hydraulic piston, is in the mean time turned on with a special switch that allows it to get to the required 11bar pressure. The three cameras are turned on at the same time with a remote controller. The requirement of getting a precise water profile, which is obtainable only with a clear difference of color between the water and the background, led to perform the experiments only between 8a.m. and 6 p.m. and with the lights of the laboratory always turned on. The trial starts when the compressed air is pumped into the piston through a rubber pipe and ends when all the water is discharged. The movies, taken with three Sony Handycam HDR-XR500, recorded with a High Quality resolution and 29.97 frames per seconds, are analyzed with MATLAB. The analysis allows to transform the detected water level from pixel coordinates to metric coordinates thereby providing $h(x,t)$ for each run and all 16 configurations. Roughly each run lasted from 7s to 10s with the flood wave passing the imaged sections in 4s-5s.

4.4 Movies analysis

The subsequent step after the run tests is the movies analysis. The goal here is to obtain the pixel coordinates of the water surface starting from the movies taken by the cameras.
Each test run is recorded in high quality by three cameras and stored in a 120GB hard disk. First of all the movies are converted in MP4 format and cut to a length of 30 seconds. After that each movie is loaded into MATLAB where the video frames are extracted. The cameras record 29.97 frames per second. This number of frames is overabundant in the topic studied here. Due to this fact only one out of three frames are extracted resulting in a storing of about one image every 0.1 seconds.
The first movies examined are the ones with the 0% slope. The beginning of the time axis ($t = 0$) is set at the time when the cofferdam starts to move while the end is set 7.2 seconds after that moment resulting in a total of 81 frames. In the case of the others slopes (1%, 2% and 3%) the beginning of time is the same while the end is set at 10.8 seconds. It results in a bigger computation load represented by 121 frames.
In order to detect the water profile each image is analyzed separately. The digital images are represented by the combination of a discrete number of elementary unit called pixel. Each pixel is characterized by a variable luminosity intensity or rather a different color. Every color, according to the RGB coding, can be represented with the combination of the colors Red, Green and Blue. A color can be ideally defined by an infinity of color depths. In this case the Red, Blue and Green colors are defined by 8 bit each resulting in 256 tonalities for each color. The 8-bit system is the most common in the digital images storing. MATLAB stores every frame as a tridimensional matrix of dimension MxNx3, where M and N and are the number of pixels in the x and y direction and the third dimension represent the tonality of Red, Green and Blue.
Each image is analyzed by looking for the pixels forming the water surface. The MATLAB code, starting from the first pixel positioned in the upper left part of the picture, permits to move downwards in the same columns until the pixel of the water surface is found. The pixel belonging to the water surface is detected by setting a precise range of color. The choice of using Rhodamine to color the water and the laser to illuminate it reduces the quest to a unique shade of red. If the color of the pixel is inside a precise range of red then the point is saved as part of the profile and the research continues with the next column until all the horizontal and

vertical dimensions of the image are explored. This process is repeated for each frame.
This method is applied for each of the three cameras. The complete water surface profile, which takes into account all the three cameras, is assembled later once the profiles are all in metric coordinates.
Figures 4.7, 4.8 and 4.9 show how the laser and the Rhodamine are able to generate a color difference between the water and the black background. The pixels belonging to the water surface are detected and colored in green to show the millimetric precision of the code.

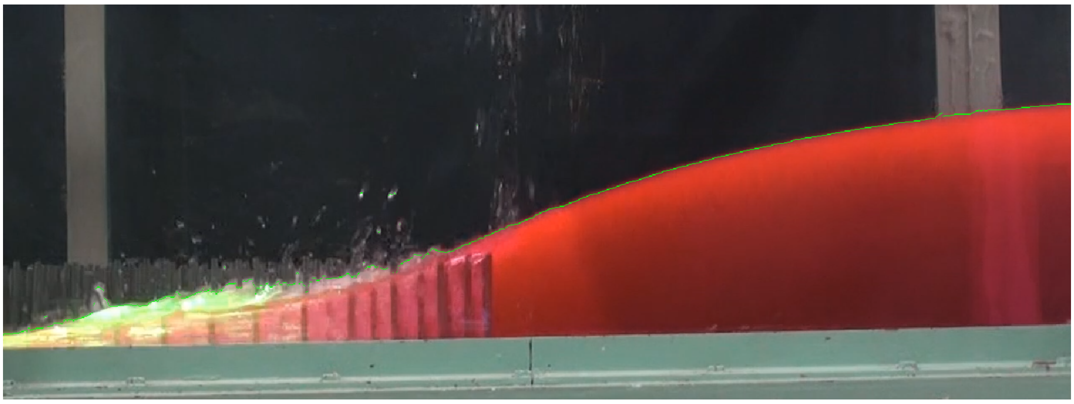

Figure 4.7. *Sample image used to determine the water surface profile for $H_o = 0.3m$, $So = 2\%$, $t = 0.5s$.*

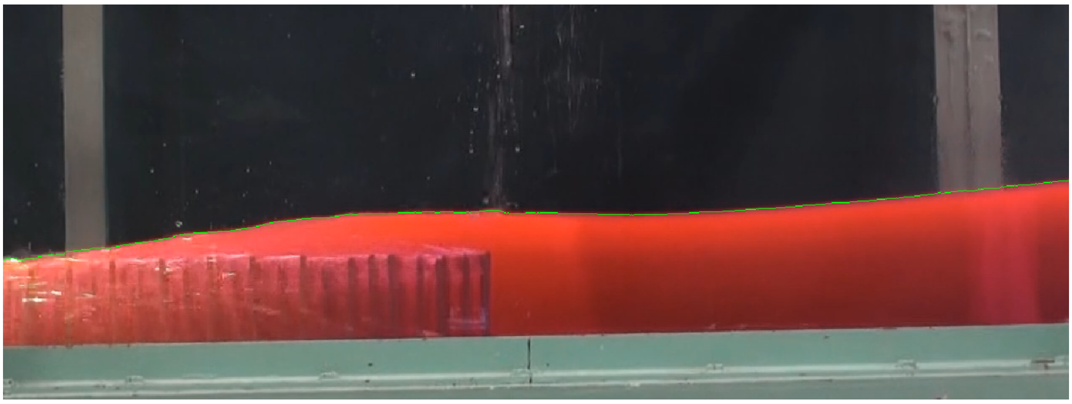

Figure 4.8. *Sample image used to determine the water surface profile for $H_o = 0.3m$, $So = 2\%$, $t = 1s$.*

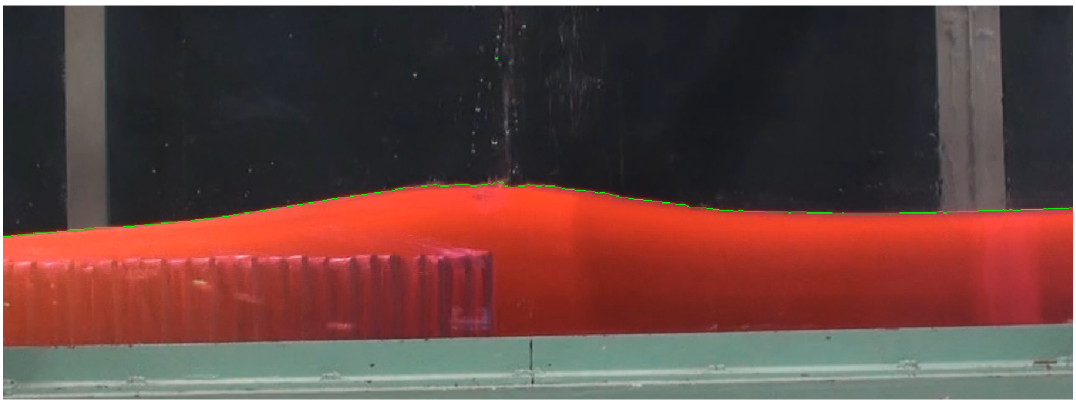

Figure 4.9. *Sample image used to determine the water surface profile for $H_o = 0.3m$, $So = 2\%$, $t = 1.5s$.*

4.5 Camera Calibration

The '*Camera Calibration*' is the process used to assess the Camera Parameters. The Camera Parameters are the criterions which allow to describe the features of a camera. They are divided in Extrinsic Parameters, Intrinsic Parameters and Lens Distorsion. The Intrinsic Parameters are seven and express the relation between geometric coordinates and pixel coordinates in the digital image produced. They are contained inside the "*Intrinsic Matrix*".

$$K = \begin{bmatrix} f_x & 0 & 0 \\ s & f_y & 0 \\ cx & cy & 1 \end{bmatrix}.$$

Where:
-F is the focal length, expressed in world units [mm];
-cx,cy are the pixel coordinates of the optical center;
-s_x, s_y are the number of pixels per world unit in the x and y direction respectively.
-fx=$F * sx$;
-fy=$F * sy$;
-s is the skew. If the x and the y axes are exactly perpendicular, then the skew is 0.

The Extrinsic Parameters are six, they allow to switch from the world reference system [X Y Z] to the camera reference system [x y z] through a "*Rototranslation*". The Rototranslation is expressed by the following formula:

$$\begin{bmatrix} x & y & z \end{bmatrix} = \begin{bmatrix} X & Y & Z \end{bmatrix} \begin{bmatrix} R \end{bmatrix} + t.$$

Where:
-R is the 3-D rotation matrix;
-t is the translation vector.
The lens distortions are the radial and tangential distortion.

The purpose of the calibration is using the Camera Parameters to turn the water profile, represented in pixel coordinates, into metric coordinates. To do so it's been used "*Single camera calibrator app*", a toolbox provided by MATLAB that allows to estimate the camera parameters. "*Single Camera Calibrator App*" requires you to create a checkerboard pattern. The size of the squares is free. The smaller is the side of the square the more accurate will be the assessment of the parameters. The chosen size for the squares is 5x5 centimeters. Moreover the checkerboard pattern can't be a square, this implies that the number of rows should be even while the number of columns should be odd. This grant the app to define the orientation of the checkerboard, assigning the x-direction to the one which has more squares. After that, the checkerboard pattern is fixed to the three glasses of the facility (see figure 4.10) taking care to set the checkerboard as flat as possible in order to reduce to a minimum the imperfections.

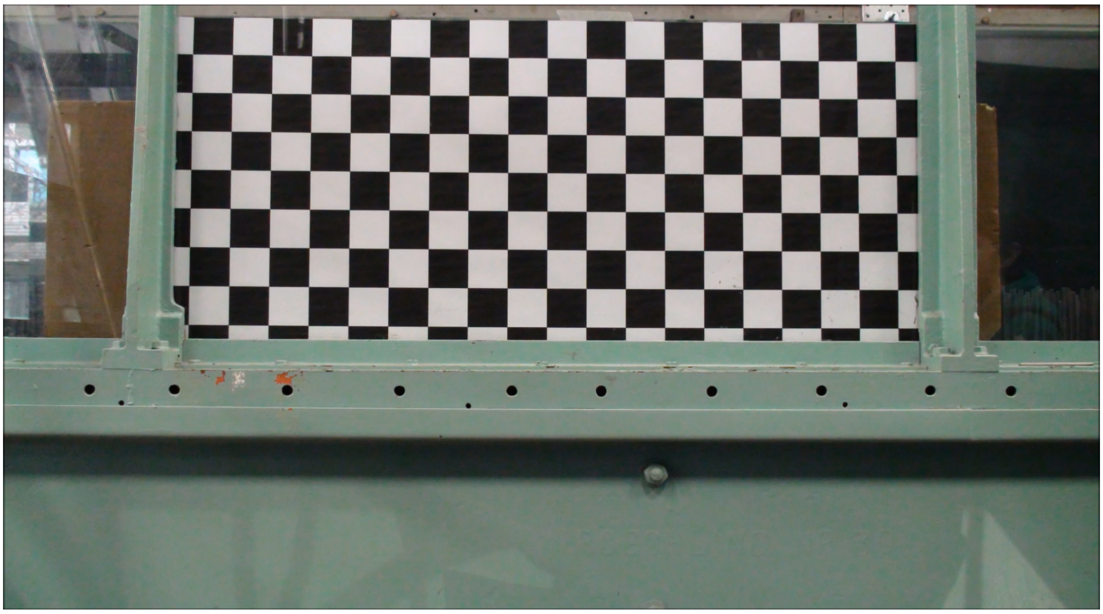

Figure 4.10. *Image of the checkerboard pattern fixed to one of the three glasses of the channel.*

Once the checkerboard is fixed the next step is to take 20 pictures of the checkerboard pattern. The pictures are taken from approximately 1.5 meters, which is the same distance chosen to make the movies. The images are taken with an angles less than 45 degrees between the plane of the checkerboard and the camera. Those images enable the toolbox to calculate the camera parameters with more accuracy. The images are added in the toolbox, which automatically finds the checkerboard pattern in each image and rejects those which don't have a certain level of accuracy. For example are rejected those where the angle between the checkerboard and the camera is more than 45 degrees.

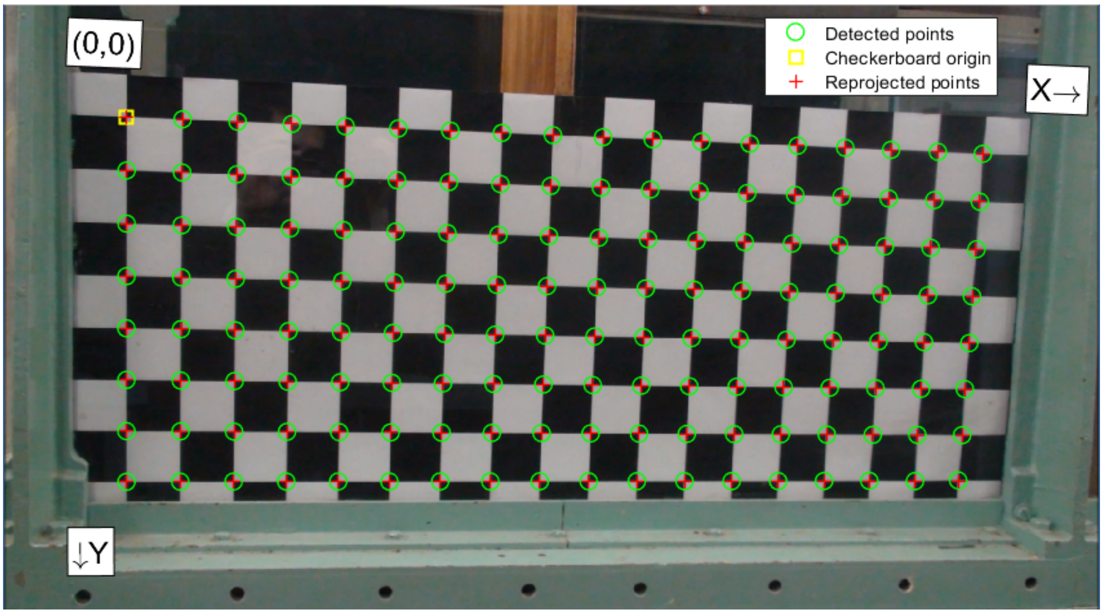

Figure 4.11. *Automathic detection of the checkerboard points.*

The checkerboard origin is set in the upper left corner of the checkerboard. In order to have the x-coordinate decreasing along the direction of the flow and the y-coordinate increasing when the flow grows, in this phase, the center of the reference system is manually changed to the lower left corner. The toolbox computes the parameters by using the function "*Calibrate*" and shows the accuracy of the calibration. It is possible then to improve the accuracy removing the images out of focus.

Figure 4.12. *Mean Reprojection Error per Image.*

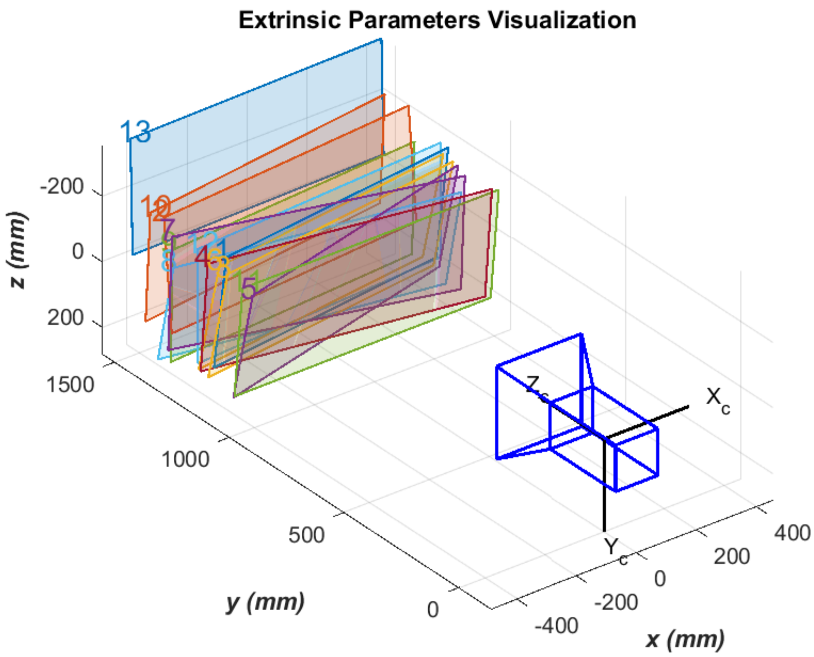

Figure 4.13. *Extrinsics Parameters Visualization.*

The accuracy of this process can be evaluated by making a simple test. At first it is needed to create a matrix which contains the x-coordinate and the y-coordinate of the intersection points of the checkerboard. This points will be called "*World Points*" and they are represented in millimeters. Knowing that the Checkerboard is made by 20 squares along the x-direction and 9 squares along the y-direction it results that there will be 144 "*World Points*" coordinates.

x (mm)	y (mm)
0	0
0	50
0	100
0	150
0	200
0	250
0	300
0	350
50	0
...	...

Table 4.1. *Points of the checkerboard in metric coordinates known as "World Points".*

After that, it is used the MATLAB function called "*Detect Checkerboard Points*". The function analyzes the provided checkerboard image and returns the detected points of the checkerboard intersections in pixel coordinates as well as the total size of the checkerboard. Once the pixel coordinates of the checkerboard are known, it is used the MATLAB function "*PointsToWorld*" which, utilizing the translation vector and the rotation matrix, allows to generate the World coordinates in millimeters of the checkerboard from the pixel coordinates of the same. This set of coordinates is called "*New World Points*".

x (mm)	y (mm)
0.26	0.22
0.17	50.16
0.22	100.26
0.43	150.47
0.28	200.38
0.51	250.51
0.59	300.44
0.65	350.35
50.16	0.07
...	...

Table 4.2. *Reprojected points of the checkerboard in metric coordinates known as "New World Points"*

If the two sets of coordinates are compared it is highlighted that the accuracy reached is about half of a millimeter. The following image is a representation of the "*World Points*" and the "*New World Points*".

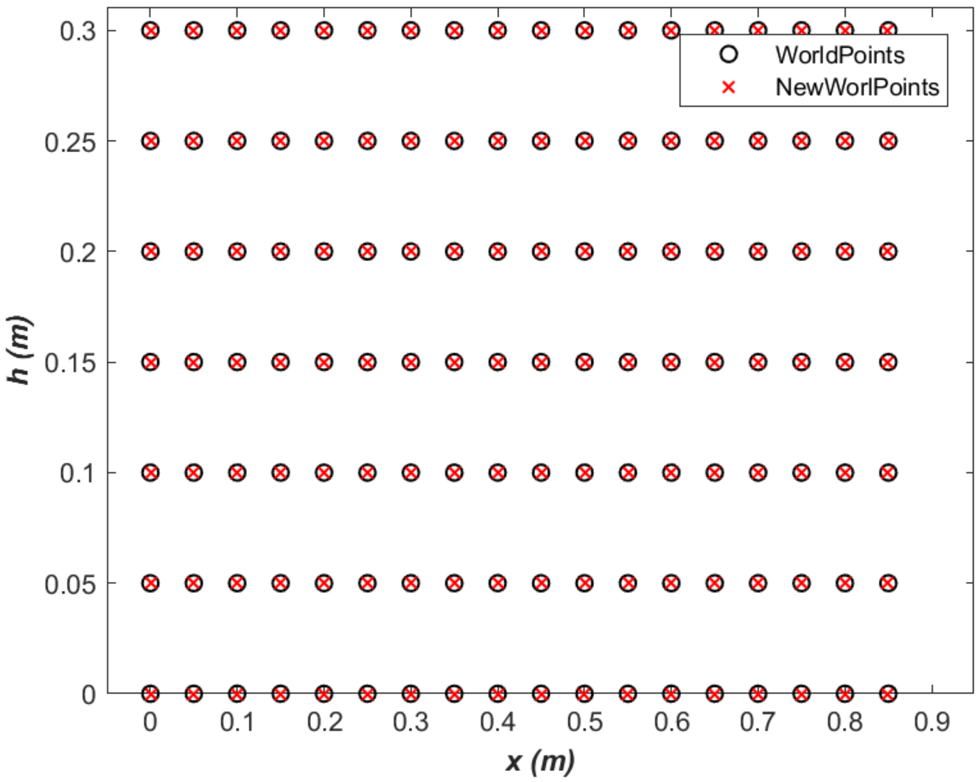

Figure 4.14. *Presentation of the reprojecting precision.*

4.6 Data Processing

In the previous section was discussed the process used to assess the Camera Parameters that are those parameters which allow to switch from a pixel coordinated system to a metric coordinates system. Once those parameters are known it is possible to use the MATLAB function "*PointstoWorld*" that, starting from the pixel coordinates and the camera parameters, allows to calculate the metric coordinates of each profile.
For each run test the water profile is split because the movies coming from the three different cameras are processed separately. In figures 4.15, 4.16 and 4.17 is represented a run test for a 1% slope, $H_o = 0.20m$ and $t = 3.24s$ after the gate opening.

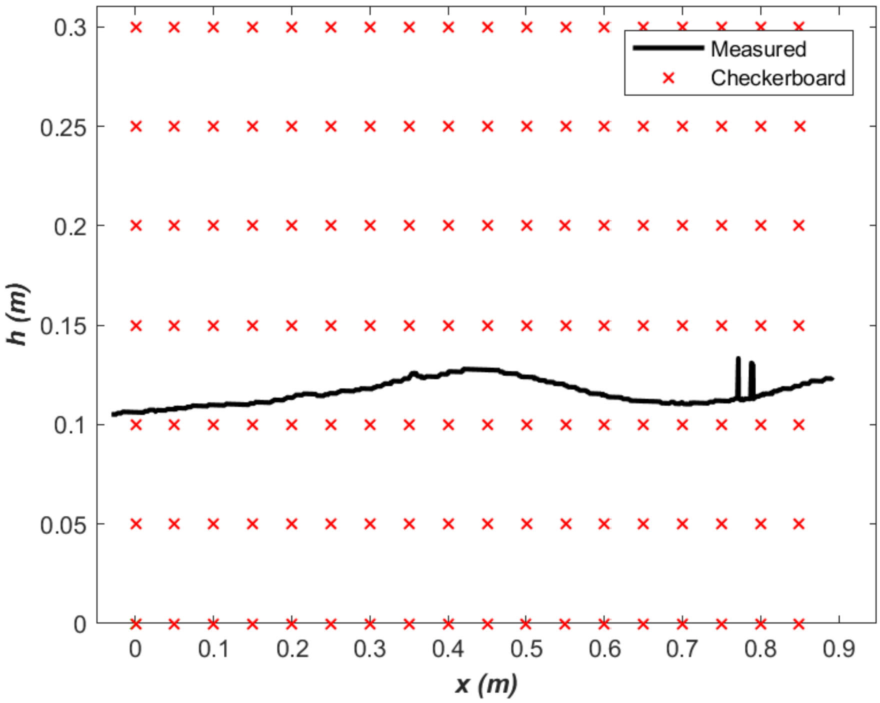

Figure 4.15. *Water surface profile for* $S_o = 1\%$, $H_o = 0.20m$, $t = 3.24s$ *recorded by Camera 1.*

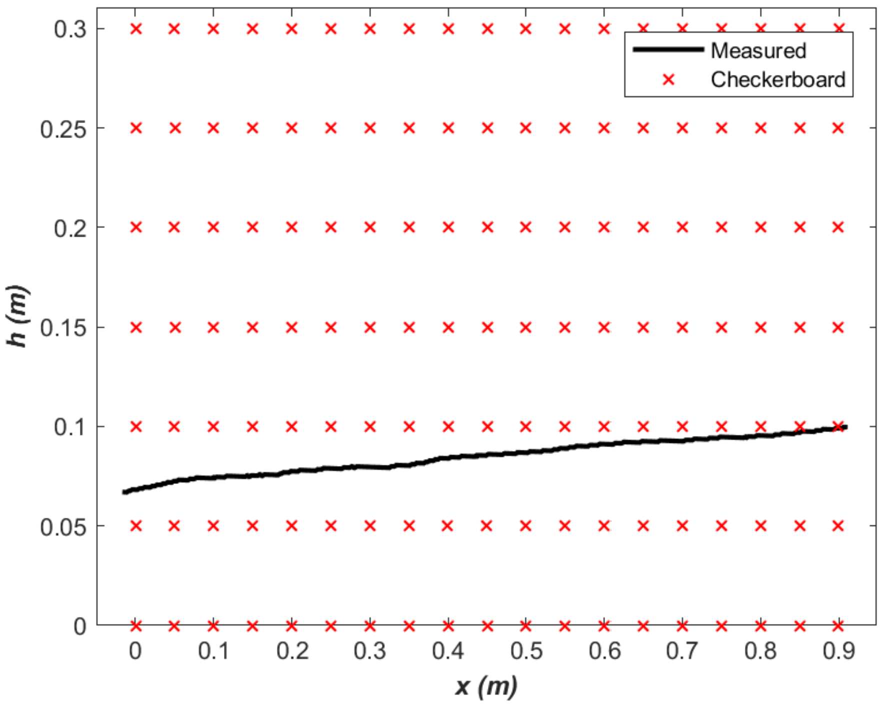

Figure 4.16. *Water surface profile for* $S_o = 1\%$, $H_o = 0.20m$, $t = 3.24s$ *recorded by Camera 2.*

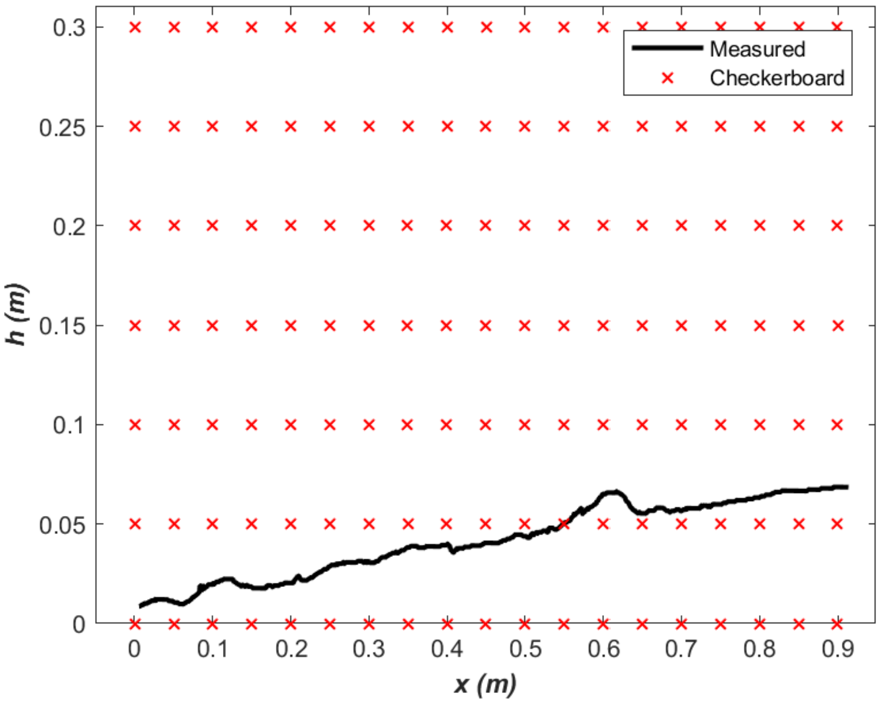

Figure 4.17. *Water surface profile for $S_o = 1\%$, $H_o = 0.20m$, $t = 3.24s$ recorded by Camera 3.*

The center of the reference system is set, in each of the three cameras, in the lower left checkerboard point detected by the camera. This means that for each camera are known the metric coordinates of the water profile, but in a local reference system which can only be associated to the camera used to determine the profile itself.
The goal here is to obtain a unique profile referred to a global reference system whose origin is set in the point where the downstream side of the cofferdam touches the bottom of the channel. The distance of the center of the local reference system from the cofferdam and the bottom of the channel depends on how the checkerboard pattern was attached to the glass in the first place. This distance is know for each camera and with simple mathematics operations the complete profile is arranged.
This process is repeated for each experiment about a precise slope. When the slope changes, the reference system set by the checkerboard changes consequently and this process must be repeated with all the four slopes.
In figure 4.18 is showed the assembled profile for a 1% slope, $H_o = 0.20m$ and $t = 1.17s$ seconds after the gate opening. The profiles are flipped mirror in order to have the center of the global reference system on the lower left part of the graph.

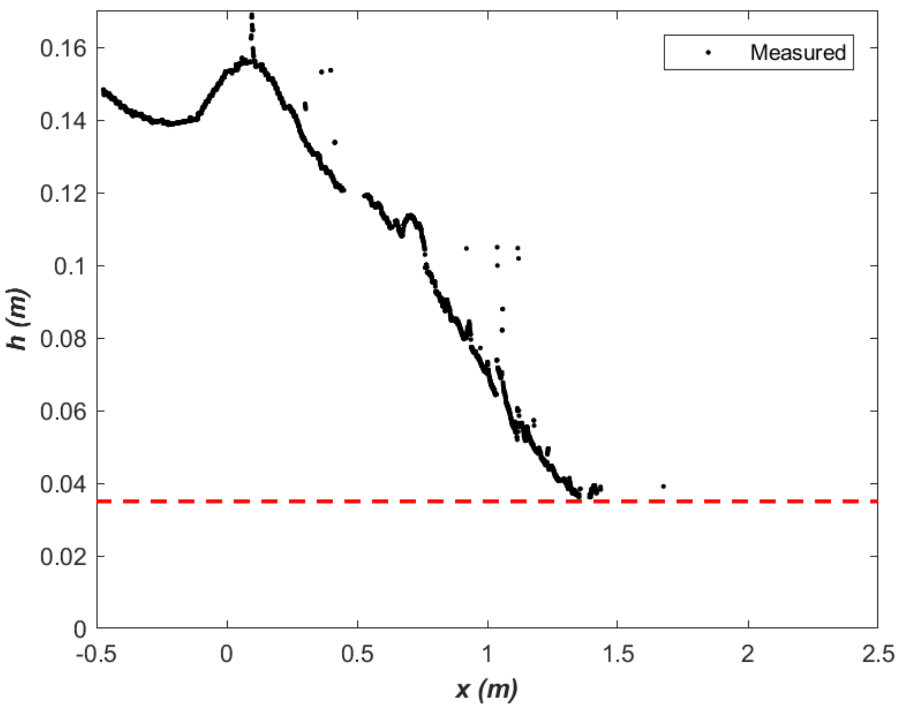

Figure 4.18. *Assembled water surface profile for* $S_o = 1\%$, $H_o = 0.20m$, $t = 3.24s$ *with the presence of several outliers. The horizontal dashed line indicates the water level above which the water level profile* $h(x,t)$ *can not be detected.*

The water level profile manifests a discrete number of outliers mostly due by the splashes of water caused by the instantaneous opening of the cofferdam. To avoid those points to cause interferences in the next phase where the profiles will be interpolated they must be eliminated. In order to eliminate the outliers it is used an interpolating polynomial. In the case of the 1% slope run tests there are 121 frames, each of them with several outliers, mostly in the first 2/3 seconds after the gate opening. The profile is interpolated with a polynomial function whose grade changes based on the number of outliers and their proximity to the real water surface.
The outliers are treated by setting that if the distance between a point of the interpolating polynomial and the point with the same abscissa of the detected water surface is bigger than 3mm, this point must be eliminated. This process allows to remove a large part of outliers as shown in figure 4.20.

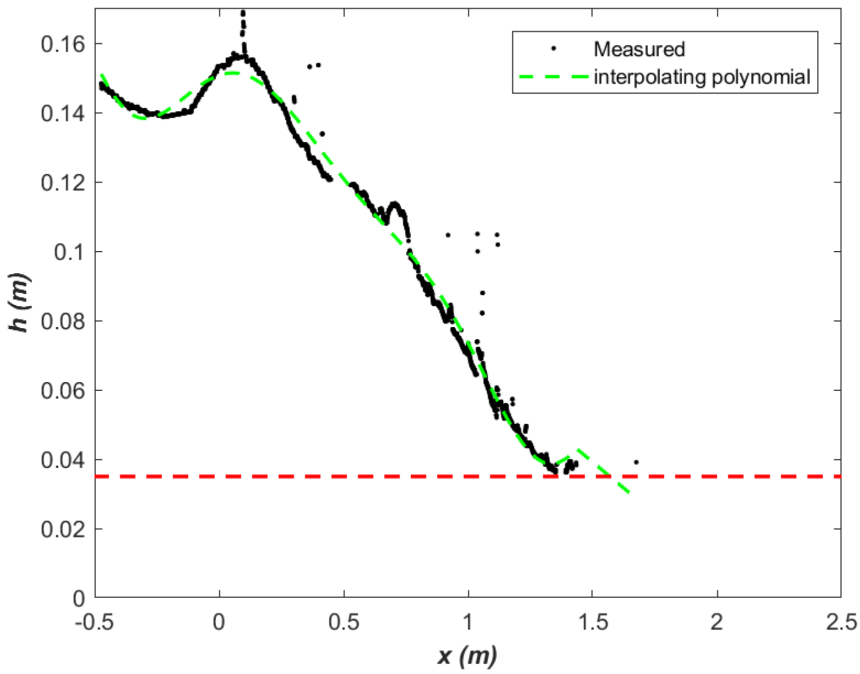

Figure 4.19. *Assembled water surface profile for $S_o = 1\%$, $H_o = 0.20m$, $t = 3.24s$ with the presence of several outliers and interpolating polynomial function.The horizontal dashed line indicates the water level above which the water level profile $h(x, t)$ can not be detected.*

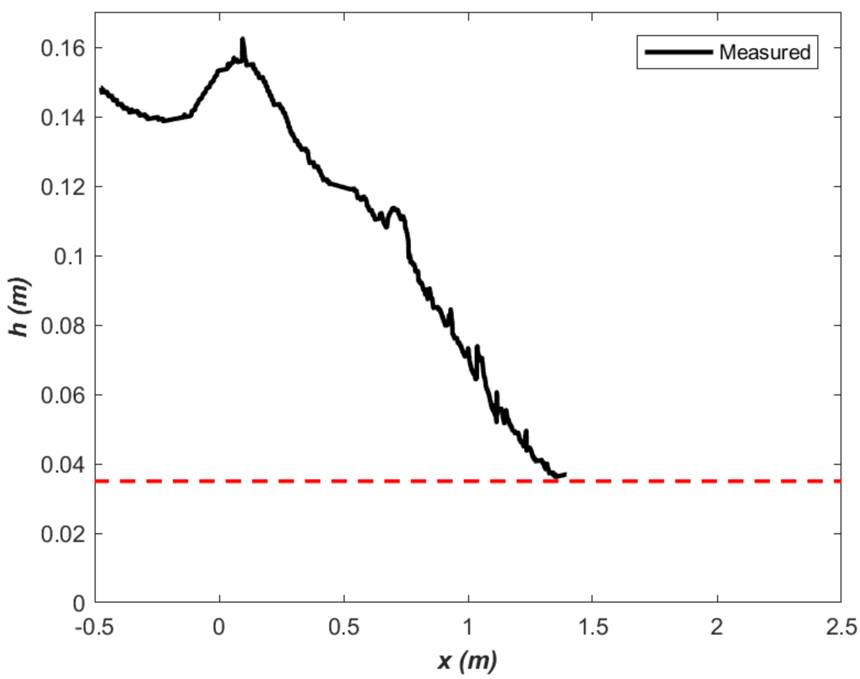

Figure 4.20. *Assembled water surface profile for $S_o = 1\%$, $H_o = 0.20m$, $t = 3.24s$ once all the outliers are removed.The horizontal dashed line indicates the water level above which the water level profile $h(x, t)$ can not be detected.*

The remaining outliers will be treated later.
In order to have statistically robust results the run tests are performed several times. As mentioned before the 0% slope configuration was performed ten times for each H_o thereby allowing the acquisition of statistically robust water level data not affected by outliers. In figure 4.21 are represented all the ten profiles for 4 different times (t=0.5s, t=1.8s, t=3.1s and t=4.3s) for all the four water levels. The outcome of the analysis showed a low standard deviation between different water profiles after 10 replicas. This led to a decision of performing only 5 replicas for the remaining H_o and S_o. Hence, water level data for $S_o = 0\%$ are presented as the averages of 10 water level replicas while the last 12 configurations are presented as the averages of the 5 water level replicas.

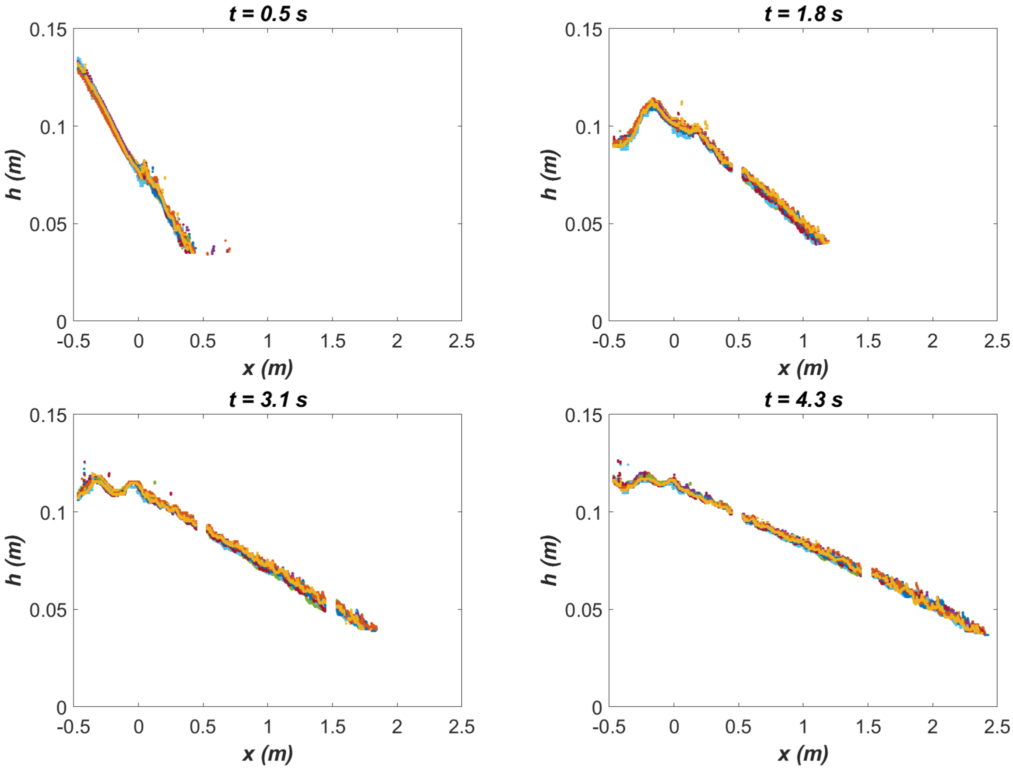

Figure 4.21. *Representation of the water surface profile, derived from the superimposition of ten run tests, for $S_o = 0\%$, $H_o = 0.15m$, at for different times (t=0.5s, t=1.8s, t=3.1s and t=4.3s).*

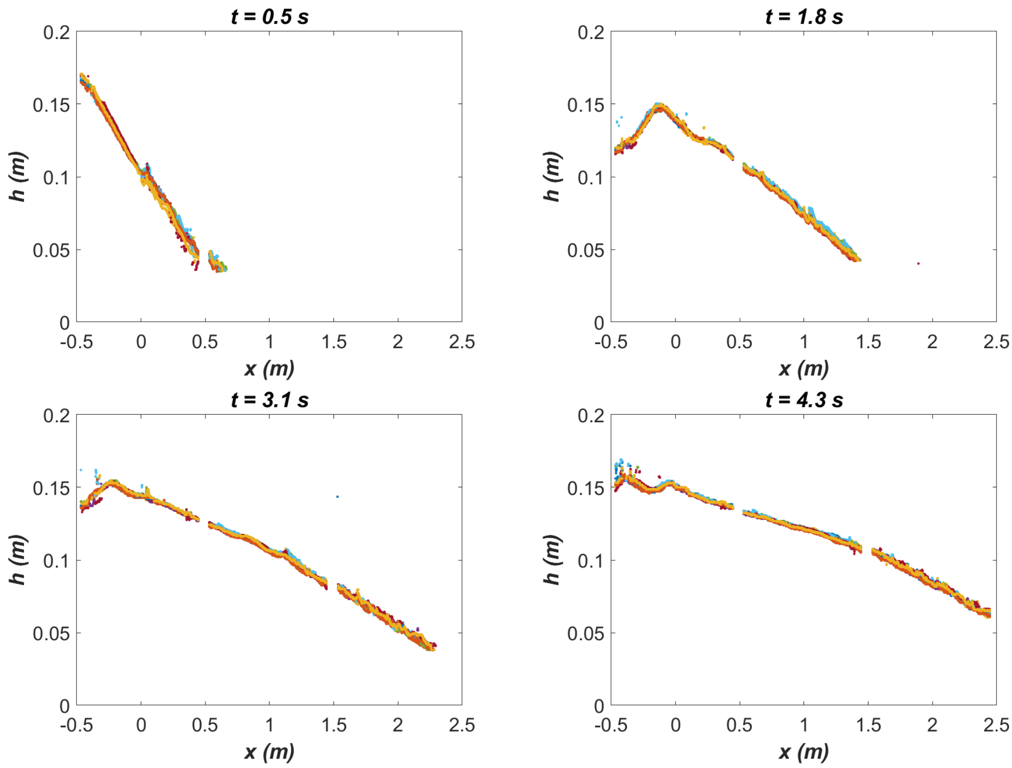

Figure 4.22. *Representation of the water surface profile, derived from the superimposition of ten run tests, for $S_o = 0\%$, $H_o = 0.20m$, at for different times (t=0.5s, t=1.8s, t=3.1s and t=4.3s).*

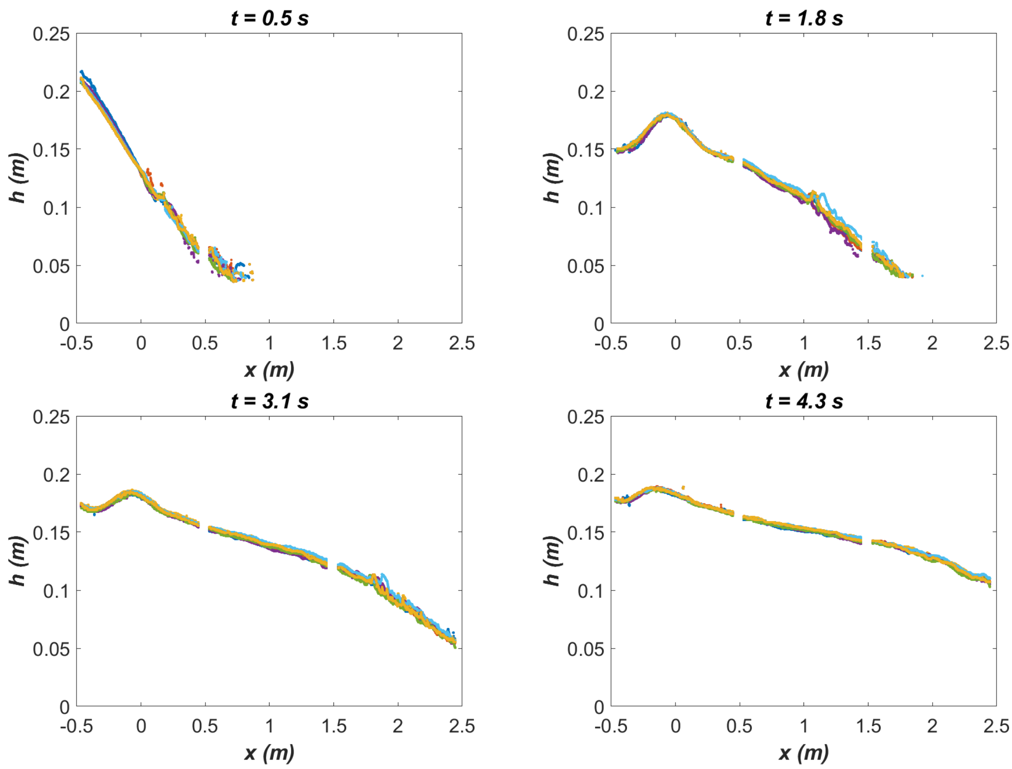

Figure 4.23. *Representation of the water surface profile, derived from the superimposition of ten run tests, for $S_o = 0\%$, $H_o = 0.25m$, at for different times (t=0.5s, t=1.8s, t=3.1s and t=4.3s).*

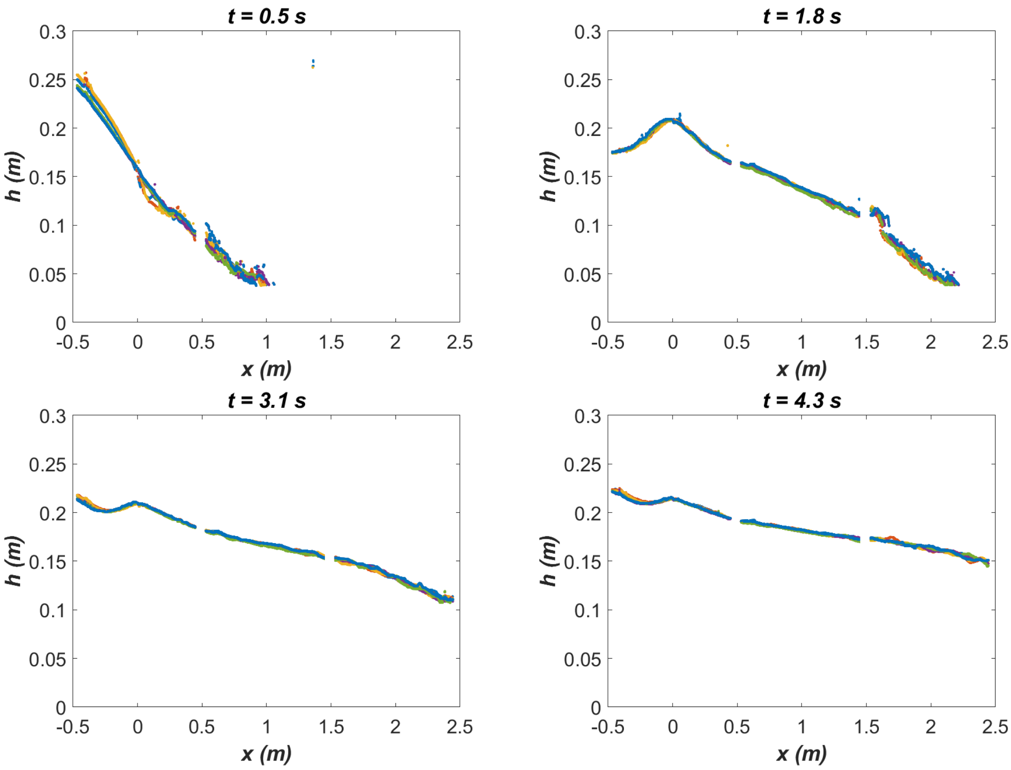

Figure 4.24. *Representation of the water surface profile, derived from the superimposition of ten run tests, for $S_o = 0\%$, $H_o = 0.30m$, at for different times (t=0.5s, t=1.8s, t=3.1s and t=4.3s).*

5. Numerical Solution of the SVE

The numerical scheme used to solve equations 3.1 and 3.2 for $h(x,t)$ and $U(x,t)$ for $x > 0$ and $t > 0$ was described by Keskin and Agiralioglu in 1997 [42]. The mesh setup matches the flume experiments earlier described, where S_o and H_o are varied. In order to solve numerically the SVE Keskin and Agiralioglu proposed the following formula

$$\frac{\partial Q}{\partial t} + \alpha \frac{\partial Q}{\partial x} + \beta = 0, \tag{5.1}$$

where α is

$$\alpha = 2\frac{Q}{A} + \frac{\frac{gA}{B} - \frac{Q^2}{A^2}}{\frac{Q}{A}(\frac{5}{3} - \frac{4R}{3B})}, \tag{5.2}$$

and β is

$$\beta = gA(S_f - S_o). \tag{5.3}$$

This model is based on the assumption that

$$\frac{\partial S_f}{\partial x} = 0, \tag{5.4}$$

which in the case studied here is self consistent. The Continuity Equation is therefore replaced by equation 5.1. The α and β coefficient are related to the Inflow Hydrograph and the cross-section area quantities.

5.1 Boundary Conditions

In order to solve the equation 5.1 two boundaries conditions must be set. The initial conditions are as in the flume experiments: A dry channel with $h(x,0) = U(x,0) = 0$. The two boundary conditions are the velocity $U(0,t)$ and the water level $h(0,t)$ calculated for a cross-section immediately downstream of the dam. More precisely the section considered is located 1mm ahead of the dam. The $h(0,t)$ is directly imaged and supplied from the flume experiments for each S_o and H_o. In Figure 5.1 is represented the evolution of $h(0,t)$ for a 1% slope, $H_o = 0.25m$ run test. It is shown the typical wavy pattern after the dam-break.

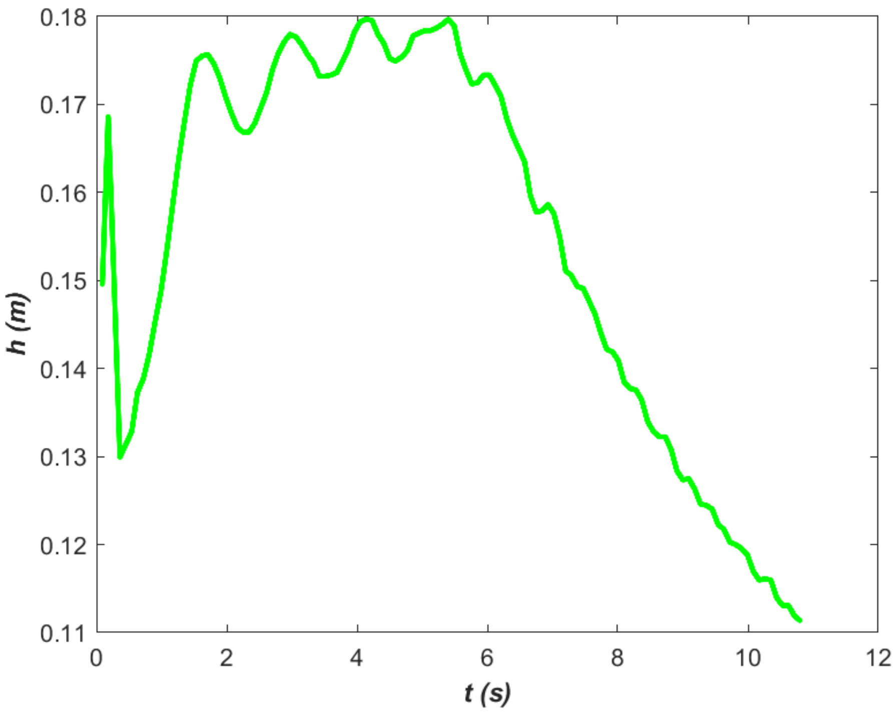

Figure 5.1. *Evolution of $h(0,t)$ for a 1% slope, $0.25m$ run test.*

The $U(0,t)$ was not directly measured but inferred starting from the Inflow Hydrograph. The Inflow Hydrograph can be only partly determined from the imaged inflow volume V_{in} into the dry channel. The inflow volume V_{in} is determined by calculating for each frame, starting from $t = 0s$, the area under the water profile and the multiplying for the width of the channel $(B = 0.5m)$. The first value of the inflow rate is obtained by subtracting from the Volume at $t = 0.09s$ the Volume at $t = 0s$ and dividing by $\Delta t = (t+1) - t$.

$$Q_{in}(0,t) = \frac{V_{in}(t+1) - V_{in}(t)}{\Delta t}. \tag{5.5}$$

The inflow velocity can then be computed from the conservation of mass with the following formula

$$U(0,t) = \frac{Q_{in}(t)}{[Bh(0,t)]}. \tag{5.6}$$

This process is repeated as far as the frontwave tip reaches $x = 2.5m$ which is the maximum length of the profile detected by the cameras. The time needed to get to $x = 2.5m$ depends on the slope and on the initial water level, therefore the length of the first part of the Inflow Hydrograph will be influenced by those two factors.
Although the purpose in this thesis is to interpret the wavefront tip shape, also the recession part of the wave is analyzed. In fact each run for the $S_o = 0\%$ last 7.2 seconds while for the other slopes last 10.8 seconds which is long from the appearence of the wavefront.
In order to evaluate the mean velocity after the wave front is passed it's been used the solution proposed by Ritter et al. [65]. In this case the velocity can be calculated without having to know the Inflow Hydrograph although it is calculated for the sake of completeness. The solution proposed by Ritter implies that there is no water below the dam initially and that the Friction Slope equals the Bed Slope. According to Ritter's solution the velocity and the depth are defined by the following formulas:

$$U = \frac{2}{3}(\frac{x}{t}\sqrt{gH_o}), \tag{5.7}$$

$$\sqrt{gH(t)} = \frac{1}{3}(2\sqrt{gH_o} - \frac{x}{t}). \tag{5.8}$$

Where H_o is the initial water level behind the dam, x is the distance of the cross-section chosen ahead of the dam and t is the time after the cofferdam is instantaneously lifted up. Equation 5.8 can be rearranged as follow:

$$\sqrt{gH(t)} = \frac{1}{3}(2\sqrt{gH_o} - \frac{3}{2}U + \sqrt{gH_o}), \tag{5.9}$$

$$\sqrt{gH(t)} = \sqrt{gH_o} - \frac{1}{2}U, \tag{5.10}$$

therefore $U(t)$ is expressed by

$$U = 2(\sqrt{gH_o} - \sqrt{gH(t)}). \tag{5.11}$$

Once the velocity is known the boundary condition is set and the inflow hydrograph can be calculated too. The following image shows a typical hydrograph for a 1% slope, $0.25m$ run test.

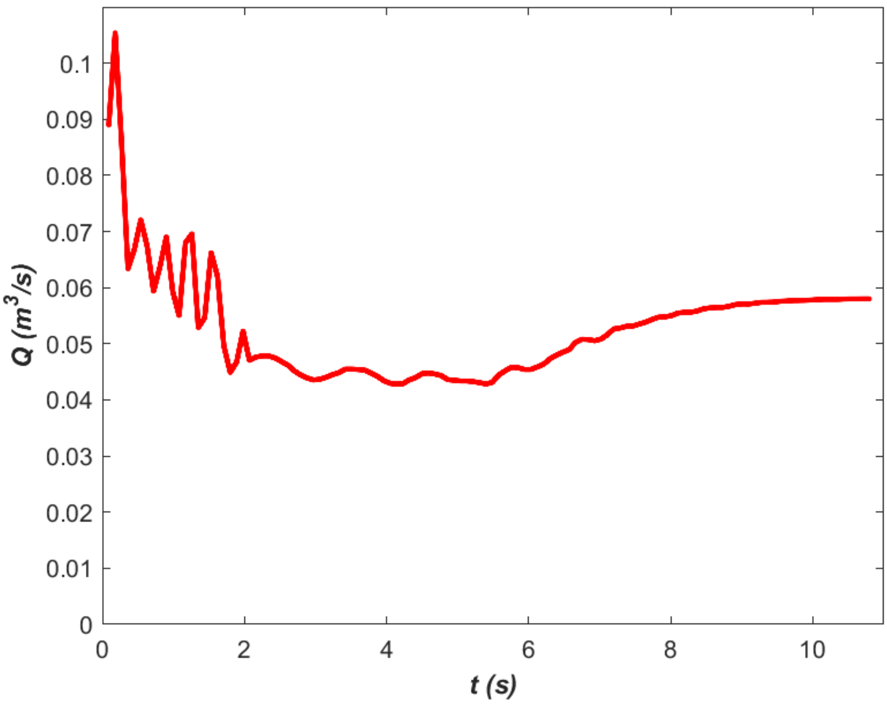

Figure 5.2. *Inflow hydrograph obtained by differenciating the volumes in time for the first 2 seconds, when the frontwave is visible, and with Ritter's formula for the remaining time.*

For the first two seconds the inflow hydrograph is calculated differenciating the volumes, instead after that it is used the Ritter solution. Due to the limited validity range of the solution proposed by Ritter, after 5 second the flow rate shows an increasing trend. As shown in expression 5.11 this is because when $H(t)$ lowers H_o remains the same, consequently the velocity increase and Q_{in} too. The Ritter solution is valid as long as the water level follows a waviness pattern. Therefore the recession part of the hydrograph is modeled in a even more different way. When the water level $H(t)$ and the time t are plotted in a logarithmic scale stands out an important characteristic of the hydrograph.

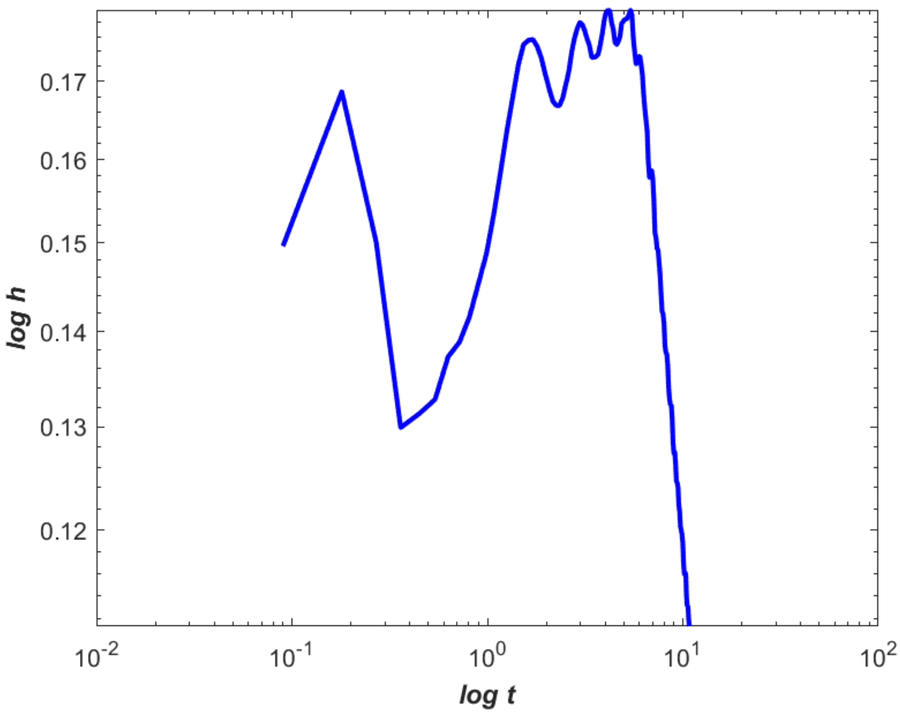

Figure 5.3. *Logarithmic representation of the measured water level in time, the linear part suggests a power low of h in the recession part.*

The logarithmic water level drops following a straight line resulting that the real water level follows a power low. The time when the dropping starts depends on the slope S_o and on the initial water level H_o of the experiments. Presuming that the inflow drops following the same trend of the water level it can be expressed with the following formula

$$Q = At^{-\beta}, \tag{5.12}$$

where the parameters A and β emerges from the boundary condition. Q_o represents the inflow at time $t*$ which is time when the Ritter Solution fails. V is the Volume loss between the time $t*$ and t' which is the end of the simulation. It can be calculated by the movie imaging. Solving the following system A and β are inferred

$$Q = At^{-\beta}, \tag{5.13}$$

$$V = \int_{t*}^{t'} At^{-\beta} dt. \tag{5.14}$$

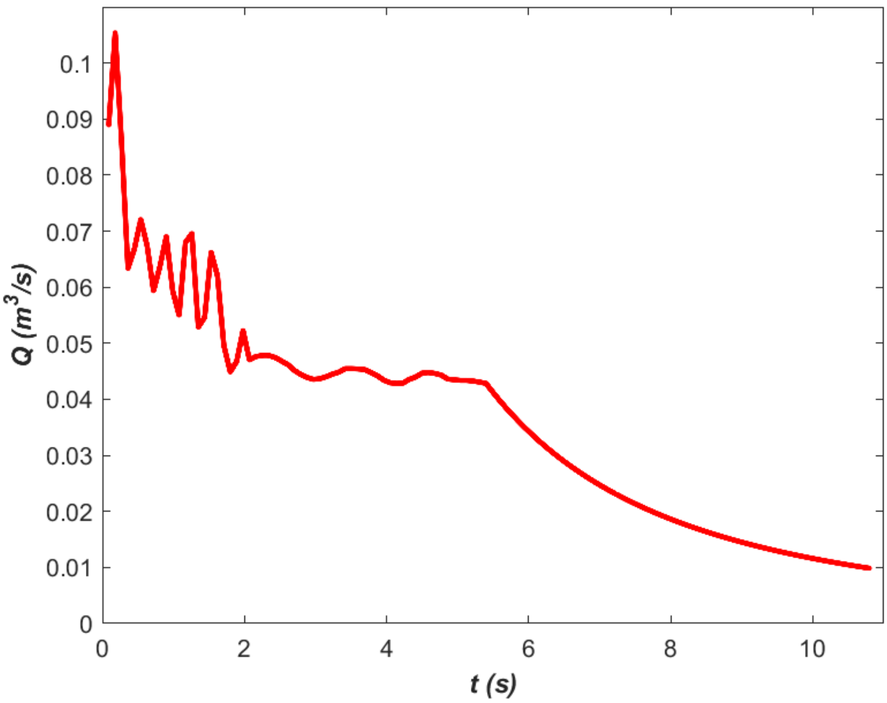

Figure 5.4. *Inflow hydrograph obtained by differenciating the volumes first, with Ritter's formula when the frontwave is no more recorded by the cameras and with a power low with negative exponent for the remaining time.*

With these initial and boundary conditions, the numerical scheme was used to assess how various parametrization of S_f described by equations 3.7 and 3.15 impact $h(x,t)$. For equation 3.7, Manning's $n = 0.05$, which was deemed optimal for reproducing the steady-state wave velocity (discussed later). This value is also commensurate with many other experiments on flow through emergent dense vegetation described elsewhere [58, 10]. For equation 3.15, the calculations are conducted using $C_{d,iso}$, $C_{d,a}$, and $C_{d,s}$ as well as a constant C_d. All these calculations are then compared to experiments imaging $h(x,t)$ for the varying H_o and S_o.

6. Results

6.1 Data summary and comparison with the Ritter Solution

The measured $h(x,t)$ for all 16 configurations are presented in dimensionless form and compared to the Ritter Solution (i.e. equation 3.10) in Figure 6.1. The Ritter Solution (based on $S_f = S_o = 0$) shows that the dimensionless water level h_n and the dimensionless wave speed u_n are linked by a parabolic relation. Follows that for a fixed h_n corresponds a unique u_n. The comparison between measurements for all x and t per test run and the Ritter model highlights three results:
(i) The dimensionless variables selected to normalize the Ritter Solution do not fully collapse the measurements. This result emphasizes the impact of the dense rods canopy on the flow making the initial condition of ideal flow no longer valid.
(ii) The measured $h_n = h/H_o$ is larger than predictions from the Ritter Solution and the deviations are dependent on the specific S_o and H_o value. This is connected to the presence of the rods (not covered by Ritter) which, contributing to the increasing friction, makes the level of the water deeper if compared with the Ritter Solution. In particular all the 16 configurations show, in the first frames of the test runs, a value of the normalized water level h_n of about 0.75, which is a 50% more than the 0.5 of the Ritter Solution.
(iii) The initial decay of h_n with increasing u_n is much steeper than predictions by equation 3.10 for all S_o and H_o highlighting the overall role of S_f.
The first result achieved in this thesis is the confirmation of non-applicability of the Ritter Solution in the case studied. This result, already achieved in the past, led to a further inquiry into the explicit inclusion of distributed drag forces by vegetation elements. The results of this inquiry already mentioned will be presented in the next sections.

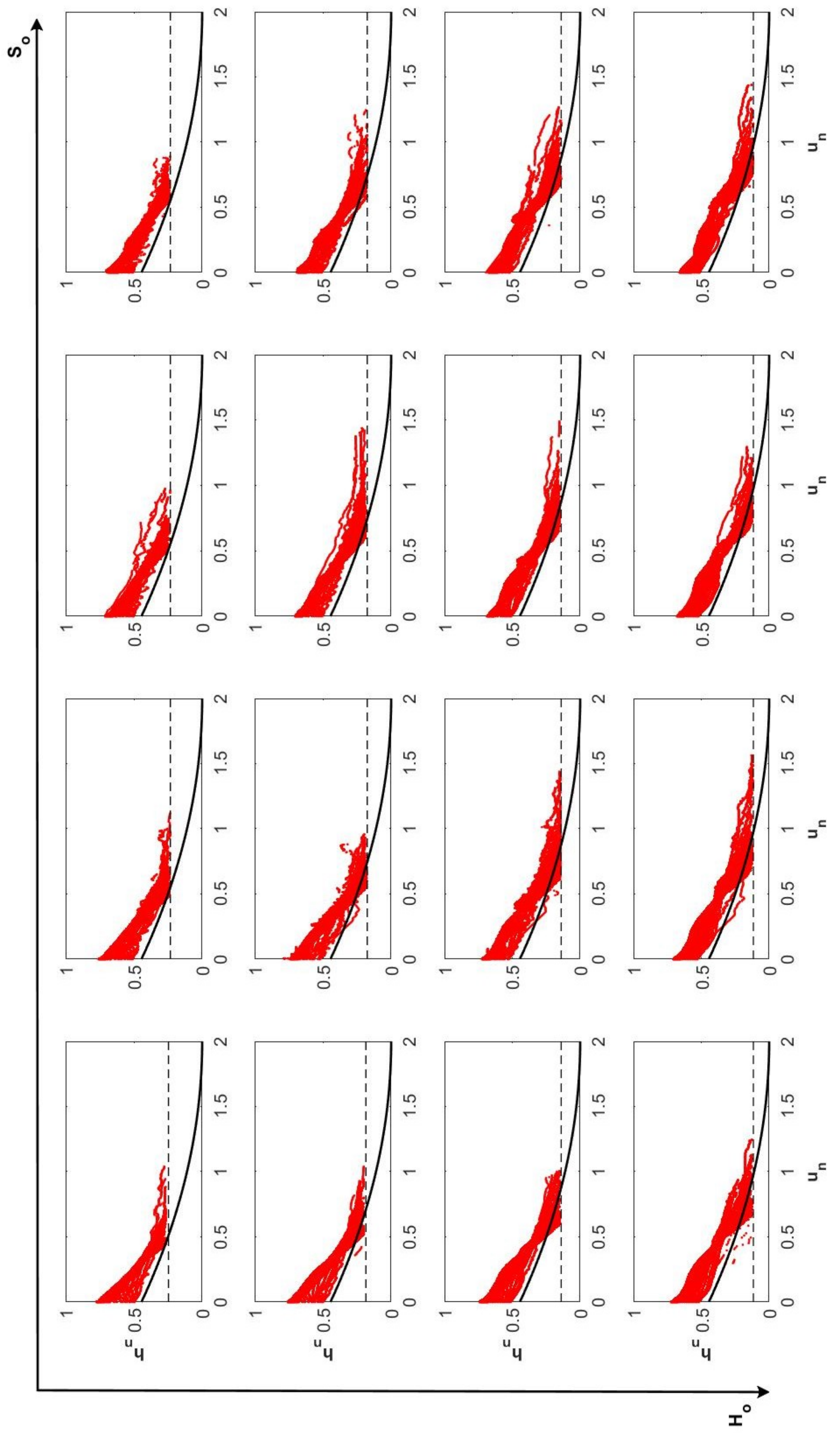

Figure 6.1. *A comparison between measured normalized water surface $h_n = h/H_o$ (red circles) and modeled h_n (black line) using the Ritter Solution for $S_o = 0$ against normalized velocity $u_n = (x/t)/\sqrt{gH_o}$ for all 16 configurations (and $x > 0, t > 0$). Panels from left to right indicate increasing $S_o = 0$,1,2,3% (horizontal arrow) whereas panels from top to bottom indicate increasing $H_o = 0.15, 0.20, 0.25, 0.30m$ (vertical arrow).The horizontal dashed line in all panels indicates the water level beneath which it is impossible to detect the surface.*

6.2 Determination of C_d and n

To investigate the mechanism of the wave propagation through a rod dense canopy after the dam-break two paths can be followed.
The first approach is based on Manning's theory which, although is considered too simple even to describe an uniform steady flow, can be useful to understand how far an inertial unsteady flow can be represented by a constant n value. Therefore, the first goal of this section is to find a parametrization of a constant Manning's value n able, at least, to reproduce the velocity of the wavefront. A preliminary estimate n was carried out using a small subset of the water level measurements.
Within the wavefront region, the front speed is assumed to be roughly constant so that $\partial U/\partial t$ and $\partial U/\partial x$ are small relative to the remaining terms in the SVE [14]. The reduced SVE equation can be written as follow:

$$g\left(\frac{\partial h}{\partial x} + S_f\right) = 0, \tag{6.1}$$

and the continuity equation simplifies to

$$\frac{\partial h}{\partial t} + U\frac{\partial h}{\partial x} = 0. \tag{6.2}$$

If S_f is inferred with a constant n value equations 3.27 and 3.28 can be deducted. For a constant n, h scales as a power-law with a sub-unity exponent (i.e. $x^{3/7}$). and n is expressed by the following formula

$$n = \sqrt{\frac{h^{4/3}}{U_f^2}\frac{\partial h}{\partial x}}. \tag{6.3}$$

Equation 6.3 was used to compute n thereby ensuring that at least U_f is matched on average near the wavefront. In fact expression 3.28 showed that h scales as a power-law with x. Follows that the wavefront tip measured can only be described in term of velocity. This finding is also illustrated in Figure 6.2, where the wave speed matching is possible only in term of velocity but not in term of wavefront tip shape. A more expansive analysis was conducted on other test runs and an $n = 0.05$ appeared to reasonably reproduce the front speed in all of them.

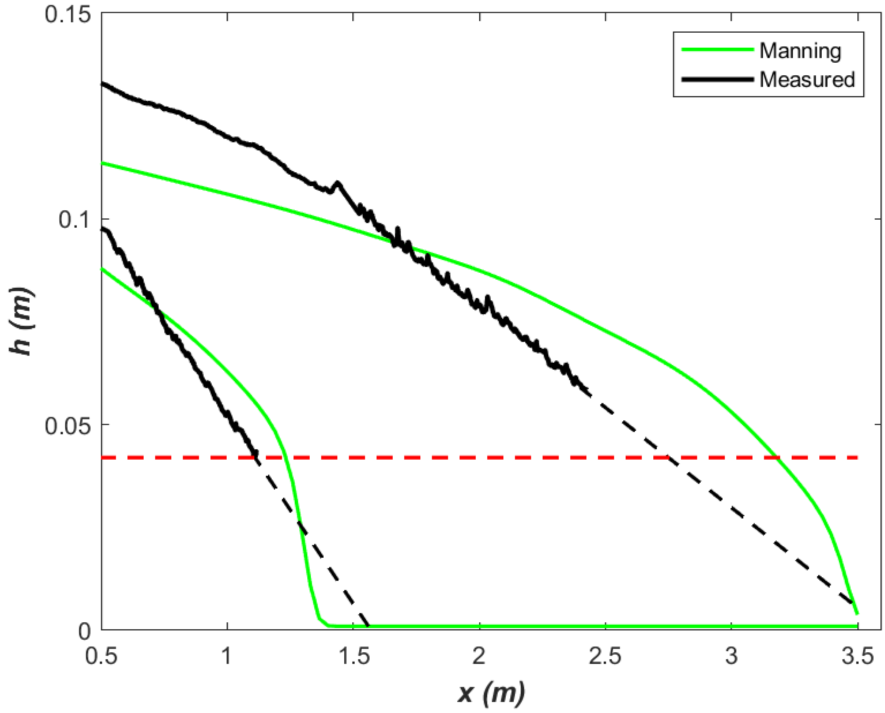

Figure 6.2. *A comparison between measured water surface h and modeled h using a constant $n = 0.05$. Using the linear portion of the $h(x,t)$, a near constant $C_d = 0.4$ was determined and used throughout. The horizontal dashed line in all panels indicates the water level beneath which it is impossible to detect the surface.*

On the other hand the experiments shown a clearly different shape if compared with the shape obtained with a constant Manning's value. Hence the necessity of further inquiry into the explicit inclusion of a distributed drag force by vegetation at high Reynolds numbers. The characteristic linearity of the wavefront tip drops every relation of C_d with the Reynolds number, which means that such shape can be justified only by a constant C_d value. If the same analysis is conducted for a constant C_d, equations 3.25 and 3.26 are obtained, showing that $h(x,t)$ is linear in x and C_d can be obtained as follow

$$C_d = \left(\frac{\partial h}{\partial x}\right)\frac{2g(1-\phi_v)}{U_f^2 mD}, \tag{6.4}$$

where $\partial h/\partial x$ and U_f are respectively the slope and the mean constant velocity of the wavefront tip. U_f is inferred by knowing the position of the wavefront at two different times and then dividing by the time difference between the two frames considered. To do so two frames with a time distance of one second have been chosen, both of them when the wavefront is formed and assumed a linear shape. Although the water profile is not completely visible the movies suggested a linear shape even in the hidden part. $\partial h/\partial x$ is deducted by calculating the slope of the profile at two different times and averaging them afterward. This analysis, performed for different slopes and water levels, converged to a unique C_d values around 0.4. This values along with with the Drag Coefficient depending by the Reynolds number will be used as input to solve the numerical SVE.

6.3 Comparison between SVE and measurements

A comparison across all runs for constant $n = 0.05$ and models of $C_{d,iso}$, $C_{d,a}$, and $C_{d,s}$ as well as $C_d = 0.4$ is now conducted for all $h(x,t)$.
The numerical solving of the SVE emphasized similar results in term of $h(x,t)$ for the runs with $C_{d,iso}$, $C_{d,a}$, and $C_{d,s}$. Therefore, from now on, will be shown only the runs with the drag coefficient obtained for the Staggered configuration which is the most similar to the lay used in the test runs in laboratory.
To best show the results achieved in this thesis two graphics representations have been chosen: (i) a Color Map and (ii) and the water surface profile.
The Color Map is a chart able to exhibit three variables in the Cartesian Plane. The x-axis is the distance from the dam expressed in meters and the y-axis is the time expressed in seconds. The water level is represented by the different colors plotted on the map whose intensity is connected to the water height which may be read in the color bar next to the graph. In this way is possible to show the results for a test run from the moment when the dam collapses to a time fixed to 7.2 seconds. The dashed red lines represent the three times chose to show the water level surface.
The second representation is a figure of the water level surface profile. Each figure contains three graphs regarding three significant times ($t = 0.5s$, $t = 1.5s$ and $t = 2.5s$). In each graphs are plotted the water profiles obtained for $C_{d,s}$, $C_d = 0.4$, $n = 0.05$ and the measured one, one on top of each other. In the interest of giving a visual representation able to show the pattern discovered only 4 out of 16 configuration will be set out. This runs are $H_o = 0{,}15m$ with a slope $S_o = 0\%$, $H_o = 0{,}20m$ with a slope $S_o = 1\%$, $H_o = 0{,}25m$ with a slope $S_o = 2\%$ and $H_o = 0{,}30m$ with a slope $S_o = 3\%$. In this way every slope and every water level are shown comprising the extreme cases.

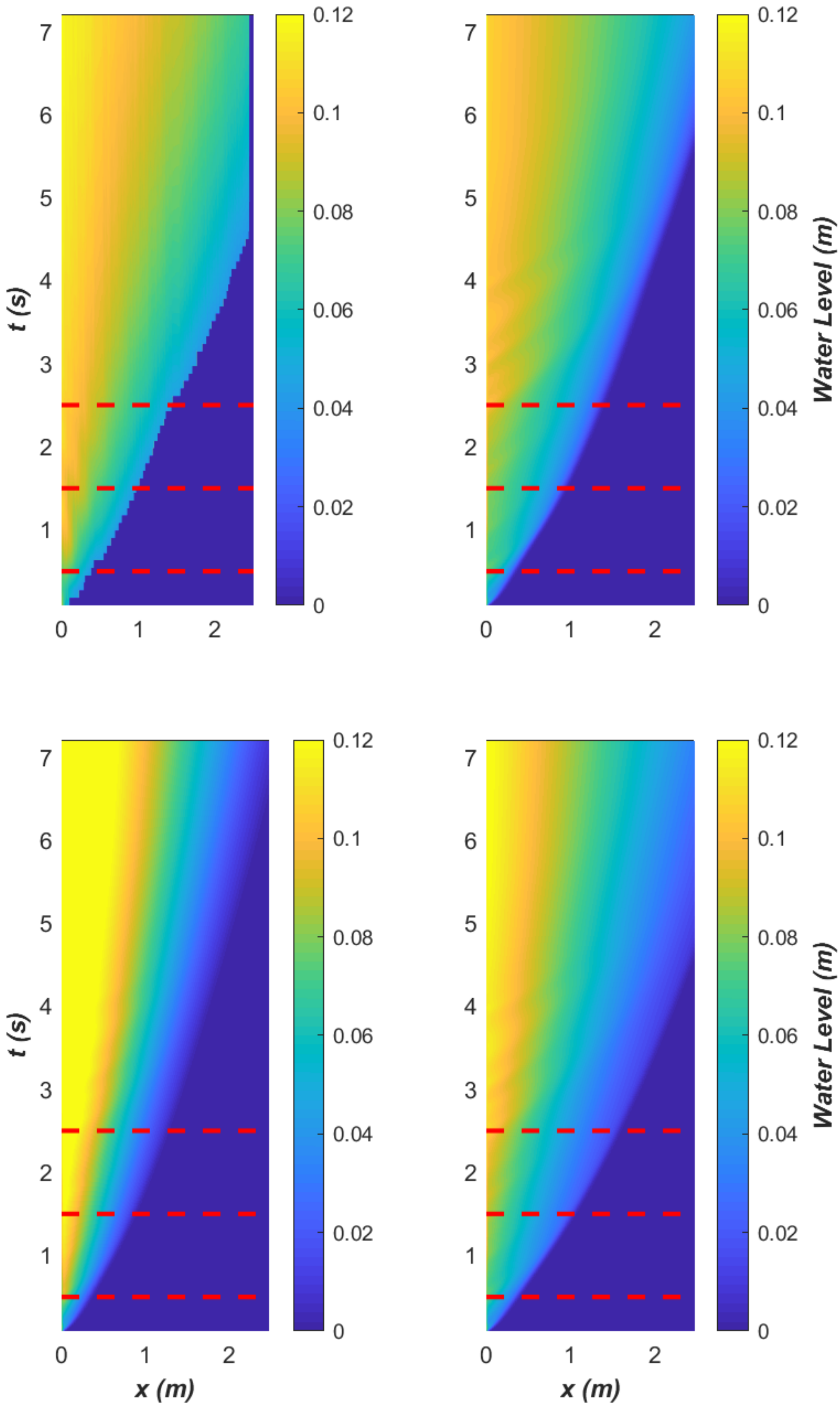

Figure 6.3. *A comparison between measured and modeled $h(x,t)$ for $S_o = 0\%$ and $H_o = 0.15m$. The first panel in the first row from the left represents the measured $h(x,t)$, the second is modeled $h(x,t)$ with $n = 0{,}05$. In the second row from the left is shown the modeled $h(x,t)$ with $C_{d,s}$ and modeled $h(x,t)$ with $C_d = 0.4$.*

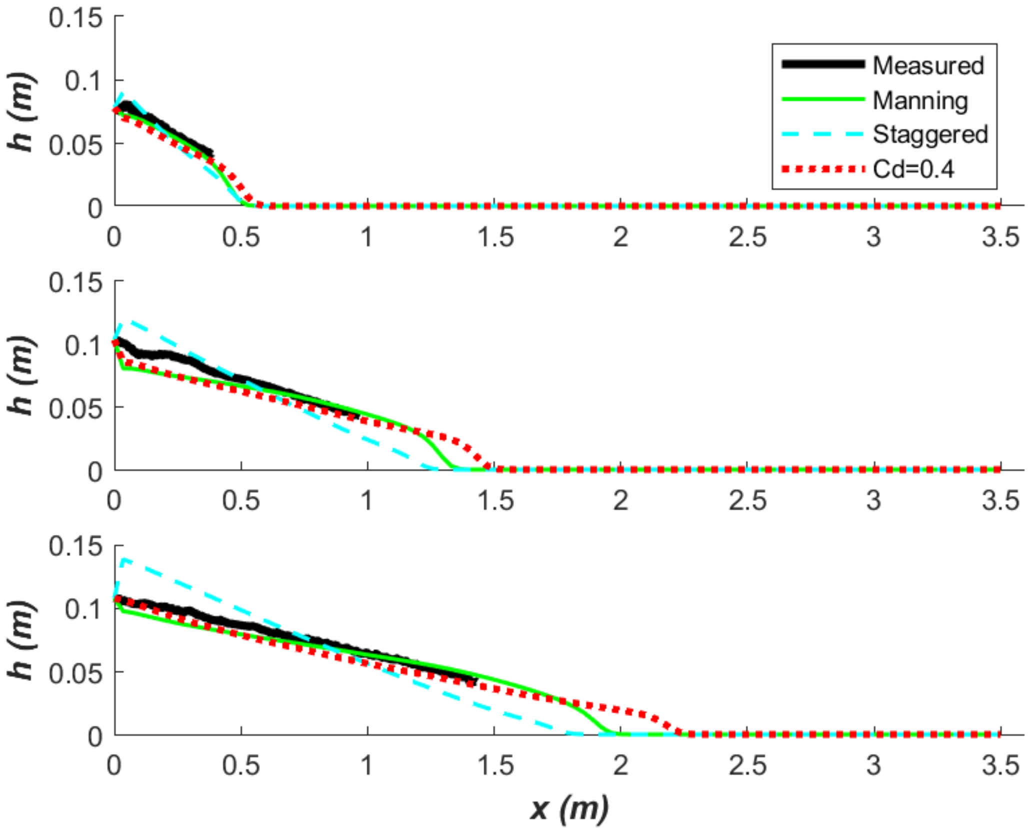

Figure 6.4. *A comparison between measured and modeled $h(x,t)$ for $S_o = 0\%$ and $H_o = 0.15m$. $h(x,t)$ measured is represented with the three $h(x,t)$ modeled ($C_{d,s}$, $C_d = 0.4$ and $n = 0.05$) for three significant times ($t = 0.5s$, $t = 1.5s$ and $t = 2.5s$). The three time instants are shown in figure 6.3 as a horizontal dashed red line.*

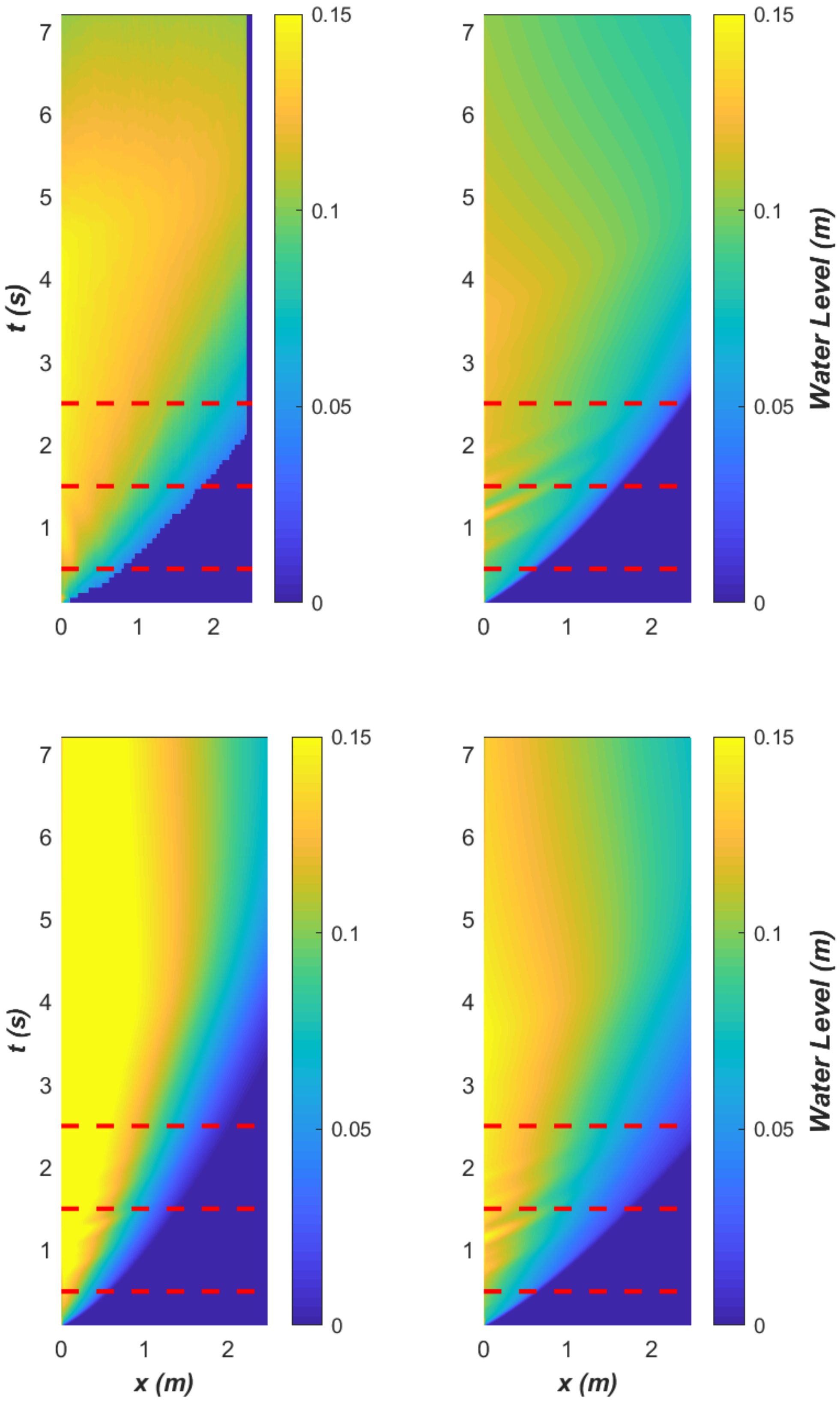

Figure 6.5. *A comparison between measured and modeled $h(x,t)$ for $S_o = 1\%$ and $H_o = 0.20m$. The first panel in the first row from the left represents the measured $h(x,t)$, the second is modeled $h(x,t)$ with $n = 0{,}05$. In the second row from the left is shown the modeled $h(x,t)$ with $C_{d,s}$ and modeled $h(x,t)$ with $C_d = 0.4$.*

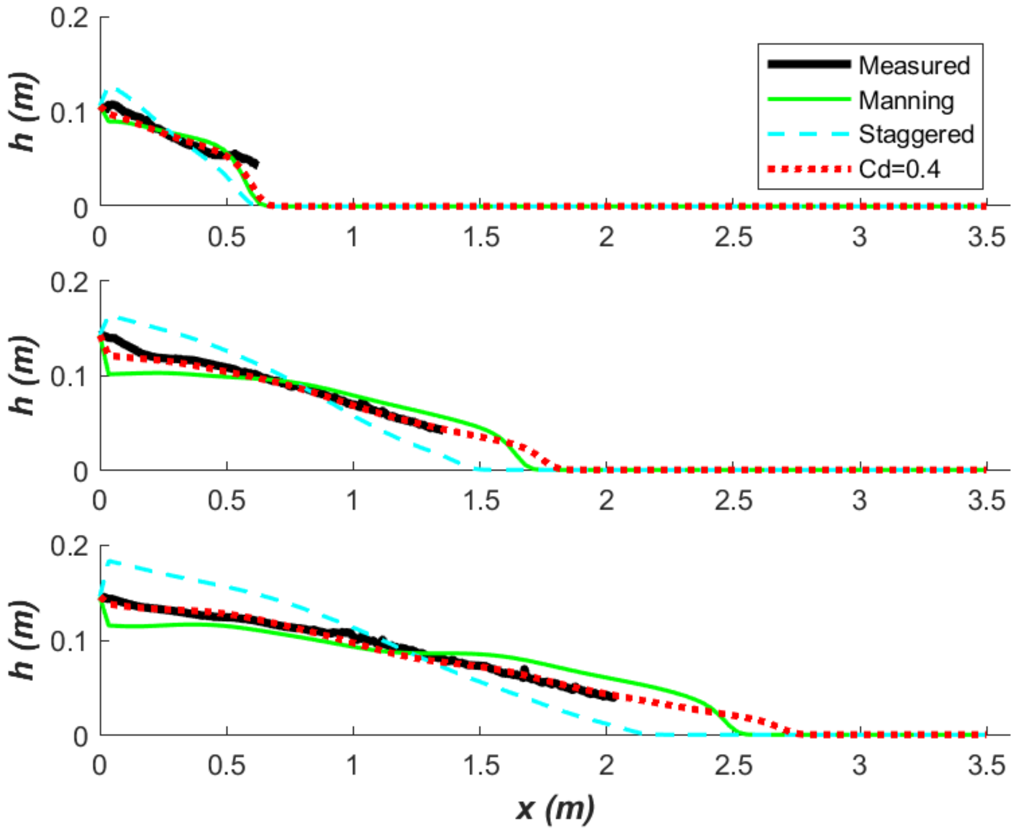

Figure 6.6. *A comparison between measured and modeled $h(x,t)$ for $S_o = 1\%$ and $H_o = 0.20m$. $h(x,t)$ measured is represented with the three $h(x,t)$ modeled ($C_{d,s}$, $C_d = 0.4$ and $n = 0.05$) for three significant times ($t = 0.5s$, $t = 1.5s$ and $t = 2.5s$). The three time instants are shown in figure 6.9 as a horizontal dashed red line.*

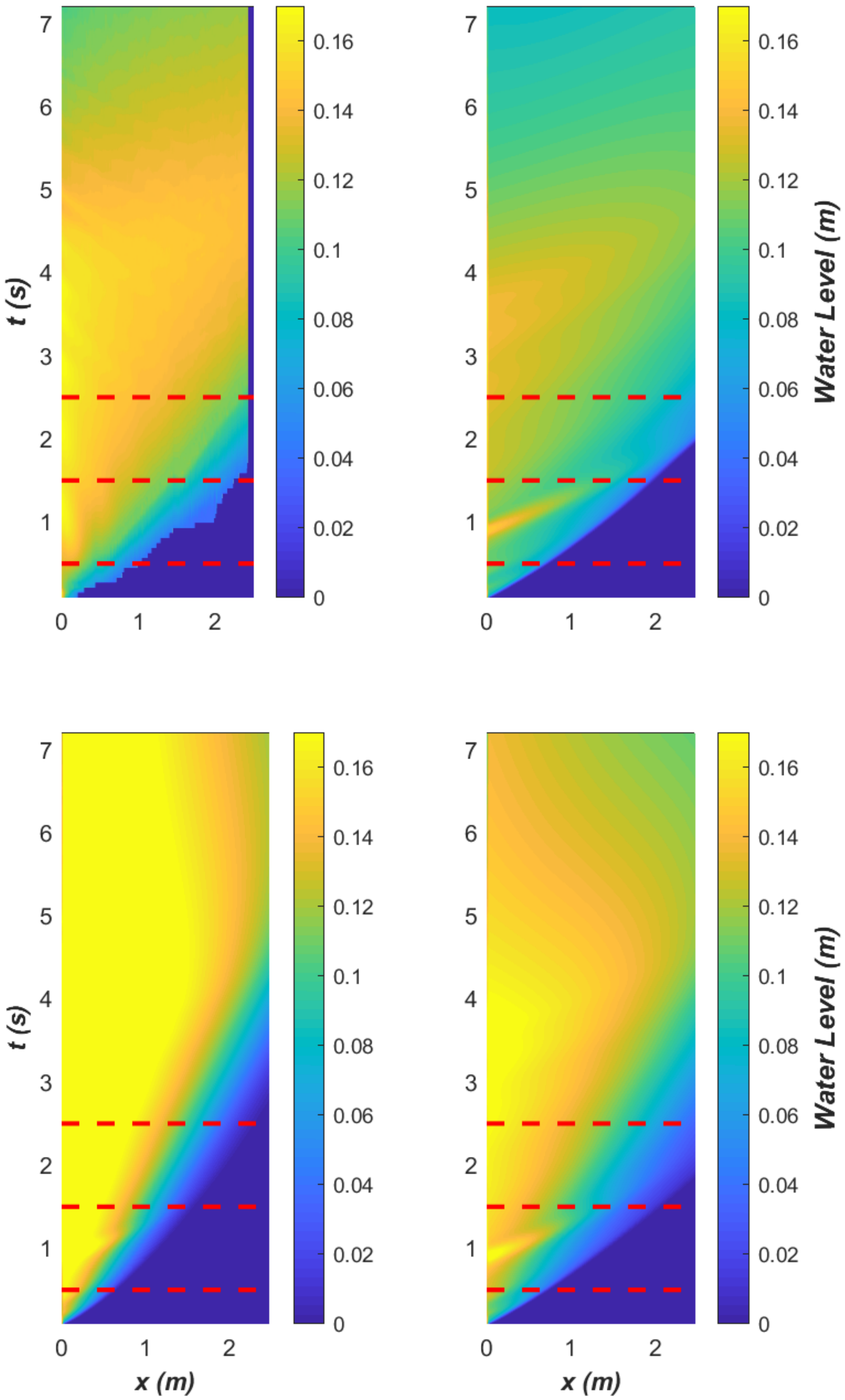

Figure 6.7. *A comparison between measured and modeled $h(x, t)$ for $S_o = 2\%$ and $H_o = 0.25m$. The first panel in the first row from the left represents the measured $h(x, t)$, the second is modeled $h(x, t)$ with $n = 0{,}05$. In the second row from the left is shown the modeled $h(x, t)$ with $C_{d,s}$ and modeled $h(x, t)$ with $C_d = 0.4$.*

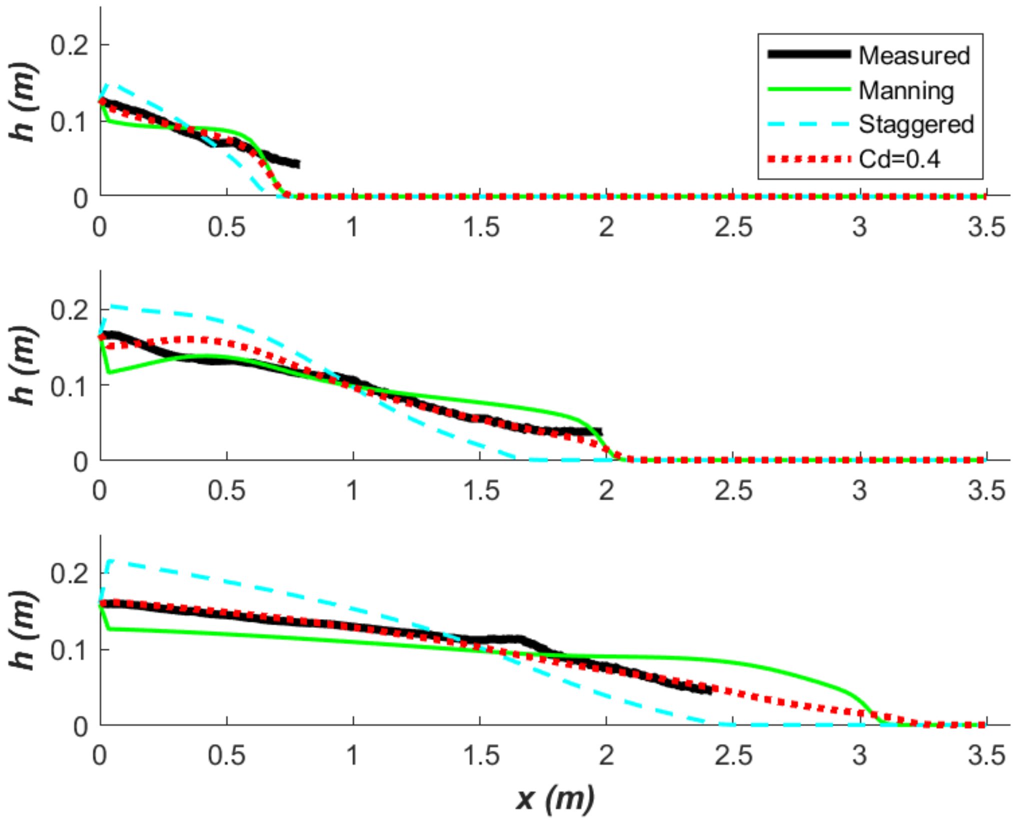

Figure 6.8. *A comparison between measured and modeled $h(x,t)$ for $S_o = 2\%$ and $H_o = 0.25m$. $h(x,t)$ measured is represented with the three $h(x,t)$ modeled ($C_{d,s}$, $C_d = 0.4$ and $n = 0.05$) for three significant times ($t = 0.5s$, $t = 1.5s$ and $t = 2.5s$). The three time instants are shown in figure 6.7 as a horizontal dashed red line.*

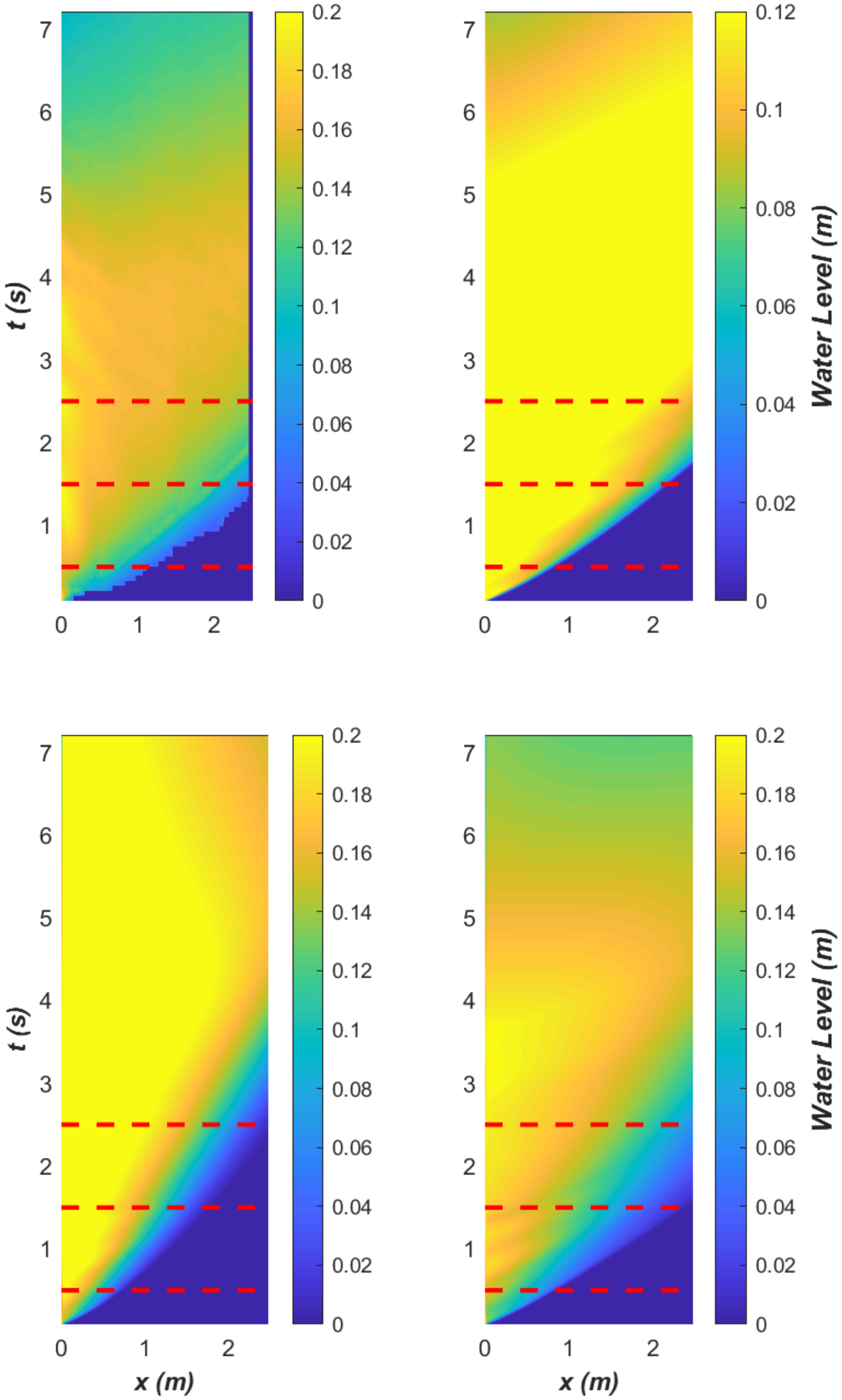

Figure 6.9. *A comparison between measured and modeled $h(x,t)$ for $S_o = 3\%$ and $H_o = 0.30m$. The first panel in the first row from the left represents the measured $h(x,t)$, the second is modeled $h(x,t)$ with $n = 0{,}05$. In the second row from the left is shown the modeled $h(x,t)$ with $C_{d,s}$ and modeled $h(x,t)$ with $C_d = 0.4$.*

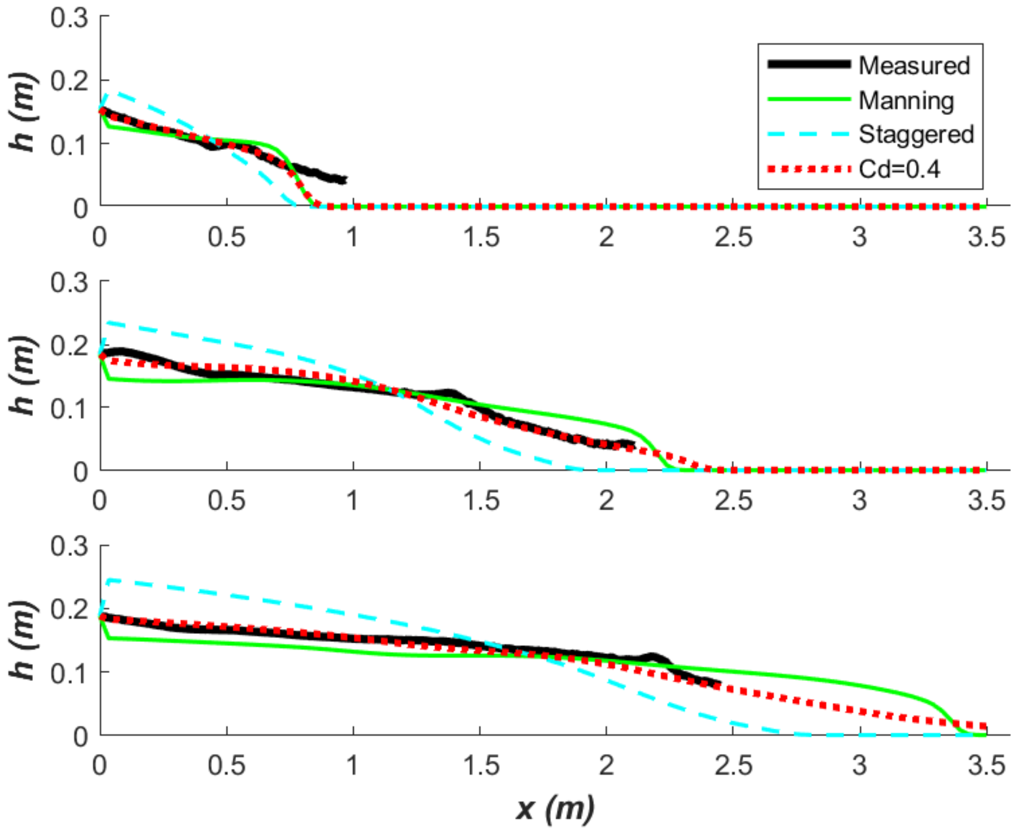

Figure 6.10. *A comparison between measured and modeled $h(x,t)$ for $S_o = 3\%$ and $H_o = 0.30m$. $h(x,t)$ measured is represented with the three $h(x,t)$ modeled ($C_{d,s}$, $C_d = 0.4$ and $n = 0.05$) for three significant times ($t = 0.5s$, $t = 1.5s$ and $t = 2.5s$). The three time instants are shown in figure 6.9 as a horizontal dashed red line.*

An example of such comparisons is shown in Figures 6.3 and 6.4 for Manning's formula with $n = 0.05$, $C_{d,s}$, and $C_d = 0.4$. Unsurprisingly, all models reproduce h reasonably at early times given the specified inflow hydrograph. However, the models begin to diverge at later times as the flood wave progresses further downstream. The comparisons with measurements are suggestive that $C_d = 0.4$ compares best. The usage of $C_{d,s}$ without any further sheltering or drag reductions overestimates $h(x,t)$ at later times (especially for the largest S_o and H_o). Manning's formula with $n = 0.05$ captures the bulk space-time patterns of the water surface but the details shapes of the water surface profile are not fully recovered.
Figures 6.11, 6.12, and 6.13 summarize the overall comparison between measured and modeled $h(x,t)$ using a constant $C_d = 0.4$, a constant $n = 0.05$, and the $C_{d,s}$ formulation with no further drag reduction. This graphs contain in the x-axis the water level normalized with H_o ahead of the dam and in the y-axis is represented the water level of each model normalized in this case too. Each colormap contains all the points of the 16 configurations for a total of more than 800000 points. The color map emphasizes the zones where the points are denser.

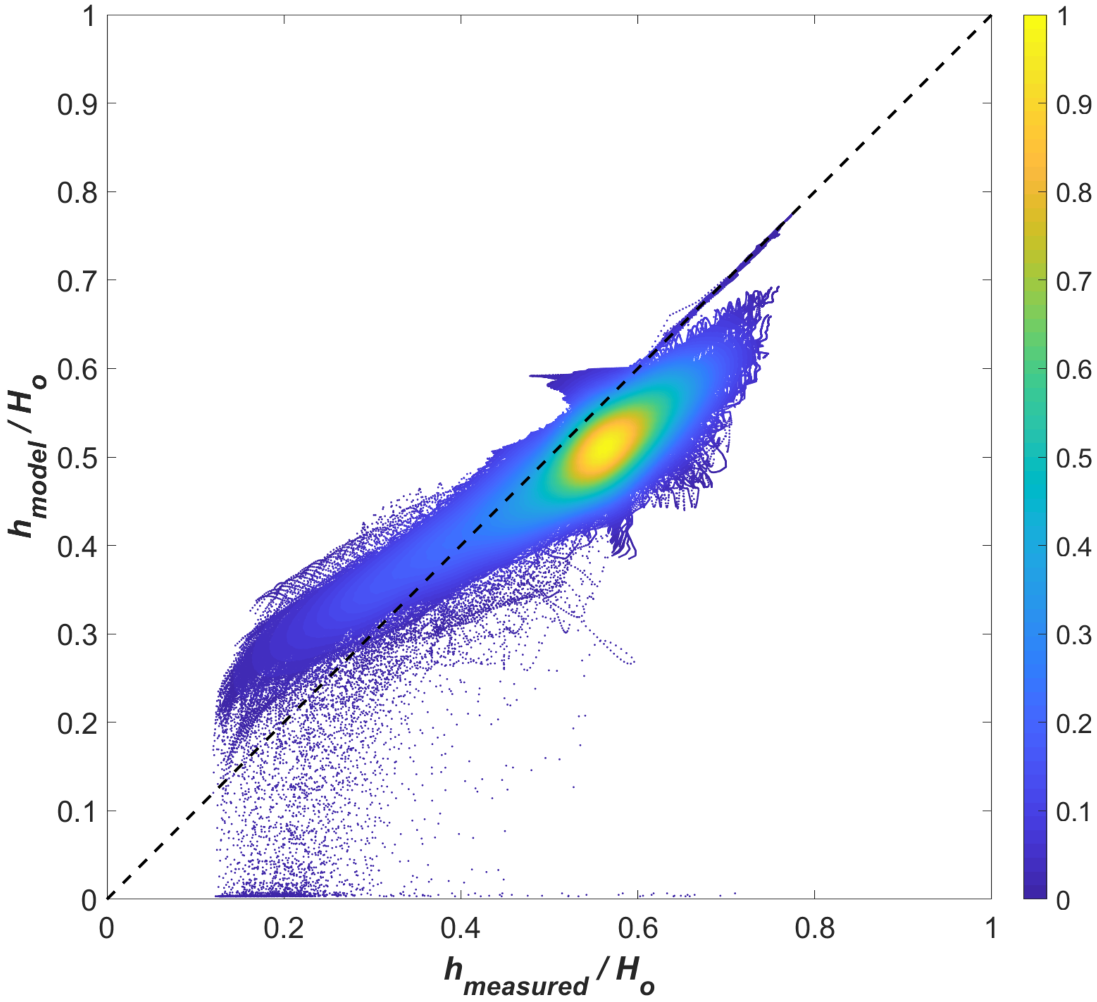

Figure 6.11. *A comparison between measured and modeled $h(x,t)$ using a Manning's formula with constant $n = 0.05$ for all (x,t) and all 16 runs. The colormap signifies density of points. The one-to-one line is also shown.*

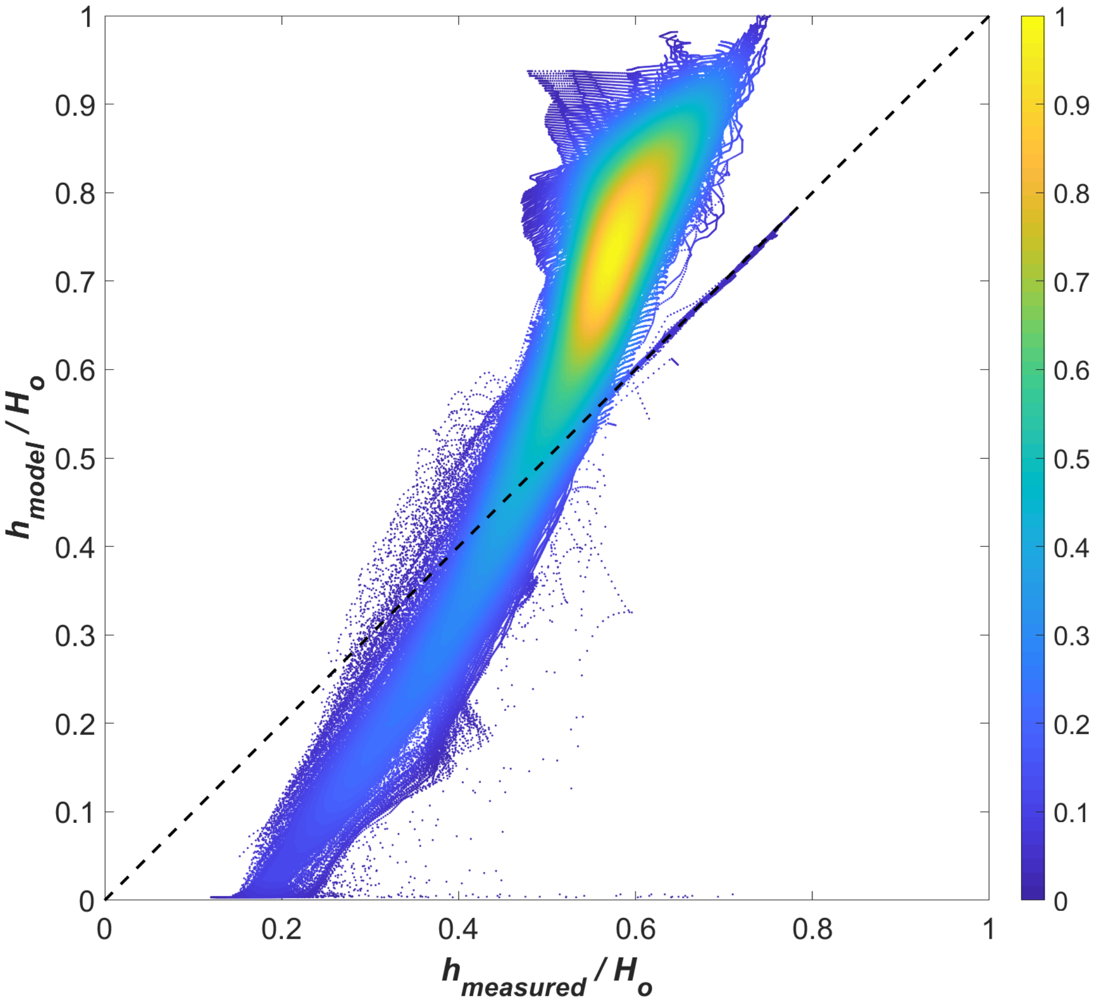

Figure 6.12. *A comparison between measured and modeled $h(x,t)$ using the staggered $C_{d,s}$ formulation for all (x,t) and all 16 runs. The colormap signifies density of points. The one-to-one line is also shown.*

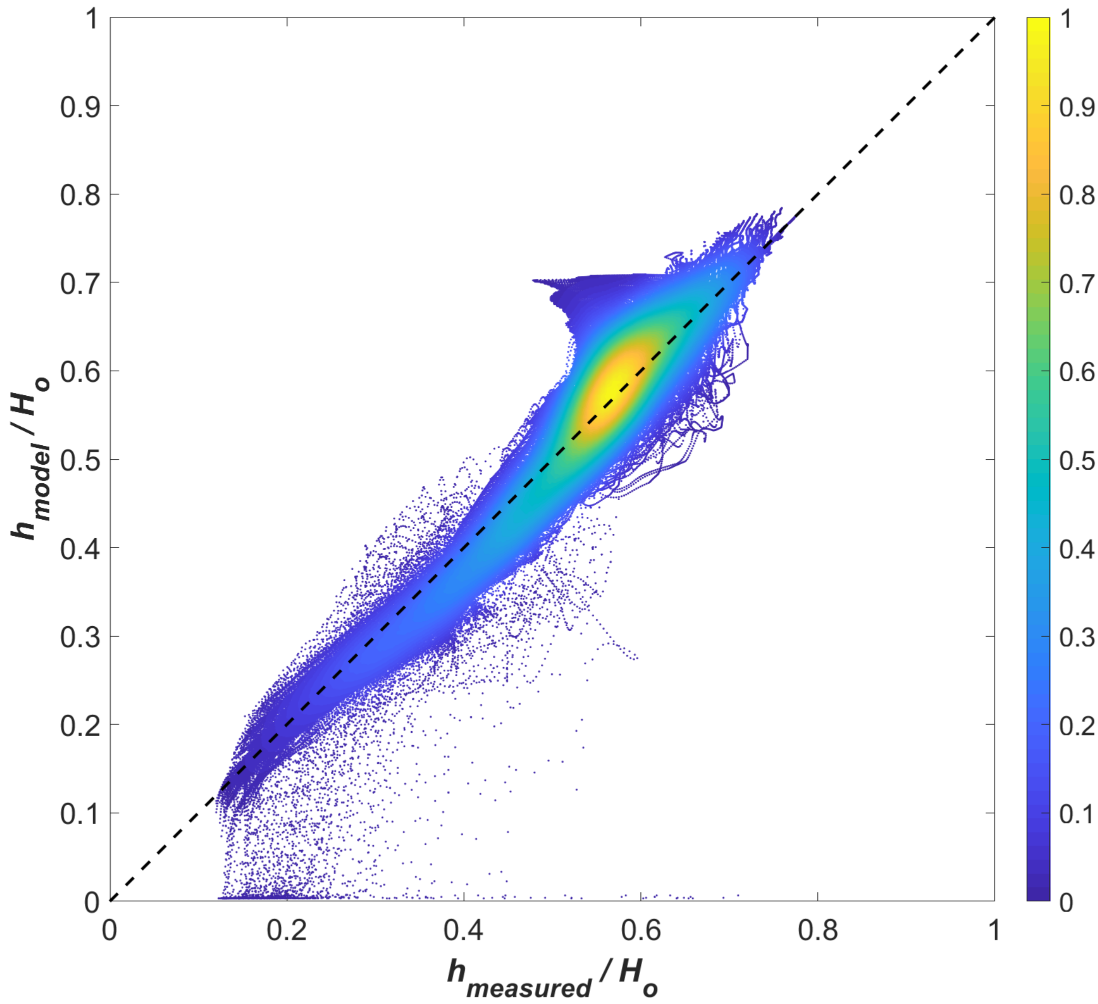

Figure 6.13. *A comparison between measured and modeled $h(x,t)$ using a constant $C_d = 0.4$ for all (x,t) and all 16 runs. The colormap signifies density of points. The one-to-one line is also shown.*

Table 6.1 summarizes the regression statistics associated with Figures 6.11, 6.12, and 6.13. The three statistics which show the well-fitting of a regression model are R-squared, the slope and the intercept of the straight line. The coefficient of determination in the case of a linear regression is the square of the correlation coefficient. The coefficient of determination ranges from 0 to 1. It is acceptable for all three models suggesting that all three models reasonably reproduce the variability in measurements. However, the model biases (interpreted here as regression intercept differing from zero and regression slope differing from unity) differ in how the frictional law is imposed and parametrized.

	Slope	**Intercept**	**R^2**
C_d=0.4	0.90	0.05	0.91
n=0.05	0.76	0.08	0.87
$C_{d,s}$	1.24	-0.03	0.87

Table 6.1. *Characteristics of the linear regression for* $C_{d,s}$, $C_d = 0.4$ *and* $n = 0.05$.

Figure 6.11 shows that Manning's formula underestimates h in the regions where h measured is high and overestimates h in the regions where h measured is low. The main reason is that for $n = 0.05$ the wave speed is matched but not the water surface profiles. If the speed of the front is equal, the profile for $n = 0.05$ will be higher than the linear profile measured as shown in 6.2. In fact according to equation 3.28 h scales as a power-law with a sub-unity exponent (i.e. $x^{3/7}$) for the constant n near the advancing wavefront.
The staggered drag coefficient formulation clearly overestimates the Drag. The formula used here it's been proven valid by Etminan [24] for the case of uniform flow and becomes inconsistent in this case. Figure 6.12 shows that $C_{d,s}$ overestimates h in the regions where h measured is high and underestimates h in the regions where h measured is low revealing an opposite pattern to Manning's formula.
The model calculations with $C_d = 0.4$, showed in figure 6.13 match closely the one-to-one line, in fact $R^2 = 0.90$ (biases are about 10%) and the slope intercept is 0.05.

7. Discussion

The main purpose of this thesis is to capture the dam-break wave propagation in situations where the resistance to the flow is not originating from side or bed friction. A hundred run tests were performed for a total of 16 different configurations.
For the dam-break problem over vegetation, the presence of a uniform rod canopy appears to simplify the description of the water surface profile in the vicinity of the advancing wavefront because C_d becomes weakly or almost independent of the Reynolds number. This simplification is in contrast to a Manning type representation for equivalent wall frictional effects with a constant n. An extensive linear $h(x)$ with x was predicted by this simplification for the advancing wave and was confirmed for all 16 configurations.
The expression for C_d is represented in Figure 3.1 for $\phi_v = 0.03$. It is shown that for large Re_d (i.e. $Re_d > \times 10^5$), C_d becomes weakly dependent on Re_d or almost entirely independent of Re_d altogether. However all the experiments and simulations run so far to determine C_d, took into account a steady state permanent flow characterized by $Re_d \leq 10000$. Thereby the right part of the graph, for around $Re_d \geq 10000$, is yet unexplored.
An unexpected result emerging from the experiments here is the significant reduction in $C_d (= 0.4)$ below its array (uniform or staggered) values reported from uniform canopy flow experiments. At high Reynolds number (but $Re_d < 3 \times 10^5$), the C_d for an isolated cylinder asymptotically approaches $C_{d,iso} = 1.2$, whereas $C_{d,s} \approx 1$ and $C_{d,a} \approx 0.8$.
What can be the cause (or causes) of such reduction in C_d? In this discussion will be offered four speculation which are i) misalignment between the total velocity vector and the cylinder axis, ii) wave effect in the flow, iii) relation between the drag and the Froude number and iiii) flow separation. Which one of this factor has a major impact on the shape of the flow is still unknown, but clearly every one has an important role into reducing the drag.

7.1 Misalignment between the total velocity vector and the cylinder axis

At high Re_d, form drag dominates over viscous drag and only the velocity component perpendicular to the individual cylinder axis must be factored into the calculations of a form-drag coefficient. The velocity component parallel to the cylinder axis does not contribute to the form drag. If the total velocity is U_T, then the velocity component responsible for the form drag here is $U_T \sin(\theta)$, where θ is the angle between U_T and the cylinder axis. It directly follows that deviations from $\theta = \pi/2$ must be accounted for using a drag reduction factor set to $[\sin(\theta)]^2$. To achieve a 50% reduction in C_d requires a $\theta = \pi/4$, which may not be large immediately after the dam break but is large at the tip of the advancing wave front. If the angle formed by the water surface profile and the vertical rods is used as a surrogate for θ, then $\theta \sim \pi/18$ (instead of $\theta = \pi/2$). Resolving θ in the vicinity of the advancing wave front was beyond the capacity of the imaging system here. Not withstanding this experimental limitation, the main message to be conveyed is that any misalignment between the velocity vector and the cylinder axis leads to reductions in C_d when compared to expectations from uniform flow experiments where $\theta = \pi/2$.

7.2 Waviness

In the last two decades several studies about the wave attenuation by vegetation were made. For example Kobayashi [44] performed many experiments in a channel equipped with a wave maker keeping the water level fixed and changing the frequency of the waves. This studies highlighted that in case of a waving flow a drag coefficient could be calibrated in function of the Reynolds number as shown in Figure 7.1.

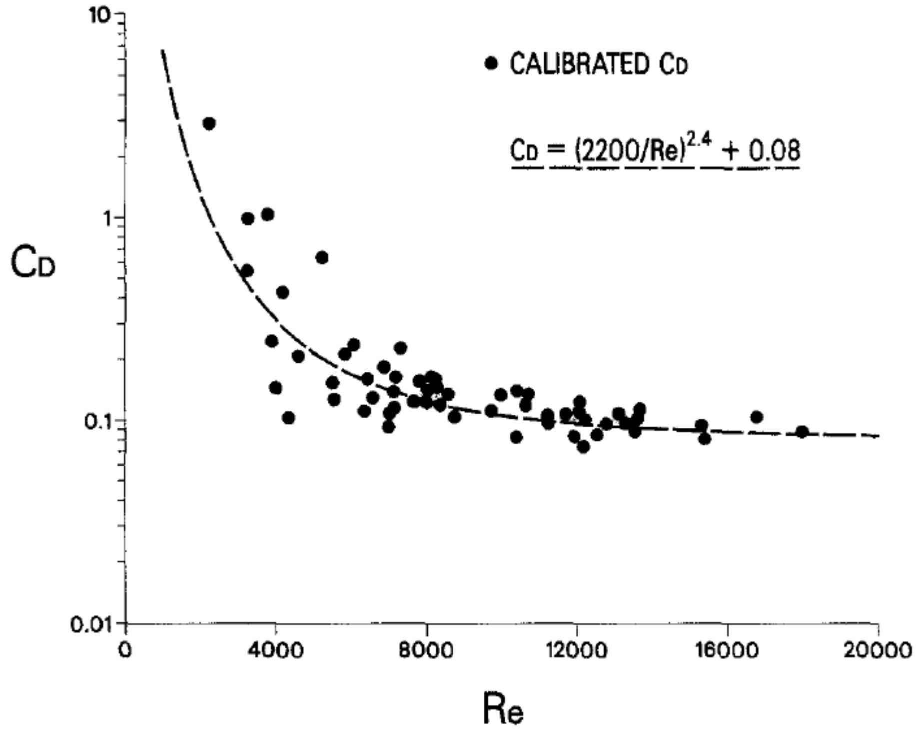

Figure 7.1. *Calibrated values of the Drag Coefficient C_d as function of Reynolds number.*

Hence the relation between C_d and Re is expressed by the following formula:

$$C_d = 0.08 + (\frac{2200}{Re})^{2.4}. \tag{7.1}$$

Equation 7.1 is empirical but describes a range of canopy density and wave frequency. The baseline C_d=0.08 value is small and is suggestive that at high Re_d, the presence of waves act to reduce C_d versus expectations from uniform pressure or gravity driven flows at the same Re_d. The physical mechanisms for the reduction in form drag are not too different from the one discussed in section 7.1 though inertial forces cannot be generally ignored in wave-driven flows. However, at large Keulegan-Carpenter numbers (KC), the form drag dominates over inertial forces and C_d may be interpreted as representing the total drag force acting on a cylinder. The assumption of a large KC may be plausible here when the front wave attains a quasi-constant U_f (i.e. $\partial U_f/\partial t$ is small). Transient waves do persist in the first 2-3s out of the 7-10s experiment duration here for each test run. However, these waves are not monochromatic (as in the case of a wave maker) and are superimposed on a rapid current entirely absent in wave-induced flows. For the purposes of discussion only, it may be argued that the limiting C_d at high Re_d (hereafter labeled as the asymptotic value) lies between 0.08 (for waves) and 0.8 (for uniform staggered dense canopy), with a mean value of about 0.4 as waves persisted about 50% of the inflow hydrograph period associated with the wave front. Upstream of the rapidly advancing wave front, the Reynolds number is lower, the water depth is gradually approaching a quasi-uniform state as evidenced by Figure 6.4, and $\partial C_d / \partial Re_d$ may follow expectations from uniform flow vegetation studies for staggered cylinders. These two arguments may be naively superimposed to yield

$$C_d = 0.4 + 10(Re)^{-2/3}, \tag{7.2}$$

which is labeled as $C_{d,s}$-modified. A global comparison between measured and modeled $h(x,t)/H_o$ for all 16 test runs is shown in Figure 7.2 and the regression statistics of this comparison are summarized in Table 7.1. A reduction in the asymptotic value of C_d from 1.0 to 0.4 improved the comparison between measurements and model calculations over the original $C_{d,s}$, but this improvement is quite minor. A global comparison in the next figure show that the water profile is well represented in the wave-front as well as in the back where the Reynolds number values are lower.

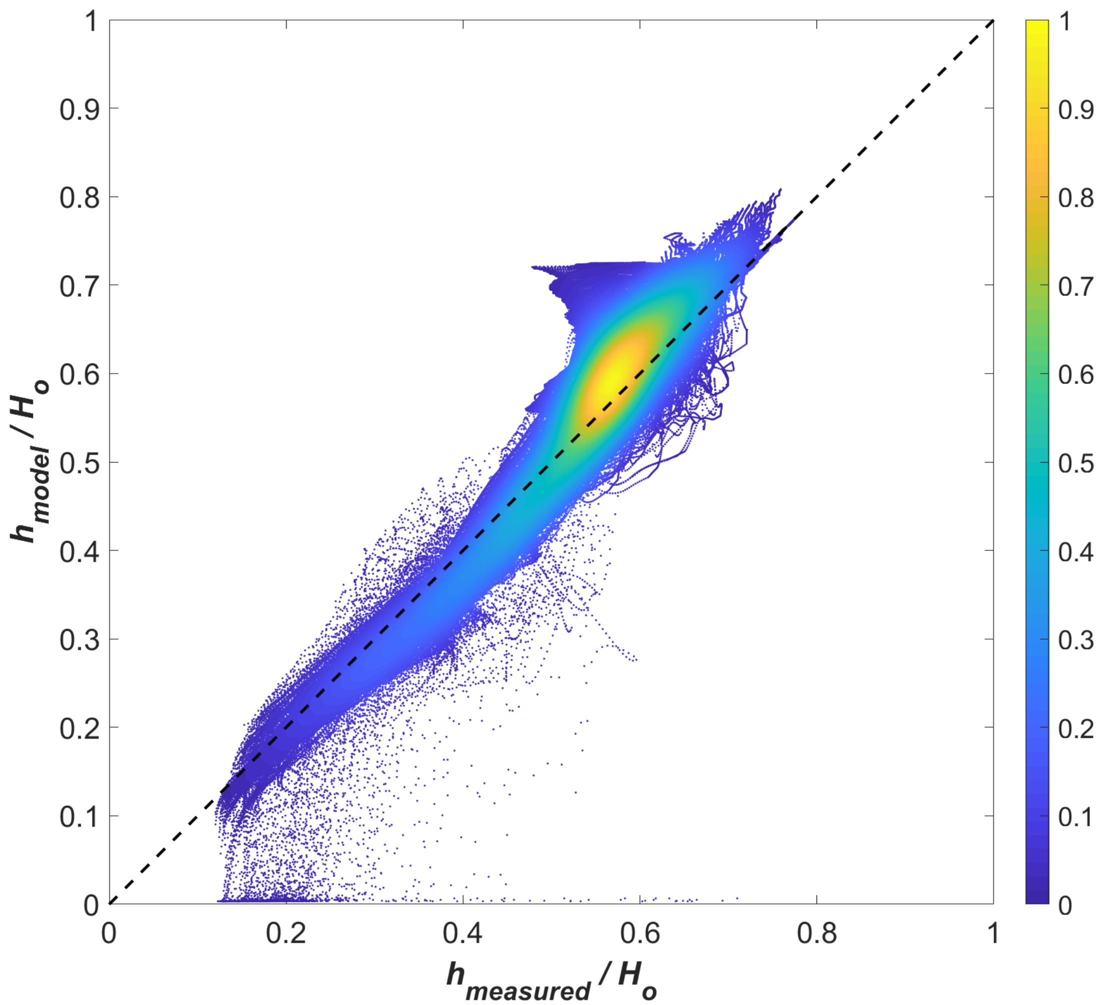

Figure 7.2. *A comparison between measured and modeled $h(x,t)$ using a Etminan's formula with reduced asymptotic limit for all (x,t) and all 16 runs. The colormap signifies density of points. The one-to-one line is also shown.*

7.3 Froude Number effects

When the flow is widely non uniform the resistance, expressed by the friction slope, is a complex function of the density of the rods, the channel bed slope, the Reynolds number as well as the Froude number. Starting from the second law of Newton it can be found that, for an unsteady inertial flow, the drag force is directly related to the Froude number.

$$\sum \vec{F} = m\vec{a}, \tag{7.3}$$

$$\sum \vec{F} = m\frac{\partial \vec{V}}{\partial t}, \tag{7.4}$$

$$\sum \vec{F} = \frac{\partial}{\partial t} m\vec{V}, \tag{7.5}$$

the mass m can be express as Volume W multiplied for ρ, hence

$$\sum \vec{F} = \frac{\partial}{\partial t} W\rho\, \vec{V}, \tag{7.6}$$

ρ is constant, follow that

$$\sum \vec{F} = \rho\frac{\partial}{\partial t} W\, \vec{V}. \tag{7.7}$$

If the derived is expanded ρ is constant, follow that

$$\sum \vec{F} = \rho\left[W\frac{\partial V}{\partial t} + \vec{V}\frac{\partial W}{\partial t}\right]. \tag{7.8}$$

In the frontwave tip the velocity V is approximately constant and $\frac{\partial W}{\partial t} = Q$, hence

$$\sum \vec{F} = \rho\vec{V}Q, \tag{7.9}$$

$$\sum \vec{F} = \rho Q(V_2 - V_1). \tag{7.10}$$

Taken a control volume, where $Q = BVh$ the conservation of momentum can be expressed by

$$\rho g\frac{h_1^2}{2}B + \rho(V_1 h_1 B)V_1 = \rho g\frac{h_2^2}{2}B + \rho(V_2 h_2 B)V_2, \tag{7.11}$$

dividing by ρ and B

$$g\frac{h_1^2}{2} + V_1^2 h_1 = g\frac{h_2^2}{2} + V_2^2 h_2, \tag{7.12}$$

rearranging the terms

$$V_1^2 h_1\left[\frac{gh_1}{2V_1^2} + 1\right] = V_2^2 h_2\left[\frac{gh_2}{2V_2^2} + 1\right], \tag{7.13}$$

considering that $V_1 = V_2 = constant$ in the wave front tip, the conservation of momentum show that the water level is a function excusively of the Froude number:

$$h_1\left[\frac{1}{2}\frac{1}{Fr_1} + 1\right] = h_2\left[\frac{1}{2}\frac{1}{Fr_2} + 1\right]. \tag{7.14}$$

Therefore the drag force that equilibrates the hydrostatic pressure can be wrote as a function of Froude number.

For example, the Chezy expression where the resistance stress is expressed in kinematic form as $C_h U^2$ results in

$$Fr = \frac{U}{\sqrt{gR_h}} = \sqrt{\frac{S_o}{C_h}}, \tag{7.15}$$

where C_h is the Chezy constant. Re-arranging this expression yields

$$C_h = \frac{S_o}{Fr^2}. \tag{7.16}$$

For vegetated canopies, C_h can be related to C_d, which must then be inversely related to Fr. The relation between the drag coefficient C_d and the Froude number Fr has already been experimentally explored by Yoshiharu Ishikawa [34] and it is shown in the next figure:

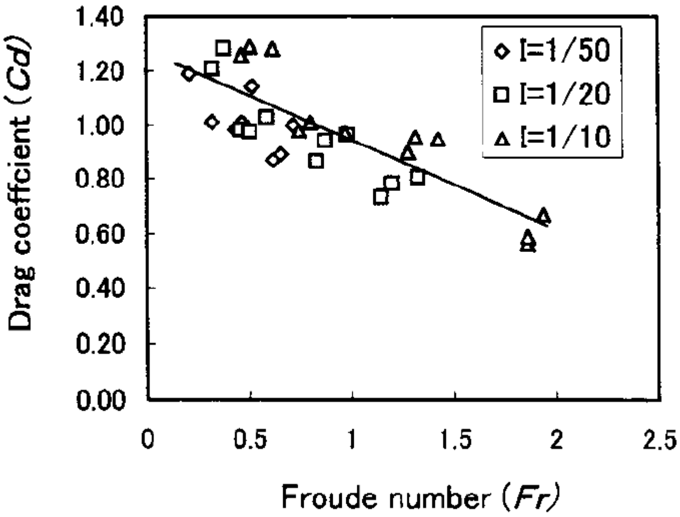

Figure 7.3. *Calibrated values of the Drag Coefficient C_d as function of Froude number.*

In particular the experimental data are well fitted with a power low function:

$$C_d = 1.24 - 0.32Fr. \tag{7.17}$$

For the dam-break problem, the wave front velocity U_f approaches a near constant value with increasing x; However, $\sqrt{R_h}$ is decreasing resulting in Fr that increases with increasing x. The immediate consequence of this analysis is that $\partial Fr/\partial x$ is expected to be positive with increasing x. Based on equation 7.17, $\partial C_d/\partial x$ is negative in the vicinity of the wave front due to depth non-uniformity. A C_d that only varies with $Re_d = UD/\nu$ simply cannot detect this decline because $U \approx U_f$ is not changing in space whereas R_h in the vicinity of the wave front is. The only way to accommodate this C_d decline in a $C_d - Re_d$ expression is to artificially reduce C_d below expectations from uniform flow in canopies (here $C_{d,s}$). Hence, it is conceivable that a reduced $C_d = 0.4$ is simply an artifact of modeling C_d by Re_d and h or R_h variations cannot be accommodated. Hence, an alternative to a $C_d - Re_d$ expression is now explored based on an expression that resembles equation 7.17. To maintain tractability, it was assumed that

$$C_d = a_1 + a_2(Fr)^{a_3}, \tag{7.18}$$

where $a_1 = 1.24$, $a_2 = -0.32$, and $a_3 = 1$ recovers the best-fit curve to the laboratory experiment for uniform emergent canopy flow described elsewhere [34]. Using the same subset of the data used to determine $n = 0.05$ and $C_d = 0.4$, best-fit parameters were determined to be here $a_1 = 0.1$, $a_2 = 0.25$, and $a_3 = -0.5$.

$$C_d = 0.1 + 0.25(Fr)^{-0.5}. \tag{7.19}$$

Upon comparing the values determined for the dam-break problem here with those in equation 7.17, a number of clarifications must be made: (1) Equation 7.17 predicts a $C_d < 0$ when $Fr > 3.87$ whereas the derived expression here predicts a saturating $C_d \approx 0.1$ for large Fr; (2) the derived expression here predicts a $C_d \in [0.24, 0.36]$ for $Fr \in [1, 4]$ (i.e. spanning the entire super critical regime encountered in vicinity of the modeled wave front); (3) for $Fr < 1$, C_d increases rapidly with decreasing Fr but remains well below predictions from equation 7.17. It appears that the best fit C_d to equation 7.18 remains well below equation 7.17 even in the region far upstream of the wavefront where the flow is quasi-uniform.

As a final check, we used $a_1 = 0.1$, $a_2 = 0.25$, and $a_3 = -0.5$ in equation 7.18 (labeled as C_d−Froude) to predict $h(x,t)/H_o$ for all 16 runs. A comparison between measured and modeled water levels is summarized in Table 7.1. Overall, the performance of the model in equation 7.18 is no worse than a $C_d = 0.4$ suggesting that the tendency to drop C_d below its uniform staggered arrangement value is not an artifact of the choice of an Re_d that is insensitive to R_h. A global comparison with C_d as a function of Re follows

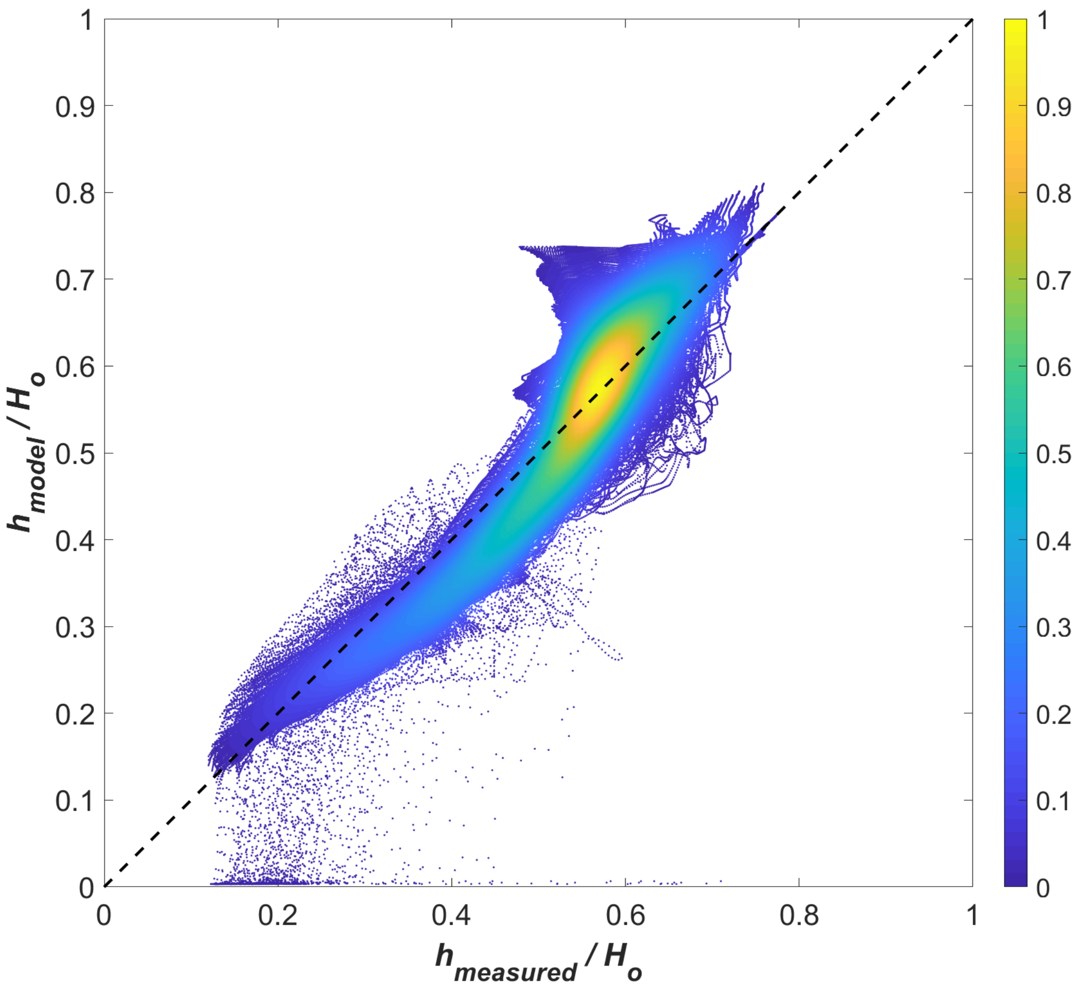

Figure 7.4. *A comparison between measured and modeled $h(x,t)$ using C_d as a function of Fr all (x,t) and all 16 runs. The colormap signifies density of points. The one-to-one line is also shown.*

7.4 Separation

For an isolated cylinder with $Re_d < 3 \times 10^5$, the boundary layer attached to the cylinder is laminar and generally separates on the front half leading to the formation of wakes behind the cylinder. For dense canopies, sheltering is linked to interactions between those wakes. The pressure in the separated region on the downstream side of an isolated cylinder is nearly constant but still smaller than the free stream pressure resulting in a large C_d. This is the situation that was considered in prior studies dealing with separation for uniform flow within staggered vegetated systems [24]. For $Re_d > 3 \times 10^5$, the aforementioned separation mechanism becomes far more complex. The laminar boundary layer that is just beginning to the form at the tip of the front half of the cylinder becomes unstable over a very short distance. The shear layer switches to a turbulent state and reattaches to the front half of the cylinder. However, this newly formed turbulent boundary layer itself separates from the cylinder on the back-half. The net result is that the separation region has decreased and the pressure in this region nearly returns to its free stream value causing a major decline in C_d that is well over 70$\%$ (for isolated cylinders).
While the Re_d in the wave front region of the dam-break problem is lower than 3×10^5 by an order of magnitude, the flow is highly disturbed and unsteady. In fact, the acquired movies show instances of water splashing around the rods. These large disturbances and flow unsteadiness cause rapid destabilization of the embryonic laminar boundary forming on the front side of the cylinder thereby eliciting an early transition to turbulence. If the turbulent shear layer experiences late separation on the back side of the cylinder, then the overall bulk C_d can drop by 50$\%$. In fact, if separation occurs midway on the back side of the cylinder, then the effective frontal area (or D_{eff}) will be reduced by a factor 2. This reduction from D to D_{eff} alone leads to a factor of 2 reduction in $C_d m D_{eff}$ even when setting $C_d = C_{d,s}$ at the same Re_d. This scenario cannot be overlooked or dismissed and may explain the weak dependence of C_d on Re_d reported here. The necessary (but not sufficient) conditions for its occurrence is that Re_d as well as the disturbances to the embryonic laminar boundary at the tip of the front side of the cylinders remain large to destabilize it. As an indirect check on such a separation, the calculations are repeated for the entire 16 runs with C_d set to a $C_{d,s}$ formulation using $D_{eff} = 0.5D$ (to reflect a reduction in the wake region behind the cylinder). This reduction in D also reduces Re_d, and hence a lower Re_d and higher C_d is expected away from the advancing wave front with such a D_{eff} revision. The comparison between measured and modeled water levels is also summarized in Table 7.1. Overall, the performance of the model in equation 7.18 is a small improvement over the constant $C_d (= 0.4)$. That is, accentuating the Re_d effects on C_d confers minor benefits to the comparison between measured and modeled h/H_o and the separation argument may be plausible.
In the next table are represented the three Cd cases discussed from the beginning and the two new C_d values proposed. Although Cd_{Froude} globally well represents the water profile, $C_{d,s}$ with the modified baseline is the best fit proposed.

	Slope	**Intercept**	**R^2**
C_d=0.4	0.90	0.05	0.91
n=0.05	0.76	0.08	0.87
$C_{d,s}$	1.24	-0.03	0.87
$C_{d,s}$modified	0.93	0.05	0.91
$C_{d,Froude}$	0.89	0.06	0.89
$C_{d,Separation}$	0.96	0.04	0.91

Table 7.1. Characteristics of the linear regression for $C_{d,s}$, $C_d = 0.4$, $n = 0.05$, $C_{d,s}modified$ and $C_dFroude$

8. Conclusions

The work here considered the effects of hydraulic resistance on the downstream evolution of the water surface profile $h(x,t)$ in a long sloping prismatic channel covered by a uniform dense rod canopy following the collapse of a dam. The focus was on the link between the sought friction slope S_f in the SVE and vegetation roughness. The 16 configurations analyzed regarded four water levels behind the dam (H_o = 0.15m, 0.20m, 0.25m, 0.30m) and four differing bed slopes (S_o = 0%, 1%, 2%, 3%) for a total of 100 test runs. In particular, the way in which drag slows the propagation of the advancing wave front was determined using three broad classes of friction models: a frictionless model with $S_f = 0$ (the Ritter solution) was used a reference, S_f described by wall or Coulomb friction (Manning's formula with constant roughness n), and a distributed drag force formulation where the drag coefficient C_d was modeled using standard equations for isolated cylinders, array of uniformly spaced cylinders, and cylinders positioned in a staggered arrangements. The following conclusions can be drawn from the experiments, model results, and simulations: (i) When setting $S_f = 0$, the Ritter's solution under-predicted the measured water level for a given wave front velocity as expected. The largest difference between measured and modeled water level was immediately after the dam but prior to the commencement of the vegetated section, where the Ritter Solution under-predicted the water level at this point by some 30%. Also, with increasing wave front speed, the measured drop in h was steeper than predictions by the Ritter solution suggesting (gS_f) was a significant term in the Saint-Venant equation. (ii) When modeling S_f with wall (or Coulomb) friction as common to Manning's formula with constant n, it was possible to match the measured wave front speed with plausible values of n(≈0.05) but not the precise shape of h. The water surface profile from a Manning representation for S_f was shown to be a power-law in x with a sub-unity exponent at any given t. (iii) When modeling S_f using a distributed drag force with constant C_d, agreement between measurements and model calculations was satisfactory with a coefficient of determination exceeding 0.9 and regression slopes deviating from unity by less than 10%. The model also predicted that the shape of the water surface profile near the wave front is quasi-linear in x and can be theoretically linked to C_d. (iv) A computed constant $C_d \approx 0.4$ from such links is much smaller than C_d reported for uniform flow experiments with staggered cylinders at the same element Reynolds number. This suggests that drag reduction mechanisms associated with non-uniformity, unsteadiness and transient waves, and flow disturbances are more likely when compared to conventional sheltering effects.

The broader implications of this work highlights a need for new frictional laws describing S_f in disturbed non-steady non-uniform flow conditions beyond conventional wall or Coulomb friction representations. These developments are likely to be imminently used when combining such models for closing the SVE with water level data acquired from space [3, 4, 2]. There is some urgency for progress on this front as climate change may result in more frequent flooding events and improving flood warning and monitoring systems is of obvious societal significance.

A. MATLAB Codes

A.1 Script to detect the water surface profile

```
clear all
close all
clc

%% Step 1: Definition of image boundaries.

I=imread('img19_p1.png');
cut=I(150:640,350:1630,:);

%% Step 2: Count of the number of frames.
v=VideoReader('Surface_cut.mp4'); % Movie loading.
j=0;
while hasFrame(v) %Cycle to calculate the number of frames.
    j=j+1;
    a=readFrame(v);
end
S=size(a); % Frame dimension in pixel.

%% Step 3: Each frame is loaded into a structure.
clear v a
v=VideoReader('Surface_cut.mp4');
Video(j)=struct('img',[],'imgcut',[],'profile',[],'profile_tot',[]);
% Video is the structure carrying the frames.
k=0;
% Each frame is loaded into a structure called "Video".
while hasFrame(v)
    k=k+1;
    Video(k).img=readFrame(v);
end
figure
imshow(Video(8).img); %The dam-break frame is detected.

%% Step 4: Images cutting.

for n=1:j % This cycle eliminates the unuseful pixels in
    %each image.
    Video(n).imgcut=Video(n).img(150:640,350:1630,:);
end
```

```
figure
imshow(Video(8).imgcut); % The dam-break frame is showed
%in a new image where the size is smaller.
s=size(Video(68).imgcut); % Count of the number of pixels
%forming the new image.

%% Step 5: Water surface Detecting
h=640; %h is the horizontal dimension indicating where
%the lighting is lower.Hence each image is divided in
%two parts, with two different color tollerances.
for nn=8:3:371 % Each movie is analyzed from the dam-break
    %frame (number 8) + 7.2 seconds.
    for m=1:h % Horizontal dimension.
        for l=1:s(1) % Vertical dimension.
          if Video(nn).imgcut(l,m,1)<115 && Video(nn).imgcut(l,m,3)<160
                %Red and blue tolerances.
                Video(nn).profile(l,m,1)=255;
                Video(nn).profile(l,m,2)=255;
                Video(nn).profile(l,m,3)=255;
%If the tolerance is respected a black dot
% in a white figure is printed.
            else
                Video(nn).profile(l,m,1)=0;
                Video(nn).profile(l,m,2)=0;
                Video(nn).profile(l,m,3)=0;
                blapos(nn,m)=l;
                % The rows indicates the frame number,
                % the columns indicate the abscissa of
                % the frame (starting from left).
                for x=(l+1):s(1)
                    Video(nn).profile(x,m,1)=255;
                    Video(nn).profile(x,m,2)=255;
                    Video(nn).profile(x,m,3)=255;
                end
                break
            end
        end
    end
    for m=h+1:s(2) % Horizontal dimension.
        for l=1:s(1) % Vertical dimension.
            if Video(nn).imgcut(l,m,1)<120
                % From the horizontal value 'h'
                % the lighting is worst.
                % The red tolerance is lower.
                Video(nn).profile(l,m,1)=255;
                Video(nn).profile(l,m,2)=255;
                Video(nn).profile(l,m,3)=255;
            else
                Video(nn).profile(l,m,1)=0;
                Video(nn).profile(l,m,2)=0;
```

```
                Video(nn).profile(l,m,3)=0;
                pronum(nn).oz(l,m)=0; % nero
                blapos(nn,m)=l;
                % The rows indicates the frame number,
                % the columns indicate the abscissa of
                % the frame (starting from left).
                for x=(l+1):s(1)
                    Video(nn).profile(x,m,1)=255;
                    Video(nn).profile(x,m,2)=255;
                    Video(nn).profile(x,m,3)=255;

                end
                break
            end
        end
    end

    Video(nn).profile_tot=255*ones(1080,1920,3);
    Video(nn).profile_tot(150:640,350:1630,:)=Video(nn).profile;
end
% It is shown a sample image of the detected water surface.
figure
imshow(Video(68).profile);

save Profilis blapos

%% Step 6: Recalculation of the pixel coordinates
%in the whole image.
b=size(blapos);
Profile(j)=struct('img',[]);
for a=8:3:371
    for aa=1:b(2)
        Profile(a).img(:,aa)=[aa+349 blapos(a,aa)+149];
    end
end

save pro_to_chess_p1_30_3_1 Profile

%% Step 7: Images Printing.
% The detected surface is printed in green on top
% of each image. This process is useful
% to assess the precision of the script.
for nn=8:3:371
   for c=1:b(2)
        x=Profile(nn).img(1,c);
        y=Profile(nn).img(2,c);
        Video(nn).img(y,x,1)=10;
        Video(nn).img(y,x,2)=250;
        Video(nn).img(y,x,3)=10;
   end
```

```
    cat=Video(nn).img(150:640,350:1630,:);
    figure(nn)
    imshow(cat);
    saveas(nn,sprintf('FIG%d.png',nn));
end
```

A.2 Script to switch from Pixel Coordinates to Metric Coordinates

```
clc
close all
clear all

%% Step 1: The camera parameters ("cameraParams"), calculated
% by using "Camera Calibrator" must be manually loaded.

% Images is a variable containg the twenty pictures of the
% checkerboard.
images = imageDatastore(fullfile(toolboxdir('vision'),
'visiondata' ,'calibration','Camera1'));

%% Step 2: Detection of the checkerboard corners in the images.
% The last image is left for testing.

[imagePoints,boardSize]=detectCheckerboardPoints(images.Files(1:end));

%% Step 3: Generation of a checkerboard in metric coordinates.
% worldPoints is a matrix containing the metric coordinates of
% the checkerboard squares.

squareSize = 50; % millimeters
worldPoints = generateCheckerboardPoints(boardSize,squareSize);

% Reading of the last image.
I = imread('C:\Program Files\MATLAB\R2017b\toolbox\img19.png');
imageSize = [size(I,1) size(I,2)];

%Detecting of the checkerboard point in the last image.
imagePoints = detectCheckerboardPoints(I);

%Calculation of the Rotation matrix and translation vector.
[R,t] = extrinsics(imagePoints,worldPoints,cameraParams)

% Determination of the newWorldPoints. This matrix contains the
% checkerboard corners in metric coordinates obtained by using
% the Camera Parameters to trasfmorm the corners of the
% checkerboard detected in image19 in pixel coordinates.
newWorldPoints = pointsToWorld(cameraParams,R,t,imagePoints);


%% Fase 4: Precision evaluation.
```

```
plot(worldPoints(:,1),worldPoints(:,2),'gx');
hold on
plot(newWorldPoints(:,1),newWorldPoints(:,2),'ro');
legend('Ground Truth','Estimates');


%% Fase 5: The matrix containing the pixel coordinates of the
% water surface profile is loaded.

load('pro_to_chess_30_3_1.mat')

%'pro_to_chess_30_3_1.mat' is the matrix containing the water
% profile in pixel coordinates. Each frame is transformed in
% metric coordinates by using the function pointsToWorld.
% "matrice" is the matrix carryng the metric coordinates of
% each profile.

matrice(241)=struct('real',[]);
for a=9:3:249
   prof=(Profile(a).img)';
   mat = pointsToWorld(cameraParams,R,t,prof);
   matrice(a).real = mat;
   matrice(a).real=[matrice(a).real(:,1) 350-matrice(a).real(:,2)];
end


%% Fase 6: Results checking.

% It is plotted  the profile in metric coordinates in order
% to check the success of the procedure.
matr = (Profile(3).img)';
newmatrice = pointsToWorld(cameraParams,R,t,matr);
matrix = [newmatrice(:,1) newmatrice(:,2)]
hold on
plot(newmatrice(:,1),350 - newmatrice(:,2),'mx');
hold on
plot (matrix(:,1),matrix(:,2),'bx');


%% Fase 7: Results storing.

% The matrix carrying the water surface in metric
% coordinates is saved.
save cm_30_3_1 matrice
```

A.3 Script to assemble the water surface profiles

```
clear all
close all
clc
```

```
%% Step 1: loading of the water surface profiles in metric
%  coordinates for the three cameras.

load('cm_p1_15_1_1.mat');
One=matrice(1:364);
load('cm_p1_15_1_2.mat');
Two=matrice(1:364);
load('cm_p1_15_1_3.mat');
Three=matrice(1:364);

clear matrice;

%% Step 2: Water surface profile assembling.

% The left edge of the steel structure separating the first
% and the second glass is 40+1.8=52.8 cm from the cofferdam.
% The distance between the edge of the steel structure and
% the right edge of the checkerboard is 1.21 cm.

% The left edge of the steel structure separating the second
% and the third glass is  150.6+1.8=152.4 cm from the cofferdam.
% The distance between the edge of the steel structure and
% the right edge of the checkerboard is 2.57 cm.

% The distances are represented in mm.
S=size(One);
proftot(S(2))=struct('real',[],'nothou',[],'interpol',[],'trec',[]);
for j=1:3:S(2)
    % Glass 1.
    One(j).real=[-(One(j).real(:,1)-418) One(j).real(:,2)+50];
    a=One(j).real(:,2);
    a(a>154)=1000; %All the point above a fixed height are
    % transformed to 10m.
    One(j).real(:,2)=a;

    % Glass 2.
    Two(j).real=[-(Two(j).real(:,1)-1439) Two(j).real(:,2)+53];
    a=Two(j).real(:,2);
    a(a>130)=1000; %All the point above a fixed height are
    % transformed to 10m.
    Two(j).real(:,2)=a;

    % Glass 3.
    Three(j).real=[-(Three(j).real(:,1)-2437) Three(j).real(:,2)+50];
    a=Three(j).real(:,2);
    a(a>100)=1000; %All the point above a fixed height are
    % transformed to 10m.
    Three(j).real(:,2)=a;
```

```
    % Profiles assembling.
    proftot(j).real=[One(j).real;Two(j).real;Three(j).real];
end
```

A.4 Script to eliminate the outliers

```
clc
close all
clear all

%% Step 1- Elimination of the points moved to 1000mm.

for j=1:3:S(2)
    ind=0;
    s=size(proftot(j).real);
    for k=1:s(1)
        if proftot(j).real(k,2)~=1000
            ind=ind+1;
            proftot(j).nothou(ind,1)=proftot(j).real(k,1);
            proftot(j).nothou(ind,2)=proftot(j).real(k,2);
        else
        end
    end

end
clear k

%% Step 2: Elimination of all the points beneath 35 mm which
%% can not be detected by the cameras.

for j=1:3:S(2)
    ind=0;
    s=size(proftot(j).nothou);
    for k=1:s(1)
        if proftot(j).nothou(k,2)>35
            ind=ind+1;
            proftot(j).trec(ind,1)=proftot(j).nothou(k,1);
            proftot(j).trec(ind,2)=proftot(j).nothou(k,2);
        else
        end
    end
end

% Definition of three new structures.
profilosorted(364)=struct('real',[]);
fitting(364)=struct('real',[]);
finale(364)=struct('real',[]);

%% Step 3: Interpolating polynomial.
% For each frame the water levels are sorted from the smallest to
```

```
% the biggest values; this procedure is fundamental in
% order to use Polyfit. Polyfit allows to plot
% an interpolating polynomial for each profile.

 for k=364:-3:1

   b=sortrows(proftot(k).trec,1);
   profilosorted(k).real=b;
   p = polyfit(profilosorted(k).real(:,1),profilosorted(k).real(:,2),8);
   % The polynomial interpolating grade is 8.
   x1 = profilosorted(k).real(:,1);
   y1 = polyval(p,x1);

   fitting(k).real(:,1)=x1;
   fitting(k).real(:,2)=y1;
 end

%% Step 4: Outliers elimination.
% The outliers are investigated by setting that if the distance
% between a point of the interpolating polynomial and the point
% with the same  abscissa of the detected water surface is
% bigger than 3mm, the point must be eliminated.
% Those points are transformed to 180mm and eliminated later.

for k=364:-3:1
     B=size(profilosorted(k).real);
     for n=1:1:B(1)
if abs(profilosorted(k).real(n,2)-fitting(k).real(n,2))>12
    outlier=180;
    finale(k).real(n,2)=outlier;
else
    outlier=[profilosorted(k).real(n,2)];
  finale(k).real(n,2)=outlier;
end
end
end

% Definitivo is the structure containing the profiles
% without the outliers.

definitivo(364)=struct('real',[]);
 for f=364:-3:1
       v=profilosorted(f).real(:,1);
       g=finale(f).real(:,2);
       definitivo(f).real=[v,g];
 end


% The original water surface profiles are plotted with the
% profiles cleaned up from outliers.
```

```
 for t=241:-3:1
      figure
      subplot(2,1,1);
      plot(definitivo(t).real(:,1),definitivo(t).real(:,2),'.');
      axis([-500 3000 0 200]);
      subplot(2,1,2);
      plot(fitting(t).real(:,1),fitting(t).real(:,2));
      hold on
      plot(proftot(t).trec(:,1),proftot(t).trec(:,2),'.');
      axis([-500 3000 0 200]);
 end

%% Step 5: Elimination of the last 3 points of each profile.
% These points, being usually outliers, are transformed to 180mm
% and eliminated in the next fase.

cresta(364)=struct('real',[],'definitivo',[]);
for y=364:-3:1
    D=size(definitivo(y).real);
    for r=1:1:D(1)-3
        cresta(y).real(r,1)=definitivo(y).real(r,1);
        cresta(y).real(r,2)=definitivo(y).real(r,2);
    end
    for r=D(1)-2:1:D
        cresta(y).real(r,2)=180;
        cresta(y).real(r,1)=definitivo(y).real(r,1);
    end
end


%% Step 6: Elimination of the points with y=180mm.

for x=364:-3:1
    ind=0;
    q=size(cresta(x).real);
    for k=1:q(1)
        if cresta(x).real(k,2)~=180
            ind=ind+1;
            cresta(x).definitivo(ind,1)=cresta(x).real(k,1);
            cresta(x).definitivo(ind,2)=cresta(x).real(k,2);
        else
        end
    end
end

%% Step 7: Results storing.

 profilo_p1_15_1(364)=struct('real',[]);
for j=364:-3:1
```

```
    xx=cresta(j).definitivo(:,1);
    y=cresta(j).definitivo(:,2);

    profilo_p1_15_1(j).real = [xx,y];
end

save profilo_p1_15_1 profilo_p1_15_1
```

A.5 Script to interpolate and average the water level surface profiles

```
clc, clear all, close all

%% Step 1: All the 10 run tests are loaded (Ho=15cm, So=0).

load('profilo15_12.mat');
load('profilo15_13.mat');
load('profilo15_14.mat');
load('profilo15_15.mat');
load('profilo15_18.mat');
load('profilo15_20.mat');
load('profilo15_21.mat');
load('profilo15_22.mat');
load('profilo15_23.mat');
load('profilo15_24.mat');

 %% Step 2: Each water level profile is interpolated
 %% separately.

% Interpolation
for j=4:3:241
   x=profilo15_12(j).real(:,1);
   y=profilo15_12(j).real(:,2);
    xint=(0:1:2500)';
    yint=interp1(x,y,xint);
    profilo15_12(j).interpolated(:,1)=xint;
    profilo15_12(j).interpolated(:,2)=yint;
   Q=profilo15_12(j).interpolated(:,2);
   Q(isnan(Q))=0;
    profilo15_12(j).interpolated(:,2)=Q;
end

% Interpolation
for j=4:3:241
   x=profilo15_13(j).real(:,1);
   y=profilo15_13(j).real(:,2);
    xint=(0:1:2500)';
    yint=interp1(x,y,xint);
    profilo15_13(j).interpolated(:,1)=xint;
    profilo15_13(j).interpolated(:,2)=yint;
```

```
    Q=profilo15_13(j).interpolated(:,2);
    Q(isnan(Q))=0;
    profilo15_13(j).interpolated(:,2)=Q;
end

% Interpolation
for j=4:3:241
    x=profilo15_14(j).real(:,1);
    y=profilo15_14(j).real(:,2);
    xint=(0:1:2500)';
    yint=interp1(x,y,xint);
    profilo15_14(j).interpolated(:,1)=xint;
    profilo15_14(j).interpolated(:,2)=yint;
    Q=profilo15_14(j).interpolated(:,2);
    Q(isnan(Q))=0;
    profilo15_14(j).interpolated(:,2)=Q;
end

% Interpolation
for j=4:3:241
    x=profilo15_14(j).real(:,1);
    y=profilo15_14(j).real(:,2);
    xint=(0:1:2500)';
    yint=interp1(x,y,xint);
    profilo15_14(j).interpolated(:,1)=xint;
    profilo15_14(j).interpolated(:,2)=yint;
    Q=profilo15_14(j).interpolated(:,2);
    Q(isnan(Q))=0;
    profilo15_14(j).interpolated(:,2)=Q;
end

% Interpolation
for j=4:3:241
    x=profilo15_15(j).real(:,1);
    y=profilo15_15(j).real(:,2);
    xint=(0:1:2500)';
    yint=interp1(x,y,xint);
    profilo15_15(j).interpolated(:,1)=xint;
    profilo15_15(j).interpolated(:,2)=yint;
    Q=profilo15_15(j).interpolated(:,2);
    Q(isnan(Q))=0;
    profilo15_15(j).interpolated(:,2)=Q;
end

% Interpolation
for j=4:3:241
    x=profilo15_18(j).real(:,1);
    y=profilo15_18(j).real(:,2);
    xint=(0:1:2500)';
    yint=interp1(x,y,xint);
```

```
    profilo15_18(j).interpolated(:,1)=xint;
    profilo15_18(j).interpolated(:,2)=yint;
    Q=profilo15_18(j).interpolated(:,2);
    Q(isnan(Q))=0;
    profilo15_18(j).interpolated(:,2)=Q;
end

% Interpolation
for j=4:3:241
    x=profilo15_20(j).real(:,1);
    y=profilo15_20(j).real(:,2);
    xint=(0:1:2500)';
    yint=interp1(x,y,xint);
    profilo15_20(j).interpolated(:,1)=xint;
    profilo15_20(j).interpolated(:,2)=yint;
    Q=profilo15_20(j).interpolated(:,2);
    Q(isnan(Q))=0;
    profilo15_20(j).interpolated(:,2)=Q;
end

% Interpolation
for j=4:3:241
    x=profilo15_21(j).real(:,1);
    y=profilo15_21(j).real(:,2);
    xint=(0:1:2500)';
    yint=interp1(x,y,xint);
    profilo15_21(j).interpolated(:,1)=xint;
    profilo15_21(j).interpolated(:,2)=yint;
    Q=profilo15_21(j).interpolated(:,2);
    Q(isnan(Q))=0;
    profilo15_21(j).interpolated(:,2)=Q;
end

% Interpolation
for j=4:3:241
    x=profilo15_22(j).real(:,1);
    y=profilo15_22(j).real(:,2);
    xint=(0:1:2500)';
    yint=interp1(x,y,xint);
    profilo15_22(j).interpolated(:,1)=xint;
    profilo15_22(j).interpolated(:,2)=yint;
    Q=profilo15_22(j).interpolated(:,2);
    Q(isnan(Q))=0;
    profilo15_22(j).interpolated(:,2)=Q;
end

% Interpolation
for j=4:3:241
    x=profilo15_23(j).real(:,1);
    y=profilo15_23(j).real(:,2);
```

```
    xint=(0:1:2500)';
    yint=interp1(x,y,xint);
    profilo15_23(j).interpolated(:,1)=xint;
    profilo15_23(j).interpolated(:,2)=yint;
    Q=profilo15_23(j).interpolated(:,2);
    Q(isnan(Q))=0;
    profilo15_23(j).interpolated(:,2)=Q;
end

% Interpolation
for j=4:3:241
    x=profilo15_24(j).real(:,1);
    y=profilo15_24(j).real(:,2);
    xint=(0:1:2500)';
    yint=interp1(x,y,xint);
    profilo15_24(j).interpolated(:,1)=xint;
    profilo15_24(j).interpolated(:,2)=yint;
    Q=profilo15_24(j).interpolated(:,2);
    Q(isnan(Q))=0;
    profilo15_24(j).interpolated(:,2)=Q;
end

%% Step 3: The water level surface profiles are averaged.

for j=4:3:241
   for p=0:1:2500
   x=p;
   y=(profilo15_12(j).interpolated(p+1,2)+
   profilo15_13(j).interpolated(p+1,2)+
         profilo15_14(j).interpolated(p+1,2)+
   profilo15_15(j).interpolated(p+1,2)+
         profilo15_18(j).interpolated(p+1,2)+
   profilo15_20(j).interpolated(p+1,2)+
         profilo15_21(j).interpolated(p+1,2)+
   profilo15_22(j).interpolated(p+1,2)+
         profilo15_23(j).interpolated(p+1,2)+
   profilo15_24(j).interpolated(p+1,2))/10;
   profilo15_25(j).mean(p+1,1)=x;
   profilo15_25(j).mean(p+1,2)=y;
   end
end

 %% Step 4: All points beneath 35mm are eliminated.

for j=4:3:241
     ind=0;
     s=size(profilo15_25(j).mean);
     for k=1:2500
          if profilo15_25(j).mean(k,2)>40
               ind=ind+1;
```

```
            profilo15_25(j).def(ind,1)=profilo15_25(j).mean(k,1);
            profilo15_25(j).def(ind,2)=profilo15_25(j).mean(k,2);
        else
        end
    end
end

%% Step 5: Results storing.
save profilo15_25 profilo15_25
```

A.6 Script to solve the SVE numerically

```
clc, clear all, close all

%% Step 1: Starting data.

%Specify model constants.
g=9.81; % gravitational constant
nu=0.91e-6;

%Channel properties.
B=0.5;          % Channel width (m)
Lx=3.5;         % Channel length (m)
So=0.0001;      % Bed slope
Hw=0.001;       % Initial water depth (m)
m=1207;         % Rods per m2
D=0.006;        % Rod Diameter (m)
hc=0.10;        % Rod height (m)
phi_veg=(m*pi*D*D)/4;
S=0.035;        %cylinder spacing (m)
lambda=(pi*D^(2)/4)/(0.5*S^2);

% Manning's Roughness coefficient
no1=0.055;

%% Step 2: Averaged water surface profile loading.

load('profilo15_25.mat');

%% Step 3: Determination of the inflow hydrograph

% Representation of the water surface for x=1mm.

for f=4:3:241
        ind=0;
        s=size(profilo15_25(f).interpolated);
  for k=1:s(1)
   if profilo15_25(f).interpolated(k,1)==1
    ind=ind+1;
    profilo15_25(f).uno(ind,1)=profilo15_25(f).interpolated(k,1);
```

```
    profilo15_25(f).uno(ind,2)=profilo15_25(f).interpolated(k,2);
   else
   end
  end
end

cc=0;
h1=[];

for j=4:3:241
    cc=cc+1;
    h1(cc)=profilo15_25(j).uno(:,2)./1000;
end
 hiniz=0.15;
 cc=0;
for j=4:3:241
    cc=cc+1;
    u(cc)=2*(sqrt(g*hiniz)-sqrt(g*h1(cc)));
    % the velocity is calculated with the Ritter Solution.
end

% time
t=0.09:0.09:7.20;

% Determination of the inflow hyodrgraph by using the velocity
% exerted  by the Ritter solution.
    for k=1:80
     Qm(k)=u(k).*B.*h1(k);
    end

figure(1)
plot(t,Qm,'.')

% Double logarithmic representation of the hydrograph. It can
% be seen a linear pattern.

figure(2)
loglog(t,h1,'.')


% Definition of the moment when the Ritter solution fails.
% From that moment is calculated the volume which has left
% the reservoir. This volume will be determine the power
% low relation between Q and t.

for j=4:3:241
    x=profilo15_25(j).def(:,1);
    y=profilo15_25(j).def(:,2);
    xint=(0:1:2500)';
    yint=interp1(x,y,xint);
```

```
    profilo15_25(j).prova(:,1)=xint;
    profilo15_25(j).prova(:,2)=yint;

end

   hmeani=(profilo15_25(151).prova(:,2));
   out = hmeani(all(~isnan(hmeani),2),:);
   hmeani=mean(out)/1000;
   volum=hmeani*B*2.5;

% Calculation of the real inflow hydrograph. The inflow
% volume Vin  is determined by calculating for each frame,
% starting  from t = 0s, the area under the water profile
% and then  multiplying for the width of the channel
% (B = 0.5m).
volume=[]

  for j=7:3:241
   hmean(:,1)=(profilo15_25(j).prova(:,1));
   hmean(:,2)=(profilo15_25(j).prova(:,2));
   out = hmean(all(~isnan(hmean),2),:);
   x=out(:,1);
   n=x(end)/1000;
   hmean1=mean(out)/1000;
   volume(j)=hmean1(2)*B*n;
  end


  cc=0
  for j=7:3:241
      cc=cc+1

      portata(cc)=(1.1*volume(j)-1.1*volume(j-3))/0.09;
  end
  cc=0
  for k=1:70
      cc=cc+1
      portata(cc)=(portata(k+1)+portata(k))/2;
  end

% In this part is inserted the exponential function
% which mimics the recession part.

media=mean(Qm(1:60));
Viniz=media*t(60);

cc=0;
cd=60;
for gg=61:1:80
    cc=cc+1;
```

```
    cd=cd+1;
    Qpower(cc)=0.1099*t(cd)^-1.11;
end

hold on
plot(t(61:80),Qpower,'.')

% In this part the hydrograph calculated before is modified
% by adding the real hydrograph at the beginning and
% the exponential tail at the end.

for k=1:1:44
    Qdef(k)=portata(k);
end
for k=45:1:60
    Qdef(k)=Qm(k);
end
media=mean(Qdef(1:56));
Viniz=media*t(56);
cv=0
  for k=61:1:80
      cv=cv+1
      Qdef(k)=Qpower(cv);
  end

% The hydrograph is plotted.

figure(3)
plot(t,Qdef,'b.')
s=size(Qdef);

% Q and h are interpolated with the same pace which will
% be used wor the numerically solution of the SVE.
tt=(0.09:0.09:7.20)';
yy=Qdef;
xx=tt;
xxint=(0.09:0.00001422:7.20);
yyint=interp1(xx,yy,xxint);
h1int=interp1(xx,h1,xxint);
Qdd(:,1)=xxint;
Qdd(:,2)=yyint;
h1dd(:,1)=xxint;
h1dd(:,2)=h1int;

figure
plot(Qdd(:,1),Qdd(:,2),'.')
figure
plot(h1dd(:,1),h1dd(:,2),'.')

 for u=1:size(Qdd)
```

```
        Qg(u,1)=Qdd(u,2);
        h1interp(u,1)=h1dd(u,2);

    end

Qd=Qg';
hinitial_c=h1interp';

%% Step 4: Numerical solution of the SVE

% Grid setup
tmin=0.09; tmax=7.20; Nt=5000000; dt=(tmax-tmin)/Nt;
NT_print=floor(Nt/1000);
xmin=0; xmax=Lx; Mx=100; dx=(xmax-xmin)/Mx;

x=[xmin:dx:xmax];
t=[tmin:dt:tmax];

M=length(x);
N=length(t);

%Initial conditions - Assume Uniform flow before wave entrance
Sf=So;

yic=Hw*ones(1,M);
Aic=B*yic;
R=Aic./(2*yic+B);
Vi=(1/no1)*R.^(2/3)*(Sf^(1/2));
Qic=Vi.*Aic;

ccp=1;
Qipc(ccp,:)=Qic;
yipc(ccp,:)=yic;

for i=1:N
     yic=[];Pwc=[];Vic=[];Sfc=[];alphac=[];betac=[];
     yic=Aic/B;
     Pwc=B+2*yic;
     Rc=Aic./Pwc;
     Vic=Qic./(Aic+eps);
     Uc = (Vic)/(1-sqrt(2*lambda/pi));
     Fr=Vic./(sqrt(g.*yic));

   % Reynolds numbers.

     Re=Vic*D/nu;
     Rec=Uc*D/nu;
     Rv=(pi/4)*((1-phi_veg)/phi_veg)*D;
     Rev=Vic*Rv/nu;
```

```
% Drag Coefficients.

 Cd_iso=11*Re.^(-3/4)+0.9*(1-exp(-1000./Re))+
 1.2*(1-exp(-(Re./4500).^0.7));
 Cd_array=50*Rev.^(-0.43)+0.7*(1-exp(-Rev/15000));
 Cd_manning=(2*g*(1-phi_veg)*no1^2)./(Rc.^(4/3)*m*D);
 Cd_staggered=1+10*Rec.^(-2/3);
 Cd_staggered_revised=0.4+10*Rec.^(-2/3);
 Cd_Froude=0.1+0.25*Fr.^(-0.5);
 Cd=Cd_staggered;

 %Adjust for submergence depth;
 Cd=Cd.*min(yic,hc)./(yic+10*eps);
 Sfc=(Cd*m*D/(1-phi_veg)).*(Vic.^2)/(2*g);

 % compute the friction slope
 % Sfc=((no1.*Vic)./((Rc+eps).^(2/3))).^2;

 alphac=2*Vic+((g*Aic/B-Vic.^2)./
 ((Vic+2*eps).*(5/3-4*Rc./3/B)));
 betac=g*Aic.*(Sfc-So);
 % Make sure inflow hydrograph sets the flow rate at x=0
 Qfc(1)=Qd(i);
 % March in time using the SVE
 Qfc(2:M)=Qic(2:M)-dt/dx*alphac(2:M).*(Qic(2:M)-Qic(1:M-1))
 -betac(2:M)*dt;
 cc1=[];
 cc1=find(Qfc<0);
 Qfc(cc1)=eps;
 Qic=Qfc;

 % Apply Continuity equation to determine depth
 Afc=[];
 Afc(2:M)=Aic(2:M)-(dt/dx)*(Qic(2:M)-Qic(1:M-1));
 Afc(1)=(B*hinitial_c(i));
 cc1=find(Afc<0);
 Afc(cc1)=eps;
 Aic=Afc;


 % Only store every NT_print for graphing
  if (mod(i,NT_print)<eps)
      ccp=ccp+1
      Qipc(ccp,:)=Qic;
      yipc(ccp,:)=yic;
      tp(ccp)=t(i);
  end

end
```

```
% Step 5: Representation of the measured water profile with the same time
% pace of SVE numerical solution.
clear k

tempo(3)=struct('real',[]);
for index=0:1:2500
for f=4:3:241

    s=size(profilo15_25(f).interpolated);
    for k=1:s(1)
         if profilo15_25(f).interpolated(k,1)==index
         ind=ind+1;
         tempo(f).real(ind,1)=profilo15_25(f).interpolated(k,1);
         tempo(f).real(ind,2)=profilo15_25(f).interpolated(k,2);
        else
        end
        end
end
end
% Remove the 0.
for h=4:241
    s=size(tempo(h).real);
    ind=0
    for k=1:s(1)
        if tempo(h).real(k,2)~=0
      ind=ind+1;
     tempo(h).def(ind,1)=tempo(h).real(k,1);
     tempo(h).def(ind,2)=tempo(h).real(k,2);
        else
        end
    end
end

h=[];

for k=1:1:2501
  ind=0;
for j=4:3:241
  ind=ind +1;
    h(ind)=tempo(j).def(k,2);
end
tempo(k).top=h;
end

yyyy=[]
for b=1:2501
for k=1:1:80

    yyyy(k)=tempo(b).top(1,k);
end
```

```
    xxint=(0.09:0.0071029:7.20);
    yyint=interp1(xx,yyyy,xxint);

    tempo(b).net(:,1)=xxint;
    tempo(b).net(:,2)=yyint;


end
ypsilon=[]
ind=0

for j=1:1:2501
    ind=ind+1
    ypsilon(:,j)=tempo(j).net(:,2)/1000;
end

%ics and ypsilon are the matrix containing the measured water profiles.
save ics ics
save ypsilon ypsilon

%THIS IS MAINLY FOR VISUALIZATION
Visualize_Results_withMovie
```

A.7 Script to represent the measured profile and the profile obtained by solving the SVE numerically

```
%% Step 1: load the water profiles.

load ics
load ypsilon
load x
laod yipc

% This file simply views the solution
outputFileName = ('streamFlow.avi');
vw = VideoWriter(outputFileName);
open(vw);

for ii=1:ccp

clf

subplot (3,1,1)
plot (tp,Qipc(:,1),'r-')
hold on
plot (tp(ii),Qipc(ii,1),'r.','markersize',5)
hold off
xlabel ('\it{t (s)}','fontweight','bold','fontsize',12)
ylabel ('\it{Q_{INFLOW} (m^3/s)}','fontweight','bold','fontsize',12)
subplot (3,1,2)
```

```
plot (x,yipc(ii,:))
hold on
plot(ics,ypsilon(ii,:),'r');
xlabel ('\it{x (m)}','fontweight','bold','fontsize',12)
ylabel('\it{h (m)}','fontweight','bold','fontsize',12)
axis ([0 3.6 0 0.4])

subplot (3,1,3)
plot(ics,ypsilon(ii,:),'r');


xlabel ('\it{x (m)}','fontweight','bold','fontsize',12)
ylabel('\it{h (m)}','fontweight','bold','fontsize',12)

axis ([0 3.6 0 0.4])

f=getframe(gcf);
writeVideo(vw,f.cdata)
end
close(vw);
```

Bibliography

[1] Ayodele E. Ajayi, Nick van de Giesen, and Paul Vlek. A numerical model for simulating hortonian overland flow on tropical hillslopes with vegetation elements. *Hydrological Processes*, 22(8):1107–1118, 2008.

[2] Doug Alsdorf, Charon Birkett, Thomas Dunne, John Melack, and Laura Hess. Water level changes in a large amazon lake measured with spaceborne radar interferometry and altimetry. *Geophysical Research Letters*, 28(14):2671–2674, 2001.

[3] Douglas E Alsdorf, John M Melack, Thomas Dunne, Leal AK Mertes, Laura L Hess, and Laurence C Smith. Interferometric radar measurements of water level changes on the amazon flood plain. *Nature*, 404(6774):174, 2000.

[4] Douglas E Alsdorf, Ernesto Rodríguez, and Dennis P Lettenmaier. Measuring surface water from space. *Reviews of Geophysics*, 45(2), 2007.

[5] Christophe Ancey, RM Iverson, Martin Rentschler, and RP Denlinger. An exact solution for ideal dam-break floods on steep slopes. *Water Resources Research*, 44(1), 2008.

[6] S Assouline, SE Thompson, L Chen, T Svoray, S Sela, and GG Katul. The dual role of soil crusts in desertification. *Journal of Geophysical Research: Biogeosciences*, 120(10):2108–2119, 2015.

[7] MJ Baptist, Vladan Babovic, J Rodríguez Uthurburu, M Keijzer, RE Uittenbogaard, A Mynett, and A Verwey. On inducing equations for vegetation resistance. *Journal of Hydraulic Research*, 45(4):435–450, 2007.

[8] Constantine V Bellos and John G Sakkas. 1-d dam-break flood-wave propagation on dry bed. *Journal of Hydraulic Engineering*, 113(12):1510–1524, 1987.

[9] Federal Investigative Board. Report of failure of kelly barnes dam, toccoa, georgia. *Report to the Office of the Governor of Georgia, Atlanta, Georgia*, 1977.

[10] Sara Bonetti, Gabriele Manoli, Costantino Manes, Amilcare Porporato, and Gabriel G Katul. Manning's formula and strickler's scaling explained by a co-spectral budget model. *Journal of Fluid Mechanics*, 812:1189–1212, 2017.

[11] Hervé Capart. Analytical solutions for gradual dam breaching and downstream river flooding. *Water Resources Research*, 49(4):1968–1987, 2013.

[12] FRANCESCO GIUSEPPE Carollo, VITO Ferro, and D Termini. Flow velocity measurements in vegetated channels. *Journal of Hydraulic Engineering*, 128(7):664–673, 2002.

[13] Jonathan L Carrivick. Dam break–outburst flood propagation and transient hydraulics: a geosciences perspective. *Journal of Hydrology*, 380(3-4):338–355, 2010.

[14] Hubert Chanson. Application of the method of characteristics to the dam break wave problem. *Journal of Hydraulic Research*, 47(1):41–49, 2009.

[15] John A. Chapman, Bruce N. Wilson, and John S. Gulliver. Drag force parameters of rigid and flexible vegetal elements. *Water Resources Research*, 51(5):3292–3302, 2015.

[16] Nian-Sheng Cheng. Calculation of drag coefficient for arrays of emergent circular cylinders with pseudofluid model. *Journal of Hydraulic Engineering*, 139(6):602–611, 2012.

[17] Nian-Sheng Cheng. Single-layer model for average flow velocity with submerged rigid cylinders. *Journal of Hydraulic Engineering*, 141(10):06015012, 2015.

[18] Nian-Sheng Cheng and Hoai Thanh Nguyen. Hydraulic radius for evaluating resistance induced by simulated emergent vegetation in open-channel flows. *Journal of Hydraulic Engineering*, 137(9):995–1004, 2010.

[19] Nian-Sheng Cheng. Representative roughness height of submerged vegetation. *Water Resources Research*, 47(8), 2011.

[20] Edoardo Daly and Amilcare Porporato. Similarity solutions of nonlinear diffusion problems related to mathematical hydraulics and the fokker-planck equation. *Physical Review E*, 70(5):056303, 2004.

[21] AJC Barré de Saint-Venant. Theorie du mouvement non permanent des eaux, avec application aux crues des rivieres et a l'introduction des mare es dans leurs lits. *Comptes Rendus des seances de l'Academie des Sciences*, 73:237–240, 1871.

[22] JT Dijkstra and RE Uittenbogaard. Modeling the interaction between flow and highly flexible aquatic vegetation. *Water Resources Research*, 46(12), 2010.

[23] Robert F Dressler. *Hydraulic resistance effect upon the dam-break functions*, volume 49. National Bureau of Standards, Washington, DC, 1952.

[24] Vahid Etminan, Ryan J. Lowe, and Marco Ghisalberti. A new model for predicting the drag exerted by vegetation canopies. *Water Resources Research*, 53(4):3179–3196, 2017.

[25] G Fasanella. *Studio sperimentale dell'influenza di macroscabrezze sulla propagazione di onde di piena*. Tesi di laurea magistrale, Politecnico di Torino, Dicembre 2017.

[26] Julian C Green. Modelling flow resistance in vegetated streams: review and development of new theory. *Hydrological Processes*, 19(6):1245–1259, 2005.

[27] Andrew J Hogg and David Pritchard. The effects of hydraulic resistance on dam-break and other shallow inertial flows. *Journal of Fluid Mechanics*, 501:179–212, 2004.

[28] Joseph Holden, Mike J Kirkby, Stuart N Lane, David G Milledge, Chris J Brookes, Vincent Holden, and Adrian T McDonald. Overland flow velocity and roughness properties in peatlands. *Water Resources Research*, 44(6), 2008.

[29] W.-X. Huai, Y.-H. Zeng, Z.-G. Xu, and Z.-H. Yang. Three-layer model for vertical velocity distribution in open channel flow with submerged rigid vegetation. *Advances in Water Resources*, 32(4):487–492, 2009.

[30] Bruce Hunt. Asymptotic solution for dam-break problem. *Journal of the Hydraulics Division*, 108(1):115–126, 1982.

[31] Bruce Hunt. Dam-break solution. *Journal of Hydraulic Engineering*, 110(6):675–686, 1984.

[32] Bruce Hunt. Perturbation solution for dam-break floods. *Journal of Hydraulic Engineering*, 110(8):1058–1071, 1984.

[33] Fredrik Huthoff, Denie Augustijn, and Suzanne JMH Hulscher. Analytical solution of the depth-averaged flow velocity in case of submerged rigid cylindrical vegetation. *Water Resources Research*, 43(6), 2007.

[34] Yoshiharu Ishikawa, Kunio Mizuhara, and Shinnya Ashida. Effect of density of trees on drag exerted on trees in river channels. *Journal of Forest Research*, 5(4):271–279, 2000.

[35] CS James, AL Birkhead, AA Jordanova, and JJ O'sullivan. Flow resistance of emergent vegetation. *Journal of Hydraulic Research*, 42(4):390–398, 2004.

[36] Imre M Jánosi, Dominique Jan, K Gábor Szabó, and Tamás Tél. Turbulent drag reduction in dam-break flows. *Experiments in Fluids*, 37(2):219–229, 2004.

[37] Juha Järvelä. Flow resistance of flexible and stiff vegetation: a flume study with natural plants. *Journal of Hydrology*, 269(1):44–54, 2002.

[38] Robert H Kadlec. Overview: surface flow constructed wetlands. *Water Science and Technology*, 32(3):1–12, 1995.

[39] Gabriel G Katul, Davide Poggi, and Luca Ridolfi. A flow resistance model for assessing the impact of vegetation on flood routing mechanics. *Water Resources Research*, 47(8), 2011.

[40] Gabriel G. Katul, Patricia Wiberg, John Albertson, and George Hornberger. A mixing layer theory for flow resistance in shallow streams. *Water Resources Research*, 38(11), 2002.

[41] Sonia Kefi, Max Rietkerk, and Gabriel G Katul. Vegetation pattern shift as a result of rising atmospheric co_2 in arid ecosystems. *Theoretical Population Biology*, 74(4):332–344, 2008.

[42] M Erol Keskin and Necati Ağiralioğlu. A simplified dynamic model for flood routing in rectangular channels. *Journal of Hydrology*, 202(1-4):302–314, 1997.

[43] Jongho Kim, Valeriy Y Ivanov, and Nikolaos D Katopodes. Hydraulic resistance to overland flow on surfaces with partially submerged vegetation. *Water Resources Research*, 48(10), 2012.

[44] Nobuhisa Kobayashi, Andrew W Raichle, and Toshiyuki Asano. Wave attenuation by vegetation. *Journal of waterway, port, coastal, and ocean engineering*, 119(1):30–48, 1993.

[45] Alexandra G Konings, Gabriel G Katul, and Sally E Thompson. A phenomenological model for the flow resistance over submerged vegetation. *Water Resources Research*, 48(2), 2012.

[46] Umesh C Kothyari, Kenjirou Hayashi, and Haruyuki Hashimoto. Drag coefficient of unsubmerged rigid vegetation stems in open channel flows. *Journal of Hydraulic Research*, 47(6):691–699, 2009.

[47] Nicholas Kouwen, TE Unny, and Harry M Hill. Flow retardance in vegetated channels. *Journal of the Irrigation and Drainage Division*, 95(2):329–344, 1969.

[48] Vladimir V Kulish and José L Lage. Application of fractional calculus to fluid mechanics. *Journal of Fluids Engineering*, 124(3):803–806, 2002.

[49] Lindsey Ann LaRocque, Jasim Imran, and M Hanif Chaudhry. Experimental and numerical investigations of two-dimensional dam-break flows. *Journal of Hydraulic Engineering*, 139(6):569–579, 2012.

[50] DSL Lawrence. Hydraulic resistance in overland flow during partial and marginal surface inundation: Experimental observations and modeling. *Water Resources Research*, 36(8):2381–2393, 2000.

[51] J.K. Lee, L.C. Roig, H.L. Jenter, and H.M. Visser. Drag coefficients for modeling flow through emergent vegetation in the florida everglades. *Ecological Engineering*, 22(4–5):237–248, 2004.

[52] Hongbo Ma and Xudong Fu. Real time prediction approach for floods caused by failure of natural dams due to overtopping. *Advances in water resources*, 35:10–19, 2012.

[53] R. Manning. On the flow of water in open channels and pipes. *Trans. Inst. Civil Eng. Ireland*, 20(5-6):161–207, 1891.

[54] Timothy I Marjoribanks, Richard J Hardy, and Stuart N Lane. The hydraulic description of vegetated river channels: the weaknesses of existing formulations and emerging alternatives. *Wiley Interdisciplinary Reviews: Water*, 1(6):549–560, 2014.

[55] Mark Morris, H Hewlett, and C Elliot. Risk and reservoirs in the uk. *Construction Industry Research and Information Association (CIRIA) Water Group*, 2000.

[56] Heidi M Nepf. Flow and transport in regions with aquatic vegetation. *Annual Review of Fluid Mechanics*, 44:123–142, 2012.

[57] HM Nepf. Drag, turbulence, and diffusion in flow through emergent vegetation. *Water Resources Research*, 35(2):479–489, 1999.

[58] L Noarayanan, K Murali, and V Sundar. Manning's 'n'co-efficient for flexible emergent vegetation in tandem configuration. *Journal of hydro-environment research*, 6(1):51–62, 2012.

[59] Athanasios Paschalis, Gabriel G Katul, Simone Fatichi, Gabriele Manoli, and Peter Molnar. Matching ecohydrological processes and scales of banded vegetation patterns in semi-arid catchments. *Water Resources Research*, pages 1–68, 2016.

[60] John D Pisaniello. A comparative review of environmental protection policies and laws involving hazardous private dams: Appropriate practice models for safe catchments. *Wm. & Mary Envtl. L. & Pol'y Rev.*, 35:515, 2010.

[61] D Poggi, A Porporato, L Ridolfi, JD Albertson, and GG Katul. The effect of vegetation density on canopy sub-layer turbulence. *Boundary-Layer Meteorology*, 111(3):565–587, 2004.

[62] Davide Poggi, Claudia Krug, and Gabriel G Katul. Hydraulic resistance of submerged rigid vegetation derived from first-order closure models. *Water Resources Research*, 45(10), 2009.

[63] MR Raupach. Drag and drag partition on rough surfaces. *Boundary-Layer Meteorology*, 60(4):375–395, 1992.

[64] Ian Reid, Jonathan B Laronne, and D Mark Powell. Flash-flood and bedload dynamics of desert gravel-bed streams. *Hydrological Processes*, 12(4):543–557, 1998.

[65] August Ritter. Die fortpflanzung der wasserwellen. *Zeitschrift des Vereines Deutscher Ingenieure*, 36(33):947–954, 1892.

[66] A Schoklitsch. Ueber dambruchwellen, sitzber. *Akad. Wise. Wien*, 126, 1917.

[67] Sandra Soares-Frazão and Yves Zech. Dam-break flow through an idealised city. *Journal of Hydraulic Research*, 46(5):648–658, 2008.

[68] PK Stansby, A Chegini, and TCD Barnes. The initial stages of dam-break flow. *Journal of Fluid Mechanics*, 374:407–424, 1998.

[69] T Stoesser, SJ Kim, and P Diplas. Turbulent flow through idealized emergent vegetation. *Journal of Hydraulic Engineering*, 136(12):1003–1017, 2010.

[70] Yukie Tanino and Heidi M Nepf. Laboratory investigation of mean drag in a random array of rigid, emergent cylinders. *Journal of Hydraulic Engineering*, 134(1):34–41, 2008.

[71] Sally Thompson, Gabriel Katul, Alexandra Konings, and Luca Ridolfi. Unsteady overland flow on flat surfaces induced by spatial permeability contrasts. *Advances in Water Resources*, 34(8):1049–1058, 2011.

[72] Bo Wang, Yunliang Chen, Chao Wu, Jianhua Dong, Xiao Ma, and Jiajun Song. A semi-analytical approach for predicting peak discharge of floods caused by embankment dam failures. *Hydrological Processes*, 30(20):3682–3691, 2016.

[73] Li-hui Wang and Cun-hong Pan. An analysis of dam-break flow on slope. *Journal of Hydrodynamics, Ser. B*, 26(6):902–911, 2015.

[74] Wei-Jie Wang, Wen-Xin Huai, Sally Thompson, and Gabriel G Katul. Steady nonuniform shallow flow within emergent vegetation. *Water Resources Research*, 51(12):10047–10064, 2015.

[75] Wei-Jie Wang, Wen-Xin Huai, Sally Thompson, Wen-Qi Peng, and Gabriel G Katul. Drag coefficient estimation using flume experiments in shallow non-uniform water flow within emergent vegetation during rainfall. *Ecological Indicators*, 2017.

[76] Gerald Beresford Whitham. The effects of hydraulic resistance in the dam-break problem. *Proc. R. Soc. Lond. A*, 227(1170):399–407, 1955.

[77] F.C. Wu, H.W. Shen, and Y.J. Chou. Variation of roughness coefficients for unsubmerged and submerged vegetation. *Journal of hydraulic Engineering*, 125(9):934–942, 1999.

[78] Momchilo M. Zdravkovich. Flow around circular cylinders, applications. 2, 2000.

[79] LM Zhang, Y Xu, and JS Jia. Analysis of earth dam failures: A database approach. *Georisk*, 3(3):184–189, 2009.

[80] K. Zhao, N.S. Cheng, X. Wang, and S.K. Tan. Measurements of fluctuation in drag acting on rigid cylinder array in open channel flow. *Journal of Hydraulic Engineering*, 140(1):48–55, 2013.

Acknowledgements

A conclusione di questo percorso è doveroso ringraziare tutte le persone che mi hanno accompagnato durante questi tre anni a Torino.
Vorrei ringraziare prima di tutto il prof. Poggi, relatore di questa tesi, per avermi dato la possibilità di sviluppare questo lavoro e realizzare il mio desiderio di andare negli Stati Uniti. Un grazie speciale va anche a Gaby per avermi fatto sentire a casa anche a Durham e per avermi guidato lungo i tre mesi trascorsi in North Carolina. Desidero inoltre ringraziare Silvia e Gianni per l'aiuto morale e sopratutto il supporto tecnico offerto durante questi lunghi otto mesi così come tutti i ragazzi del laboratorio per aver reso più leggere le lunghe giornate.
Un immenso ringraziamento a mio padre Alessandro e a mia madre Serenella per avermi dato la possibilità di studiare al Politecnico e per avermi sempre sostenuto senza mai pretendere niente, senza di voi non sarei diventato la persona che sono ora. Un grazie speciale a mio fratello Mirco per aver sempre riposto fiducia in me e per avermi spronato a fare di più. Spero di avervi reso fieri!
Un rigraziamento speciale alla mia fidanzata Eleonora, per aver supportato il mio trasferimento a Torino senza mai esitare e senza mai perdere la fiducia in me. Durante questo periodo il tuo amore mi ha aiutato a realizzarmi come studente e come uomo, questo traguardo è per metà anche tuo!
Grazie infine a tutti i miei amici(vicini e lontani) per avermi accompagnato durante questo percorso e aver reso questi tre anni a Torino una avventura indimenticabile.